Electron-Beam Lithography of Quantum Interference Devices For Electron Transport Studies

A Dissertation

Presented to the Faculty of the Graduate School

of

Yale University

in Candidacy for the Degree of

Doctor of Philosophy

by

Michael Joseph Rooks

December 1987

ABSTRACT

Electron-Beam Lithography of Quantum Interference Devices For Electron Transport Studies

Michael Joseph Rooks

Yale University

1987

Electron-beam lithography is employed to fabricate devices for electron-transport studies. A modified scanning-electron microscope is used to produce sub-0.1 μm features, and a hybrid deep-ultraviolet/electron-beam process is used to fabricate complete devices. Feature sizes as small as 30 nm have been produced with a process which uses a novel PMMA/PMMA bilayer electron-beam resist. This process allows the fabrication of metal structures whose sizes are on the order of the electron phase-breaking length, ℓ_ϕ. Devices with dimensions smaller than ℓ_ϕ demonstrate corrections to the Drude conductivity which are determined by quantum interference effects characteristic of lower-dimensional systems. These effects are observed in micron-size normal-metal rings of Al and Ag. Resistance oscillations with a flux period of h/2e, as predicted by Altshuler et al., as well as those with period h/e, are observed in 1-2 μm diameter rings. These electron interference effects in metal rings are the solid-state analog of the Aharonov-Bohm effect for electrons in vacuum. Narrow wires of Al and Ag, of width 35 to 110 nm, are used to probe the electron phase breaking rate. This rate is an important parameter for theories which predict the magnitude of interference effects seen in rings. We find that this rate at low temperatures is dominated by one-dimensional electron-electron scattering with small energy transfers.

Acknowledgements

It is my honor to acknowledge the assistance and encouragement of many people. Prof. Daniel Prober has been an ideal advisor, and has supported my efforts through thick and thin. Dan has provided a vast quantity of scientific insights, encouragement, vitality, humor, and analogy jokes (not to mention funding) to myself and to his lab.

The experience of senior graduate students has been passed down to me over the years. P. Santhanam had the patience to explain localization to me, and he has contributed a steady current of encouragement and unmuddied thinking. I have also found his thesis to be of great utility. The art of junction fabrication and characterization was taught to me by Dean Face. Dean has also shown me many drafting tricks, and has been a great help in developing our word-processing facility. Few ventures in our lab have been untouched by Dean's meticulous style. Shalom Wind has helped me with many processing difficulties, and has taught me how to work with PMMA. Shalom has done the bulk of the work involved in the wire experiment described in this thesis, and has carried forward the DProberlab humor begun by Bruce Dalrymple. The cryostat used for almost all of our measurements was built by Bruce Dalrymple.

Most measurements of rings and wires were performed by Venkat Chandrasekhar and Shalom Wind. Chandrasekhar built the temperature-control circuit, the computer-controlled magnetoresistance circuit, and has labored long to improve the sensitivity of the four-terminal bridge. His expertise in measurement has been a

vital part of our efforts. After several abortive efforts by others, Paul McEuen provided the black magic for mixing PMMA in xylene. Paul has been an essential ingredient in the PMMA bilayer, and is a worthy heir to the e-beam system. DC measurement of junctions would not have been possible without the help of Elie Track. I would also like to thank Elie for pointing out that life is indeed a carrot. Thomas Kopley, A. Hodge Worsham, G. J. Cui, and Steven Ruggiero have been valued compatriots, and have added to the diversity and quality of DProberlablife.

Several very talented undergraduates have contributed to the development of the e-beam system. Steve Lowen rebuilt and redesigned many parts of the e-beam interface, and has taught me much about building "clean" electronics. Eng Lo added the "turbo drive" (variable-speed raster) and filter sections to the interface. Steve Sanders built a spare interface board, debugged the circuit diagrams, and computerized almost all of the figures appearing in Appendix B.

I am grateful for many helpful discussions with Prof. Robert Wheeler, who has contributed his wisdom, support, and enthusiasm to our group. Professors A. Douglas Stone and Yoseph Imry have often been on hand to provide physical insights into the theories, and were always willing to answer my naive experimentalist questions. Prof. Imry has also been kind enough to review this thesis as an "outside reader". Professors T. P. Ma and P. Kindlmann have shown an ongoing interest in my work, and have served on my thesis committee along with Professors Daniel Prober, Robert Wheeler, and A. Douglas Stone.

Like many other graduate students, I am indebted to Clifford Sneider for designing, building, and maintaining many of the gadgets in our lab. Philippe Mâle

and Hans Stukenbrok of the Yale Medical School, and Alan Pooley of the Peabody Museum have provided their time and expertise for SEM and TEM studies. June Yarosh has helped me to wade through seas of paperwork, and has been a master of patience and tolerance.

Outside of Yale, I have benefitted greatly from discussions with Joseph Sauvageau and James Lukens of SUNY Stony Brook, who taught us how to expose PMMA with deep-UV light. Richard Howard of ATT Bell Laboratories was also very helpful in our initial stages of lithography development. Stuart Mackie and Steve Beaumont of Glasgow University supplied many unpublished tricks which helped us implement the PMMA bilayer technique.

This research was supported by NSF grants ECS-8305000, ECS-8509135, and DMR-8505539. Facilities support was provided by NSF DMR-8213080, IBM Corp., Shipley Inc., Hewlett-Packard Co., the Yale Center for Microelectronic Materials and Structures, and Yale University.

Finally, I would like to dedicate this thesis to my wife Naomi.

Contents

List of Symbols and Abbreviations

AAK	Altshuler, Aronov, and Khmelnitskii (see references)
AAS	Altshuler, Aronov, and Spivak (see references)
$\vec{A}$	Magnetic vector potential
A	Cross-sectional area
D	Diffusion constant = $v_F \ell/3$
DAC	Digital to analog converter
DUV	Deep-ultraviolet
e	Electron charge
E	Energy
E_c	Correlation energy
g	Dimensionless conductance (units of e^2/h)
g_b	Background ohmic conductance
G	Conductance
GPIB	General purpose interface bus (IEEE-488, "HPIB")
$\hbar$	Planck's constant
H	Magnetic field
H_{c2}	Upper critical field for superconductivity
HPIB	Hewlett-Packard interface bus (IEEE-488)
I	Current
I_c	Critical current for superconductivity
IPA	Isopropanol (2-propanol)
k	wavevector
k_F	Fermi wavevector
k_B	Boltzmann's constant

ℓ	Elastic scattering length (diffusion length)
ℓ_ϕ	Phase-breaking length of electrons
ℓ_H	Magnetic length, = $\sqrt{3}\hbar/(eBW)$
ℓ_N	Nyquist scattering length
ℓ_{so}	Spin-orbit scattering length
ℓ_T	Thermal diffusion length of electrons
ℓ_1	Composite length scale, = $(D\tau_1)^{1/2}$, used in eq. III-3
ℓ_2	Composite length scale, = $(D\tau_2)^{1/2}$, used in eq. III-3
L	Device length; Displacement
m	Electron effective mass
MIBK	Methyl isobutyl ketone
MOSFET	Meltal-oxide-semiconductor field effect transistor
N	Number of atoms in a wire's cross-section; Number of rings
N(ω)	Number density of fluctuation photons
N-QUID	normal-state quantum interference device
PMMA	Polymethylmethacrylate
q_{ph}	Phonon wavevector
r	Distance, or spacial vector; radius of a ring
R	Resistance; Reflection coefficient
$R_\square$	Resistance per square
R_N	Normal-state resistance at low temperatures
RIE	Reactive ion etching
s	Path length
SEM	Scanning electron microscope/microscopy
STEM	Scanning transmission electron microscope
SQUID	Superconducting quantum-interference device

T	Temperature; Transmission coefficient
TEM	Transmission electron microscope/microscopy
t	Time; Transmission matrix
v_F	Fermi velocity
V	Barrier height
W	Line width
α	Wavefunction amplitude
β	Larkin parameter
γ_n	Single-ring oscillation phase factor for the n^{th} harmonic
Δ	Superconducting energy gap
κ	$\{(2m/\hbar^2)[V-E]\}^{1/2}$
μ	Chemical potential
ρ	Resistivity
ρ_o	Drude resistivity
σ	Conductivity
σ_o	Drude conductivity
τ^{-1}	Elastic scattering rate
τ_ϕ^{-1}	Phase-breaking, or "inelastic" rate
τ_{ee}^{-1}	Electron-electron scattering rate
τ_{ep}^{-1}	Electron-phonon scattering rate
τ_N^{-1}	Nyquist scattering rate
τ_1^{-1}	Scattering rate associated with ℓ_1 (see eq. III-3)
τ_2^{-1}	Scattering rate associated with ℓ_2 (see eq. III-3)
ϕ	phase of wavefunction
Φ	Magnetic flux
Φ_o	Single-electron flux quantum, h/e

Φ_h	Flux through the hole of a ring
ψ	Electron wavefunction

List of Figures

List of Tables

I. Introduction

Advances in microfabrication technology have allowed the linewidths found in commercial integrated circuits to be reduced to the 1 μm scale. Linewidths produced in the laboratory [Craighead, et al., 1983; Mackie and Beaumont, 1985; Broers, et al., 1976; Rooks, et al. 1987] are as much as 100 times smaller. The trend toward smaller and faster commercial integrated circuits requires an understanding of the scaling properties of small devices. Techniques of microfabrication have not only allowed the study of such commercially-important devices, but have also opened a regime of experimental science important in its own right: the physics of electron transport in ultrasmall structures.

I.A. Device Studies

A free electron in vacuum can be described by a wavefunction

$$\psi = |\psi| e^{i\phi} = |\psi| e^{i[\vec{k}\cdot\vec{r} - (Et/\hbar)]} \qquad \text{(I-1)}$$

where $\vec{k}$ is the wavevector and E is the energy. A real metal has defects, impurities, and grain boundaries. When the electron moves in such a metal at low temperatures, it undergoes many elastic scattering events, in which $\vec{k}$ changes while E does not. The length between elastic scattering events, the mean-free path ℓ, is typically 1-10 nm in most metal films. The electron moves diffusively - perhaps under the influence of a net electric field - taking steps of length $\ell = v_F\tau$, where v_F is the Fermi velocity and τ is the time between elastic scattering events. After a time τ_ϕ the electron's phase will change by an amount comparable to π,

relative to what the phase would be had the electron not undergone any energy-changing (inelastic) collisions. Since the number of inelastic collisions goes to zero as the temperature approaches zero, $\tau_\phi >> \tau$ at low temperatures. The corresponding length scale is $\ell_\phi = (D\tau_\phi)^{1/2}$, which is the phase-coherence length. $D = v_F\ell/3$ is the diffusion constant for conduction in films with $\ell < d$. Phase-breaking events can arise from electron-electron scattering or electron-phonon interaction.

There is an important distinction between elastic and inelastic scattering: collisions which change the energy state alter the phase in a time-dependent manner. In contrast, a set of elastic collisions can form a standing-wave pattern analogous to water waves in a rocky stream. An electron "remembers" its phase over a distance ℓ_ϕ; therefore, devices designed to show effects due to the interference of electron waves should be made smaller than the phase-coherence length of electrons in the material.

Wires which are much longer than ℓ_ϕ, but whose width W is much smaller than ℓ_ϕ, are considered "one-dimensional" (1D) in the theory of localization. First predicted by Thouless for wires of finite width at finite temperature [Thouless, 1977], electron localization causes an *increase* in the resistance of the wire as the temperature approaches 0 K. This rise in R is in contrast to the resistance of a classical wire at low temperature, which approaches a constant value determined by impurity scattering. In a non-classical, narrow wire at low temperatures the electrons have an enhanced probability - due to quantum interference - of forming standing waves; this is the origin of the term "localization". The effect has been studied thoroughly, both theoretically [e.g. Altshuler, et al.,1981; Fukuyama, 1984]

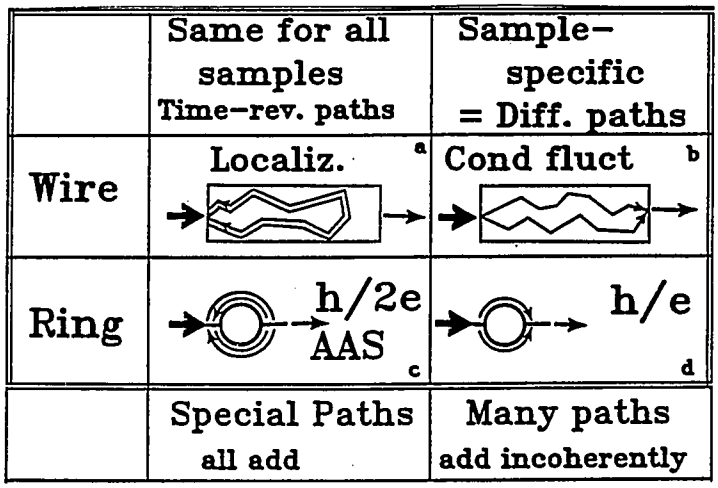

Fig. I-1: Summary of quantum transport effects. (a) interference due to time-reversed paths in wires leads to localization effects, (b) random paths in short samples leads to conductance fluctuation effects, (c) time-reversed paths in ring structures cause oscillations in the resistance with magnetic flux period h/2e, (d) random, sample-specific paths in rings cause oscillations in the resistance with magnetic flux period h/e. From [Prober, 1986].

and experimentally [Bergmann, 1984; Santhanam et al., 1984, 1987, and references therein].

Studies of localization have been important for understanding quantum interference effects in micron-size rings. Fig. I-1 gives a summary of these effects, in rings and wires. Single rings of Al and Ag have shown oscillations in their resistance as a function of magnetic field. These oscillations are due to the interference of electron waves - the same interference which causes localization effects in wires. Other interference effects seen in rings are seen as well in short wires (where $L < \ell_\phi$).

I.B. Lithography

In order to study quantum interference effects (as discussed in section I.B.) in an effectively lower-dimensional system, one or more of the dimensions of the device must be less than the phase-breaking length ℓ_ϕ. This length is typically one micron at low temperatures (~1 K). For a moderately complex device - e.g., a ring - the linewidth must be much smaller than ℓ_ϕ - say, W ~ 0.1 μm. To study the effects of one-dimensional electron-electron scattering, a wire must also be narrower than the thermal diffusion length $\ell_T = (\hbar D/k_B T)^{1/2}$, where D is the diffusion constant and T is the temperature. ℓ_T ~ 0.1 μm in typical metal wires at ~2K. These dimensional constraints (as discussed further in sections I.B. and III) require the use of a high-resolution technique such as electron-beam lithography.

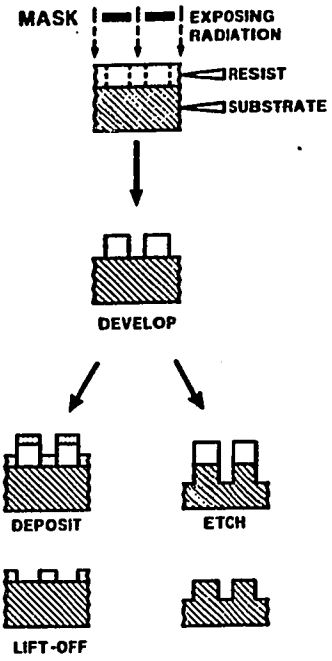

Fig. I-2: The basic steps of lithography. An organic resist on a Si wafer is exposed with light and developed. The pattern left in resist can be transfered by etching (right). Alternatively, a metal is evaporated onto the pattern followed by imersion in acetone. The acetone dissolves the organic resist, leaving a metal pattern. This "liftoff" process is shown on the left. From [Howard and Prober, 1982].

I.B.1. Exposure and Pattern Transfer

The basic steps of lithography are shown in Fig. I-2. Consider the following process example. A solution of polymethylmethacrylate (PMMA) in a solvent is spun on an oxidized silicon wafer, then baked to form a solid layer. The PMMA resist is then exposed, either with light or with electrons, thereby breaking bonds in the long chain resist polymer. A developer will preferentially dissolve the low molecular-weight areas of the polymer film, leaving the desired pattern. The pattern is then transferred to the substrate either by etching (wet etching or plasma etching) or by the "liftoff" technique. In the liftoff process a metal film is evaporated onto a developed pattern. The remaining resist is dissolved by immersion in acetone, leaving a pattern of metal as shown in Fig. I-2. Liftoff is the technique used for most of the work described here.

I.B.2. Electron-Beam System

The e-beam patterning used for this work employs a standard ISI SS-60 scanning electron microscope (SEM) [ISI]. A custom interface drives the electron beam in a raster pattern, while a computer turns the beam on and off. These "beam blanking" signals are fed from the computer, through the raster interface, to an electrostatic beam blanker on the SEM column (Fig. I-3). For features larger than 0.1 μm a single layer of PMMA (0.3 μm thick) is used as the resist. For linewidths down to 30 nm, a two-layer PMMA resist is used. The pattern is defined in the thin top layer. The bottom layer serves to enhance the resist undercut, and provides the overall thickness necessary for lifting-off a metal pattern. This bilayer is discussed thoroughly in section II.D.

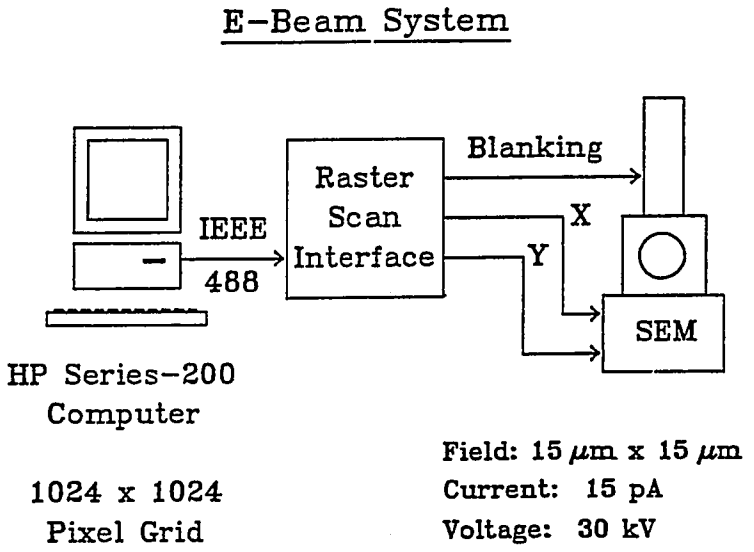

Fig. I-3: Electron-beam lithography system. A scanning electron microscope equipped with an electrostatic beam-blanker receives X-Y scan signals from a custom raster-scan interface, while blanking signals are sent through the interface from a Hewlett-Packard Series-200 computer. The computer also sends information which allows the interface to change raster speeds.

The most fundamental limitation of e-beam lithography is its serial nature (i.e., the primitive shapes in the pattern are drawn one after another). In contrast, the process of photolithography is a parallel process - in which the entire pattern is transferred from mask to wafer in one step, regardless of pattern complexity. A number of works have reviewed the process of standard photolithography: [e.g., Lin, 1983; Ghandhi, 1983]. Fortunately, PMMA can be used both as a photoresist and as an e-beam resist, so that the advantages of both mechanisms can be exploited.

I.C. Motivation and Outline

The next chapter (II) is devoted to the fabrication techniques which have constituted the largest portion of this thesis work. A more complete discussion of quantum interference effects will be presented in chapter III. Earlier studies of scattering mechanisms and quantum interference effects in metals (e.g., localization experiments) were greatly limited because devices (wires) could not be made smaller than the relevant dimensional length scales, or materials were not completely characterized. These considerations have motivated the development of a flexible high-resolution electron-beam lithography facility.

A new regime of device size scales has made possible a great variety of new experiments. Electron-beam lithography at Yale has been applied to (1) the Aharonov-Bohm effect in metal rings, (2) one-dimensional electron-electron scattering in wires, (3) spatial quantization in narrow-gate MOSFETs, and (4) normal-state junction interference devices. This thesis deals primarily with electron-beam lithography, ring experiments, experiments on normal-junctions, and (to a lesser

degree) experiments on 1D electron-electron scattering. The experiments will be discussed in chapter IV, following the theoretical discussion in chapter III.

II. Fabrication Techniques

II.A. Process Outline

The basic steps of the liftoff process have been described in section I.B.1, and are shown in Fig. II-1. Electron-beam (e-beam) lithography provides high-resolution exposure, but with our system is too slow for full-wafer exposure. A typical e-beam exposure takes 1 minute for a 15×15 μm field using a beam current of 15 pA. The same exposure over a 3 inch diameter wafer, using even 1000 pA, would take 210 days. Fortunately, PMMA can be exposed with deep-ultraviolet (DUV) light, using a contact mask. Features as small as ~1 μm can be exposed simultaneously over an entire wafer, using typically a 15-20 minute exposure.

The hybrid DUV/e-beam process is shown in Fig. II-2. PMMA is first exposed with DUV light (~220 nm), then developed in 1:3 methylisobutylketone : isopropanol (MIBK:IPA). The resist is then exposed with e-beam, and then developed for a second time. Large and small features are thus produced on the same die, by lifting-off a metal film. DUV exposure provides an efficient method of producing contact pads and large structures in the resist prior to e-beam exposure for fine-scale devices. In addition, the pattern left in the resist after DUV exposure and development can be used for alignment and focusing of the e-beam system.

Another way to solve the problem of fabricating large features is to pattern separately two metal layers - the first for leads and interconnect lines, and the second for fine-scale structures. This approach works well using Au for the large-area leads, since Au does not oxidize or contaminate significantly [Bishop et al.,

The Liftoff Process

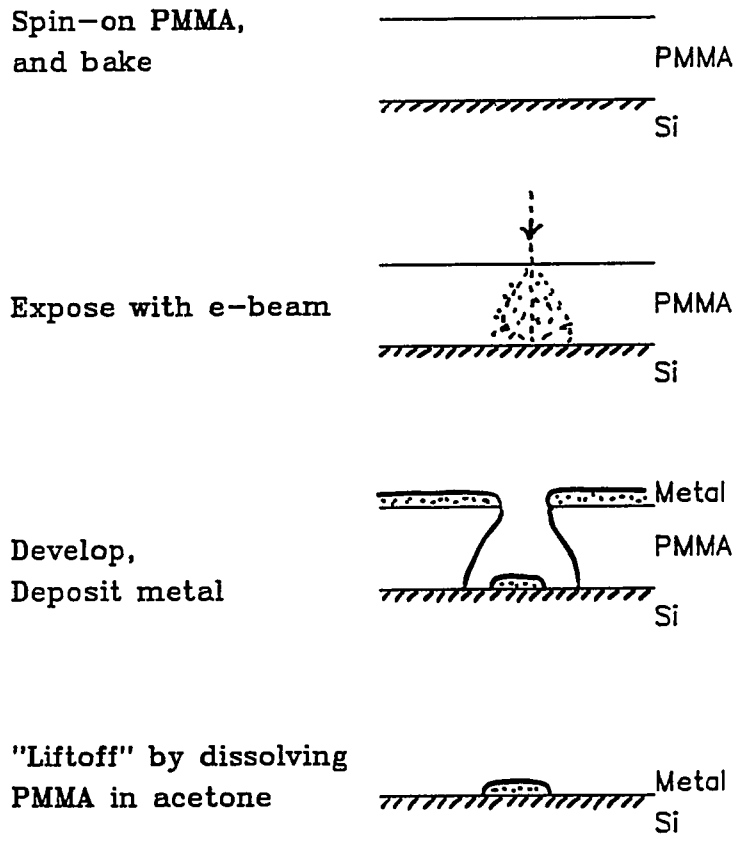

Fig. II-1: The liftoff process. The spreading of the incident beam is exaggerated.

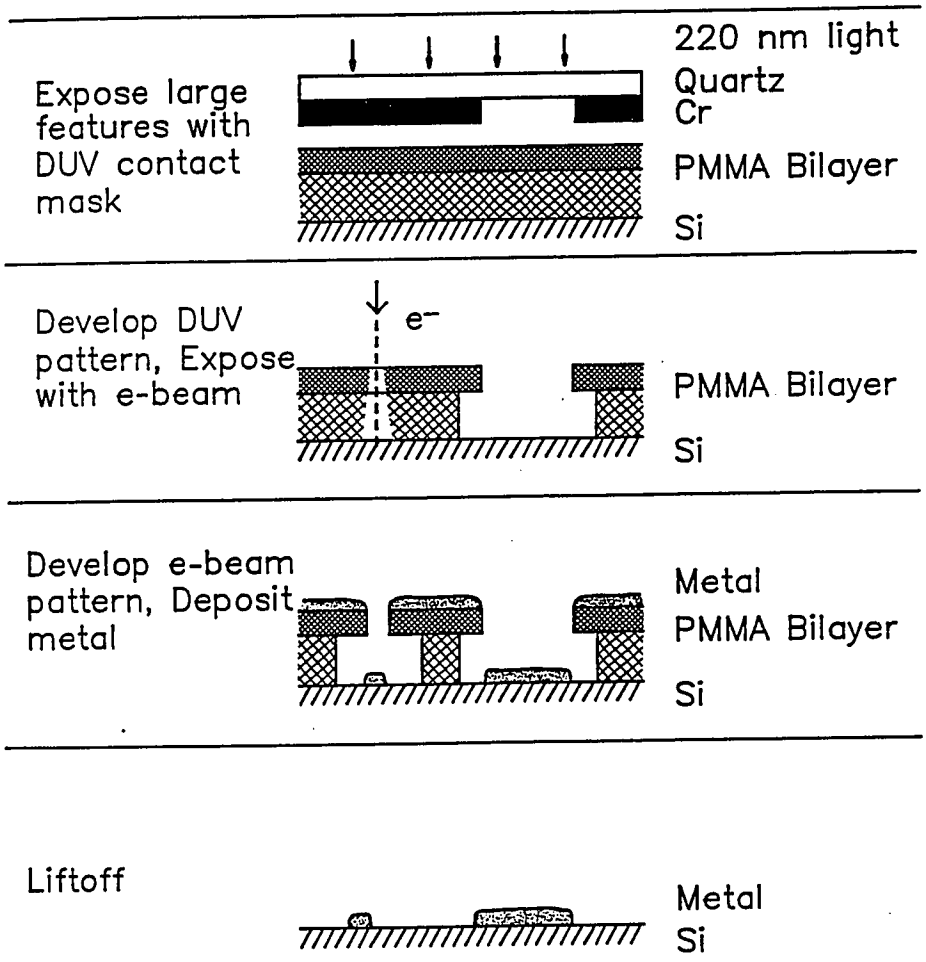

Fig. II-2: The hybrid DUV/e-beam process. The pattern produced by DUV is used for focusing and aligning the e-beam system. Large and small features are lifted-off in one step.

1985; Laibowitz et al., 1983; Molzen et al., 1980].

An alternative to the liftoff technique is the use of "contamination resist", which has demonstrated resolution below 10 nm [Broers et al.,1976]. In this technique vacuum pump oil is hardened on a metal film surface by e-beam exposure, and serves as a mask for Ar-ion etching. Although the contamination-resist technique has been very successful for experiments on Au rings [Webb et al., 1985] and Nb SQUIDs [Laibowitz et al., 1983], this method causes narrow wires to have more surface contaminants than large-area features. In this case it may be improper to use 2D films to infer the properties of 1D wires. The liftoff process has the advantage that large features used for 2D studies will have the same material properties as small features. Contamination lithography is also not well suited for patterning Al, because of the relatively low etch resistance of the contamination in a chlorine plasma [Umbach, 1985].

II.B. The Problem of Leads and Contacts

After any device is made it must be capable of surviving a minimal degree of handling, and electrical contact is often required. The largest danger in handling sub-micron devices is electrostatic discharge. To avoid currents flowing through the device, the pads are initially shorted together. Fig. II-3 shows the DUV contact-mask pattern for producing large pads. The structure is 2.5 mm × 2.5 mm. The pads are initially shorted together. After connecting wires to the pads, the shorting pattern is scratched out; in this way the leads are never left floating. Another important precaution in avoiding damage by static discharge is the use of room humidifiers and grounding straps while mounting and measuring devices.

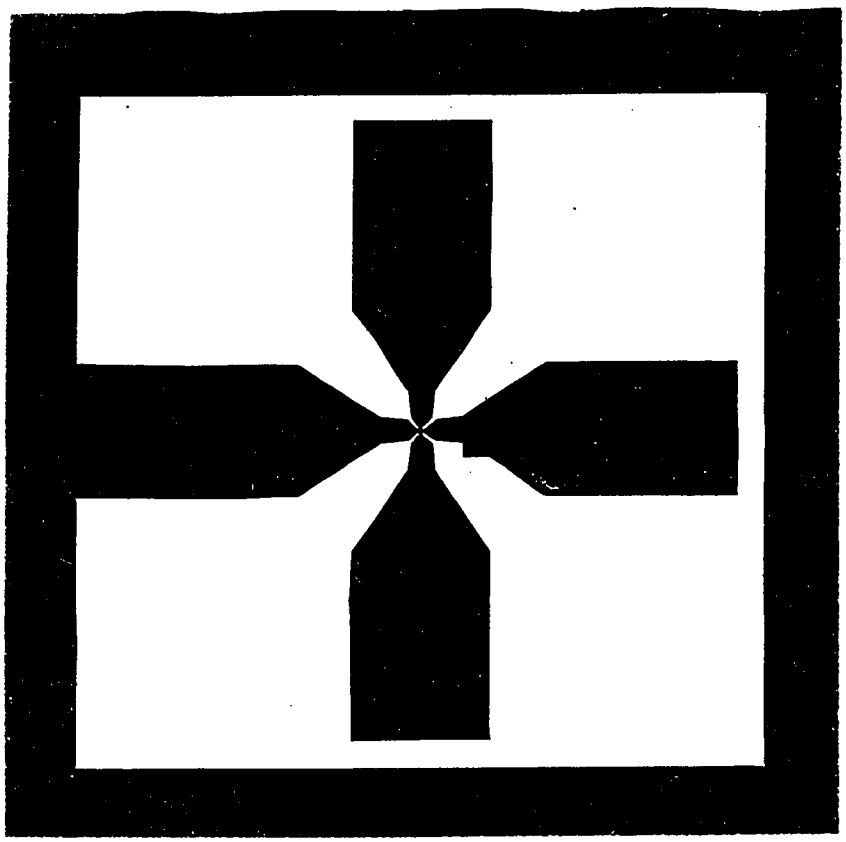

Fig. II-3: Pattern used for DUV exposure of pads. Voltage and current leads are shorted together to prevent current from flowing through the device. The pattern measures 2.5×2.5 mm on the Cr mask. The probes in the center are spaced ~40 μm apart. An intermediate pad structure is produced by e-beam, which reduces the pad spacing to ~10 μm. The high-resolution structure is drawn in a 15×15 μm field.

A variety of techniques have been used for connecting copper wires to devices. Fig. II-4 shows the methods that have been successful: gold-wire ultrasonic bonding, direct In soldering, pressed In contact, and Ag paint-to-In contacts. Wire bonding has the advantage that the pads can be very small; however, as implemented at Yale the process is complex and unreliable. Direct In soldering produces very reliable contacts. One must use a DC-powered soldering iron to avoid AC pickup in the device. The temperature must be carefully controlled to avoid damaging the device; this is more of a problem for Ag than for Al. For Pb and other low-melting-point metals direct soldering with In is unacceptable. Delicate films can be connected to wires by first melting the In next to the pads, then pressing the In into the film. A better technique (Fig. II-4d) removes the In from the wafer entirely. Ag paint is used to connect the anchored wires to the pads; neither the device nor its substrate is heated.

II.B. Deep-Ultraviolet Exposure

Polymethylmethacrylate (PMMA) can be exposed with light of wavelengths $\leq$ 240 nm [Lin, 1975, 1976]. Our DUV contact exposure masks are made with chrome (thickness > 150 nm) or aluminum (thickness > 50 nm) on 2.5 in. square, high-purity fused quartz plates. Most plates used are purchased pre-coated with Cr and photoresist [Balzers]. We use these pre-coated plates because photoresist usually does not stick well to quartz plates. We occasionally start with a blank plate, and deposit the photoresist and metal layers ourselves. In this case, a layer of Al > 50 nm Al is first evaporated. Photoresist is spun onto the Al film. The plate is

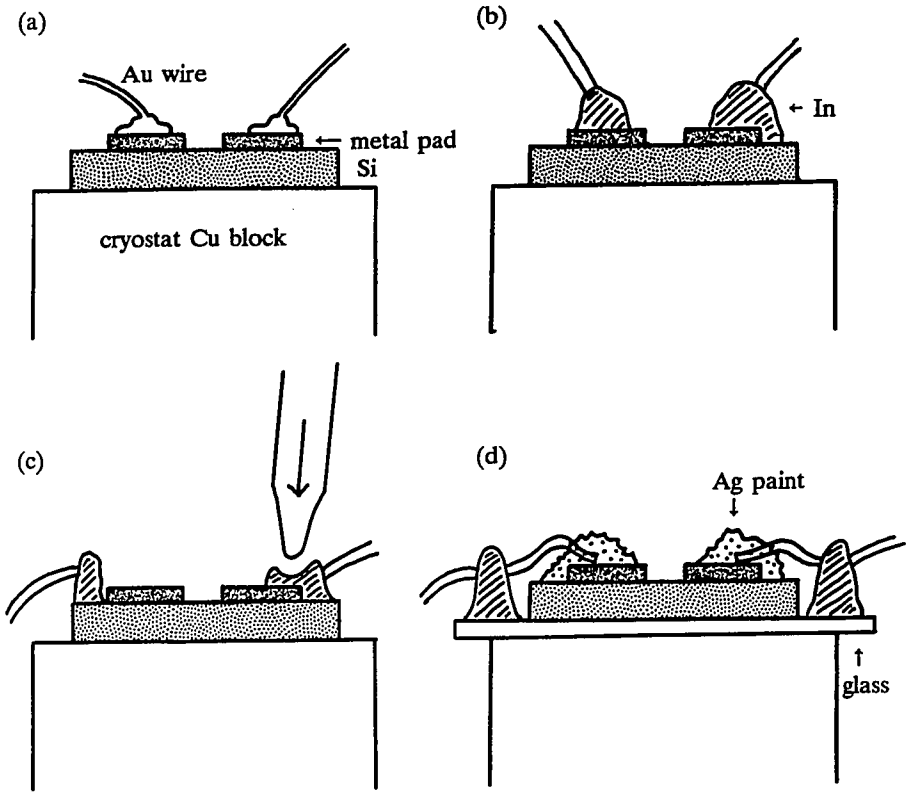

Fig. II-4: Contact methods. (a) Ultrasonic wire-bonding with Au wires, (b) direct In soldering, (c) In is melted next to the metal, then pressed into the pad, (d) In melted onto a glass cover slip supports Cu wires. Contact to pads is made with Ag paint.

secured to a spinner chuck with double-stick tape. The photoresist is then baked, exposed through an emulsion mask (made at Yale), and developed. The Al is etched in standard Al-etch [see Al-etch]. We have found that photoresist does not spin properly onto untreated Cr.

A mask aligner or a simple conformal exposure device [Feuer, 1980; Lin, 1975, 1976; Melngailis et al., 1975] is used to provide hard contact between mask and wafer. Four different light sources have been characterized: (1) a low-pressure Hg lamp (380 W) [Gates], (2) a small zinc lamp (7 W) [UVP], (3) an Oriel DUV lamp with a 500 W Ushio Hg-Xe bulb [Oriel], and (4) an HTG DUV lamp with the same Ushio bulb [HTG]. For the first three sources, an Oriel mask alignment fixture is employed (Fig. II-5). The HTG lamp is part of an HTG mask aligner system.

The following comparison of exposure times assumes a development of PMMA in MIBK:IPA (1:3). The Gates Hg and UVP Zn lamps are uncollimated (Fig. II-5) and are not filtered. An exposure time of ~1 h is required for the Gates lamp, which heats the substrate to ~83°C during exposure. The same exposure with the zinc lamp requires ~5 h, depending on the age of the lamp. Zinc has a strong spectral line at 214 nm, and is thus a far more efficient source. However, the Zn lamp is small, so the exposure is slow and is not uniform over large wafers. An advantage of Zn is that it produces almost no infrared, and so does not heat the wafer. Both the UVP and Gates lamps are relatively inexpensive.

The Oriel and HTG lamps are collimated and infrared-filtered fixtures for mask aligners. Exposure with the Oriel lamp requires 20 min. The HTG lamp requires 15 min. Both lamps provide uniform exposure over ~4 in., neither lamp heats the wafer,

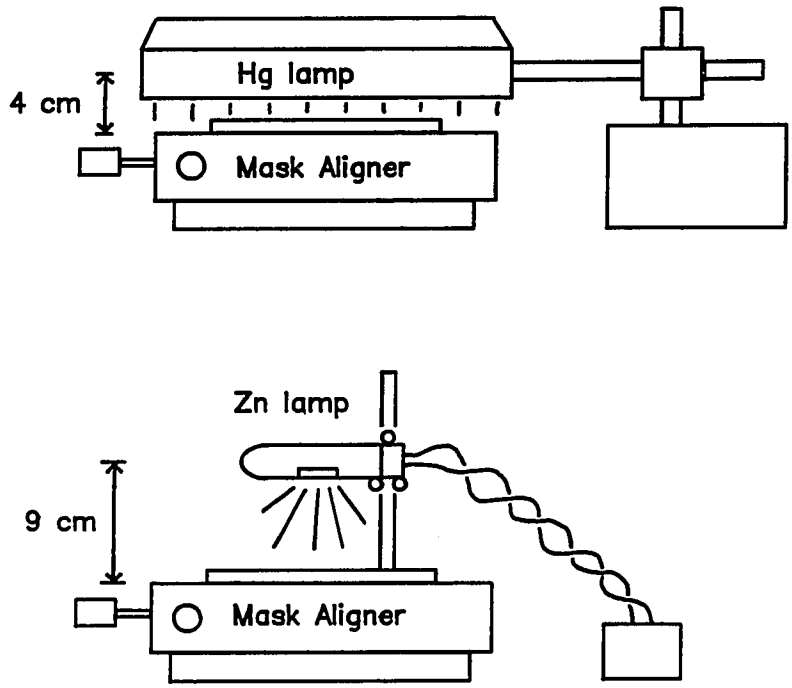

Fig II-5: Exposure using Hg and Zn lamps. The Hg bulb is placed ~4 cm from the wafer. The Zn bulb is smaller, and so is placed ~9 cm from the wafer. Both lamps are uncolumated and unfiltered. The mask alignment fixture is made by Oriel Corp.

and both are relatively expensive.

The Gates and UVP lamps are capable of *reliably* producing ~10 μm lines and spaces across a 2 in.-diameter wafer. The collimated mask-aligner lamps are capable of producing reliably ~1 μm lines and spaces across a 2 in. wafer, and are capable of producing ~0.3 μm lines in the center of the wafer.

It should be noted that, in our experience, 1:3 MIBK:IPA is *not* an optimal developer for PMMA exposed by DUV light. Much of the development time is spent clearing away a small percentage of higher molecular-weight (MW) polymer [Mackie and Beaumont, 1985, their fig. 5], which appears to remain after the developer has dissolved most of the exposed PMMA. A stronger developer, such as 1:1 MIBK:IPA, appears to eliminate this small residue layer. However, a stronger developer also slowly dissolves the unexposed resist. Although shorter exposure times and higher resolution patterning of PMMA are possible with the use of a strong developer, the thickness of unexposed PMMA is often reduced in the development process. The thickness of unexposed resist is often critical to the liftoff process, especially when a PMMA bilayer is used. This PMMA bilayer will be discussed in section II.E. The effect of the high-MW residue has been observed when using the PMMA bilayer (section II.E.), which is mixed in our lab, as well as when using commercially produced solutions of PMMA in chlorobenzene [KTI].

II.D. Electron-Beam Exposure

II.D.1. System Overview

Electron beam exposure is done with a modified ISI SS-60 scanning electron

microscope (SEM) [ISI] with an electrostatic beam-blanker from ISI (Fig. II-6). A voltage difference applied to the blanking plates causes the beam to deflect (or, "blank"), thereby preventing exposure. A Hewlett-Packard Series-200 computer sends blanking signals to the blanker, through a custom interface built at Yale. This interface controls also the scan coils of the SEM, driving the beam in a raster pattern, as shown in Fig. II-7.

Scan signals generated by the e-beam interface are mapped onto the field of view of the SEM; that is, the SEM magnification determines the size of the exposed field. The operator aligns the field to a pattern produced by DUV exposure, sets the magnification, then switches the SEM to external control for the exposure.

The following is a brief outline of the e-beam procedure:

1) A pattern is designed on the HP computer with the program GRAFF (all of the e-beam programs were written at Yale by MJR). This pattern is stored on disk as characters and rectangle coordinates.
2) The pattern is mapped onto a grid of 1024×1024 pixels by the program FILLFAST. The filled-in pattern is stored on disk.
3) The SEM is set-up for exposure; the beam-blanker is adjusted.
4) The program FASTDUMP reads the pixel grid from disk and dumps it to the e-beam interface. Each byte (8-bits) of the pattern is sliced into bits by the e-beam interface, then sent to the beam blanker.
5) Development and liftoff (or etching).

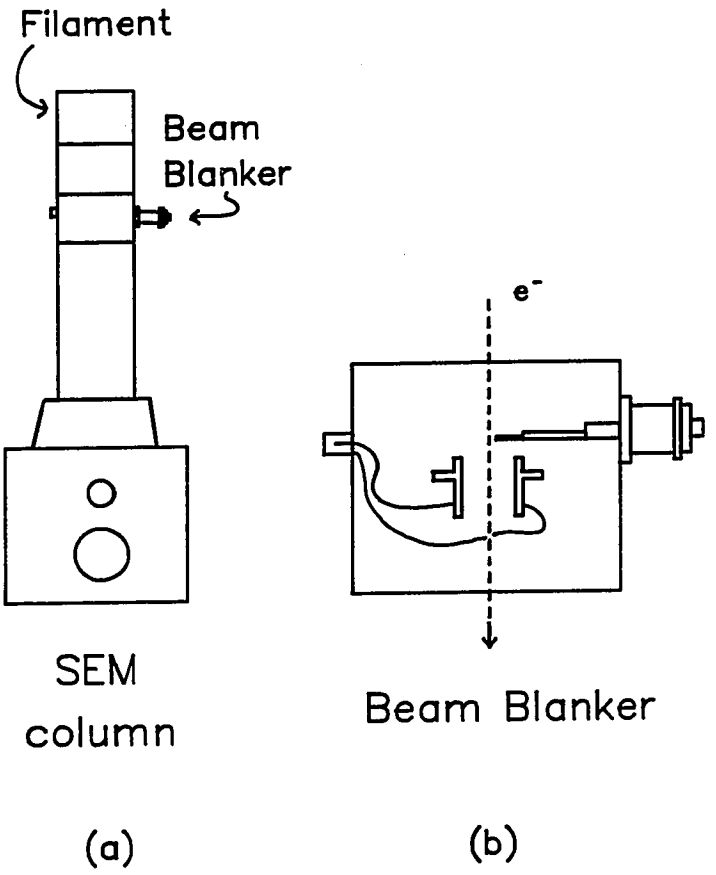

Fig. II-6: Scanning electron microscope (SEM) [ISI] with an electrostatic beam-blanker. (a) SEM column; sample chamber is at the bottom. (b) Expanded view of the beam blaking section of the column; signals fed through BNC cables charge the plates to ~18 V, thereby deflecting the beam and preventing exposure. A Mo knife-edge above the plates allows the beam to be cut completely when the plates are charged.

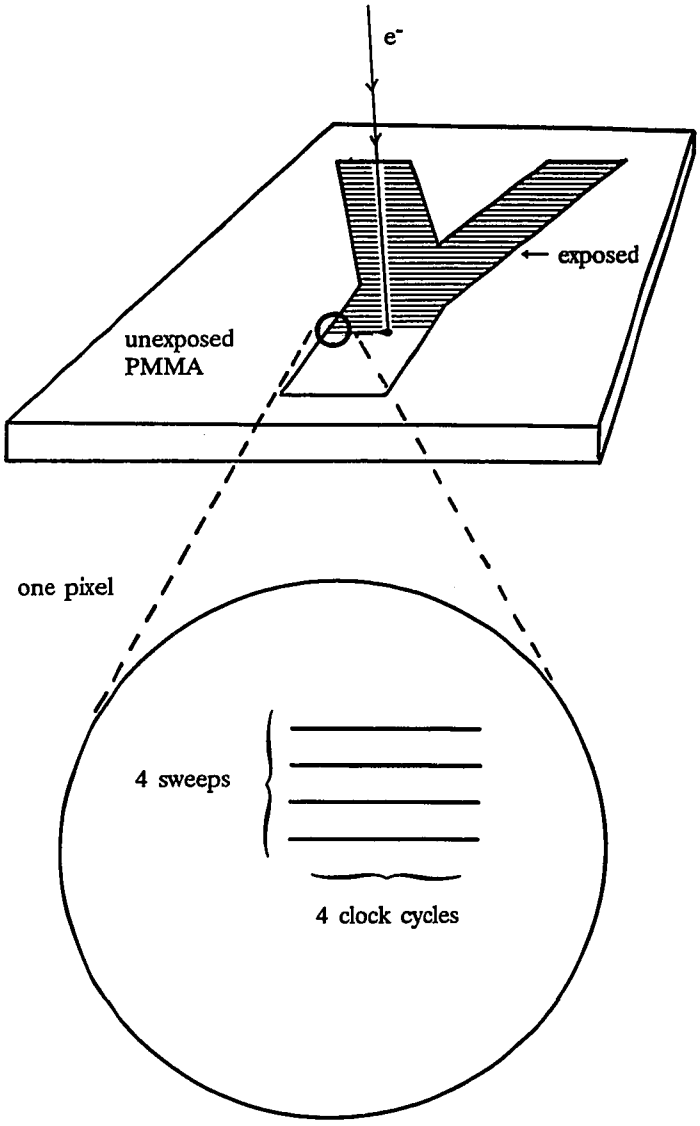

Fig. II-7: Raster-scan exposure of PMMA. Arbitrary shapes can be exposed. A full field consists of 1024×1024 pixels. Each pixel is written physically as four horizontal sweeps of four clock cycles.

II.D.2. The Beam Blanker

The beam blanker forms an extra section of the column just underneath the gun alignment coils (Fig. II-6). Two BNC cables send voltages to the plates. As little as 5 V between the plates can be used to blank the beam; however, the blanker is much easier to adjust when the blanking signal is ~18 V. Because of the convenience of producing -15 V to +15 V with standard op-amps, we apply +9 V to one plate, and -9 V to the other.

If left disconnected the blanking plates will accumulate charge from the beam. This will cause the beam to swing wildly, and then "auto-blank". Shorting plugs on the beam blanker BNCs will avoid this. When the blanker is first connected to an external device through the BNCs, this high-voltage charging can cause currents which destroy external circuit elements. To avoid this problem, a ~0.5 MΩ shunt is provided from each blanking plate to ground. This does not effect the performance of common op-amps.

A knife-edge above the blanking plates "cuts" the beam cleanly so that a relatively small voltage can be used for blanking. For normal viewing the knife-edge can be completely retracted. When using the blanker the knife-edge mechanism is pushed in, then turned slightly to lock it in place. The position of the knife-edge must be adjusted carefully to obtain maximum contrast between "on" and "off".

It is possible to do e-beam writing without a beam blanker, simply by moving the beam as quickly as possible between rectangles [Grabbe, 1980]. In this way the connections between rectangles would be too lightly exposed. Another way of

blanking the beam is by pulsing the gun alignment coils. This method is slower than the use of an electrostatic blanker, since the alignment coils have a high inductance. However, both of these techniques have the advantage that if a beam blanker is not available, modifications do not need to be made to the beam column.

II.D.3. The Raster-Scan Interface

A block diagram of the e-beam interface is shown in Fig. II-8. A clock signal drives a pair of 12-bit counters. The most significant bit of the first counter clocks the second. Digital-to-analog (DAC) chips connected to each counter then produce the X and Y raster signals. Analog raster signals are filtered, amplified, and shifted to the appropriate levels (~ ±5 V sweeps).

Each counter produces 2^{12}=4096 steps. There are 4096 clock cycles in a horizontal sweep (X), and there are 4096 scan lines. Fig. II-7 shows how the pixels are defined. Each pixel is patterned with 4 clock cycles horizontally and 4 scan lines vertically. The computer must repeat each line of the pattern four times to define a full line of pixels. There are then 1024×1024 pixels in a field. Using four sweeps spaced at the Gaussian half-width of the beam can produce a sharper exposure profile than that produced by a single sweep, and thus can produce a more uniform line [Greeneich, 1980, p.80].

Bit 3 of the X-counter (see Appx. B) is used to handshake with the computer, over the IEEE-488 (HPIB) interface. Pixels are lined up in the computer's buffer, waiting for handshake signals to allow transfer of data to the e-beam interface. One

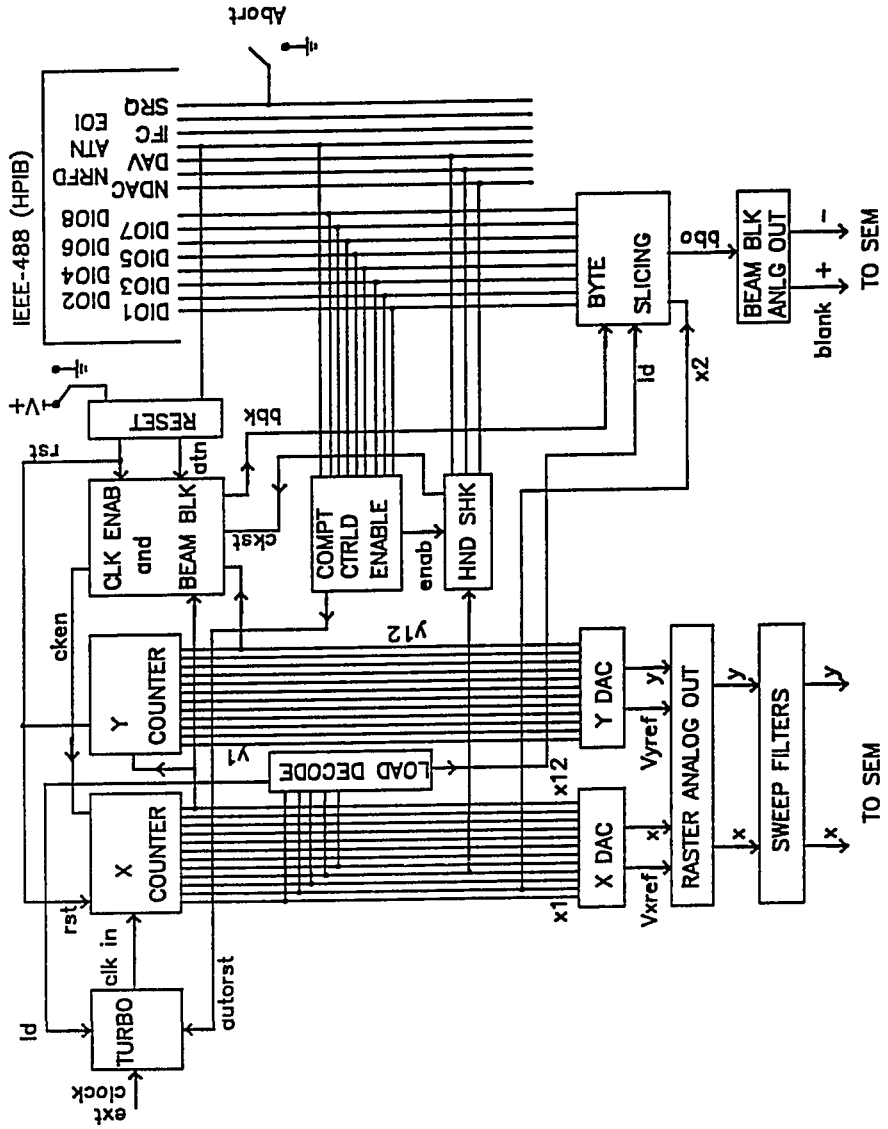

Fig. II-8: Block diagram of the electron-beam interface.

byte of pixels is transferred at each signal, and is stored in a shift register. Bit 1 of the X counter then toggles the bits out of the shift register, to be converted by op-amps into blanking signals.

Many patterns contain large blocks in which the beam is off (i.e., unexposed regions). For these sections there is no need for the beam to move slowly, and so the computer sends a signal which switches from the slow clock (an external square-wave generator) to a fast (1 MHz) internal clock. Pattern data in the buffer is interleaved with speed-control data, and a multiplexing circuit divides speed data from pattern data. Every other byte contains a "speed bit" which determines the source of the clock for the 12-bit counters. Of the eight bits in a speed byte, seven are currently unused. Switching from one clock to another must be done smoothly, so that erroneous handshaking signals will not be produced. The speed bit thus does not change clocks directly, but instead "requests" a speed change. The speed will be changed only when the external and internal clocks are in the same state. Use of the internal 1 MHz clock can increase the writing speed by as much as a factor of five over that available when using a single-speed clock.

The computer will switch back to the external clock (whose frequency is set by the lithographer) before an exposed region is reached. Because of the large inductance of the scan coils, the external clock must be selected 64 pixels ahead of the exposed region. This gives the coils time to "settle" before the beam is "unblanked". For a typical exposure, 64 pixels corresponds to a settling time of 2.5 ms - a very conservative figure.

Details of the e-beam interface can be found in Appendix B.

II.D.4. Pattern Definition

The 1024×1024 pixel grid can be filled with any graphics pattern. The program FILLFAST maps a pattern produced by GRAFF onto the grid. GRAFF is an interactive program (written at Yale by MJR) which allows the user to draw rectangles and arbitrarily-shaped characters [Wolcott and Hilsenrath, 1976]. The user can magnify sections of the pattern (zoom-in), and preview the mapping of vectors and rectangles onto pixels. A new e-beam pattern can be defined on the computer in a matter of minutes, allowing device designs to evolve rapidly.

II.D.5. Substrate Considerations

PMMA layers on oxidized Si wafers charge slightly during e-beam alignment, thereby providing increased contrast between PMMA and substrate during alignment in the SEM. Substrates such as unoxidized Si or Al provide too little charging to allow easy alignment using a resist edge. For conducting substrates, focusing and alignment marks can be made by patterning a layer of ~100 nm of Al on top of the PMMA. This Al-on-PMMA process will be discussed in section II.F. Semiconducting substrates have the advantage that static charge is conducted away from the device while at room temperature. All of the devices described in chapter IV use solid, oxidized silicon substrates. Devices fabricated on oxidized Si substrates are likely to be more susceptible to damage due to electrostatic discharges than those fabricated on unoxidized wafers; however, devices on oxidized substrates have the advantage that they can be tested for electrical continuity at room temperature.

Some of the highest resolution lithography has been done using thin-membrane substrates [Mackie and Beaumont, 1985; Broers et al., 1976]. These membranes are usually produced by growing a layer of silicon-rich silicon nitride on a silicon wafer, then etching holes through the Si from the backside with an anisotropic etchant. Use of a silicon nitride membrane as a resist support minimizes exposure from electrons backscattered from the substrate [Broers et al., 1976; Beaumont et al., 1981], and allows the use of transmission electron microscopy (TEM) for high-resolution imaging. However, other than for devices made from simple wires (e.g., rings or tunnel junctions), membranes are somewhat impractical (see for example, [Lee et al., 1987]). Moreover, the effects of backscattered electrons can be minimized through the use of high beam energies (> 50 kV) [Broers, 1981; Joy, 1983; Jackel et al., 1984], and wires as narrow as those on membranes can be made by employing a thin imaging resist [Beaumont et al., 1982]. (Note: a comparison of lithographic results will be made in section II.E.5.)

II.D.6. Exposure Parameters for Single-Layer PMMA

Beam current is measured by focusing the electrons into a Faraday cup (Fig. II-9) which is connected to a specimen current meter. The standard process for single-layer PMMA is given in Appendix A. Exposure doses for this process are approximately 100 $\mu C/cm^2$. Dense patterns require less dose, because of exposure due to the secondary electrons from adjacent exposed regions. This "proximity effect" is of great importance in commercial lithography, where patterns are commonly very dense. The proximity effect is discussed by Greeneich [1980], and references therein. For the simple patterns used at Yale, proximity corrections are made iteratively by the lithographer based on intuition and experience. One quickly gains an intuition

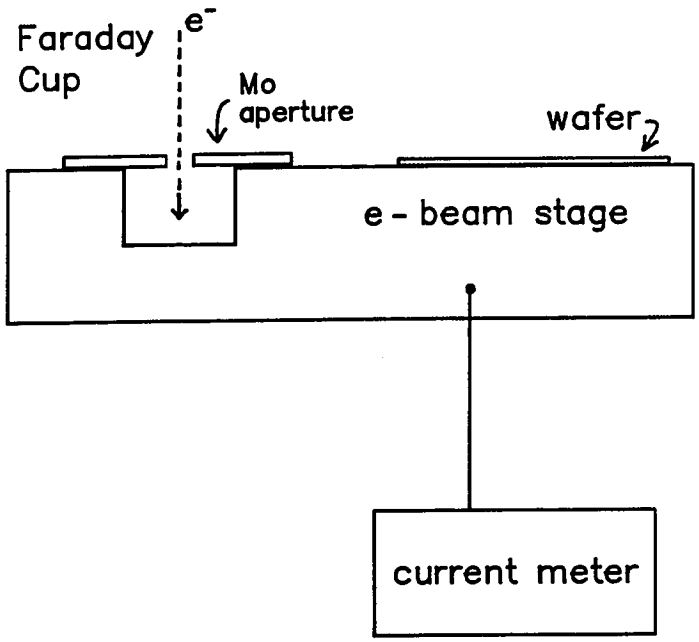

Fig. II-9: Faraday cup for measuring beam current. A 60 μm diameter Mo aperture is used to cover a well in the sample holder. The wafer is held down by Be-Cu clips, by colloidal graphite, or by Ag-paint.

for the effect.

Using a single layer of PMMA (molecular weight = 950K) ~300 nm thick, metal lines as narrow as 90 nm have been fabricated at Yale. Exposures use a 30 kV beam with a current of 10-20 pA in a field of 12 μm × 12 μm. Lines were drawn with single-line sweeps of the electron beam, using a dose of ~4 nC/cm. It is possible to produce much narrower lines, using a thin resist; however, metals such as aluminum tend to creep over the resist edge, and so require either a thicker resist or a substantially undercut resist profile. In contrast, materials such as chrome and gold can be patterned easily with thin ($\lesssim$ 100 nm) PMMA resist. Sputtered materials (e.g. Nb, Ta, or W) also require a strongly undercut resist profile, since sputter deposition is not highly directional. For this reason we have implemented a bilayer resist system, which is described in the next section.

II.E. The PMMA/PMMA Bilayer Resist

II.E.1. Multilayer resists

There are numerous process requirements which motivate the use of multilayer resists [Lin, 1983]. High resolution patterning is best achieved through the use of a thin imaging layer. However, good step coverage over existing features, and an undercut profile for liftoff processing [Grobman et al., 1979; Hatzakis, 1979; Howard et al., 1981] are best achieved through the use of a thicker lower layer.

The typical problem encountered with a multilayer resist approach is that the two resist layers may intermix. In addition to reducing the effectiveness of either layer, the thin intermixed layer can prevent proper exposure or development of the

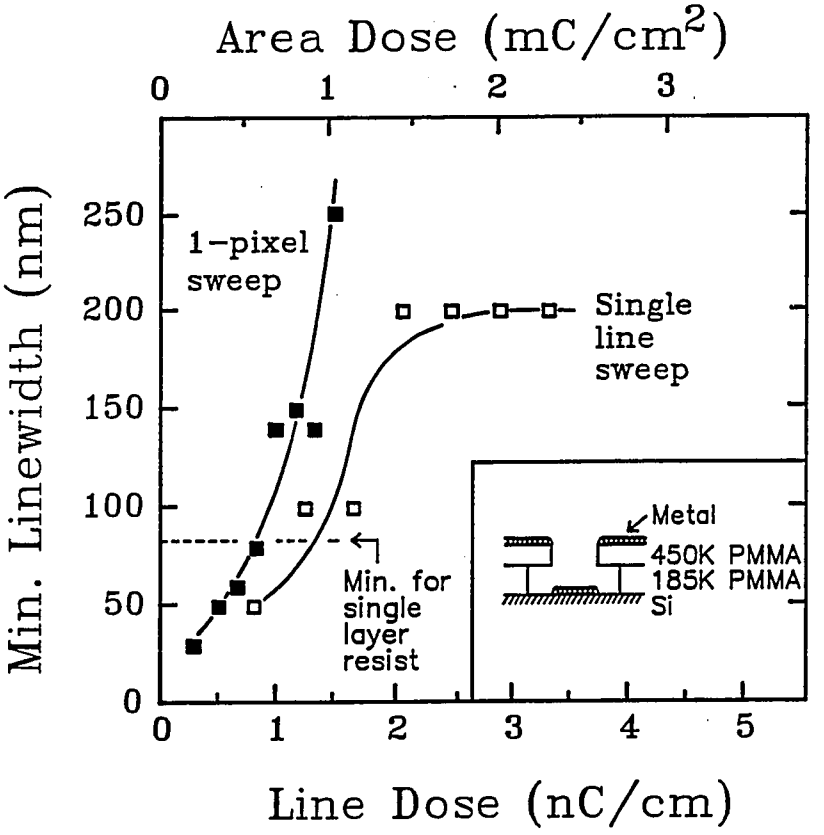

Fig. II-10: Minimum width of metal lines vs. dose for the PMMA/PMMA bilayer system. Area dose applies only for the 1-pixel wide sweep; the width of the one-pixel sweep is 15 nm = (field size)÷1024. (Area dose) = (Line dose)÷(15 nm). Inset: bilayer resist profile. From [Rooks et al., 1987].

bottom layer [Lin, 1983]. The intermixing between resist layers can be eliminated by including a separation layer of such materials as aluminum, anti-reflection coatings, or spin-on glasses. These techniques suffer from excessively complex processing. Intermixing can also be avoided simply by using materials which do not react with each other or with the solvent of the other layer.

The bilayer process described here was developed at the University of Glasgow [Mackie and Beaumont, 1985]. This PMMA/PMMA bilayer consists of two layers of PMMA of different molecular weights, with the higher molecular weight (lower sensitivity) polymer as the top layer. (See Fig. II-10, inset.) Both layers are exposed with a single exposure, and then developed with one development step.

II.E.2. Techniques and Processing For The PMMA Bilayer

The PMMA/PMMA bilayer uses a sensitive bottom layer of PMMA (molecular weight 185K) [BDH] covered with a less sensitive top layer of PMMA (molecular weight 450K) [Aldrich]. The resist structure is shown in the inset of Fig. II-10, and the processing steps are outlined in Table II-1. The solubility of PMMA in developer is greater for a lower molecular weight. As a result the bottom layer is approximately 1.5 times more sensitive than the top layer (according to [Mackie and Beaumont, 1985]). Thus, upon development the bilayer forms an undercut profile, as shown schematically in Fig. II-10.

The resist casting solvent must be chosen carefully in order to avoid mixing of the layers. If a solution of PMMA in chlorobenzene (the solvent commonly used) is spun on top of a baked layer of PMMA, the chlorobenzene partially dissolves the

bottom layer. To avoid this we have used xylene as the solvent for the top layer, since xylene is only a very weak solvent for PMMA. Most of the xylene evaporates from the top layer before any significant part of the bottom layer is dissolved. (Mixing due to subsequent thermal interdiffusion appears to be negligible.) It is also reportedly possible to use acetic acid as the solvent [Mackie, 1985]. The two layers of PMMA are developed at one time with the same weak developer (1:3 MIBK:IPA), so that any small interdiffused layer simply forms a thin region of intermediate sensitivity. The lack of intermixing is indicated by the liftoff properties of the bilayer, which are significantly better than those of a single PMMA layer of the same total thickness.

Table II-1: Processing steps for the PMMA bilayer.

1. Clean and oxidize silicon wafer.
2. Spin 185K PMMA, 3% in xylene, at 2500 rpm for 1 minute (thickness ~58 nm).
3. Bake for 1 hour in air at 180°C.
4. Spin 450K PMMA, 3% in xylene, at 7000-9000 rpm for 1 minute (thickness ~40 nm).
5. Bake for 2 hours in air at 180°C.
6. Expose with DUV using contact mask.
7. Develop for 30 sec in 1:3 MIBK:IPA, 23°C.
8. Expose with e-beam (see Fig. II-10).
9. Develop for 30 sec. in 1:3 MIBK:IPA, 23°C.
10. Clean with oxygen glow discharge in evaporator.
11. Evaporate metal.
12. Liftoff by shooting acetone.

Solutions are prepared as ~3% PMMA solids in xylene. During preparation the mixtures are magnetically stirred in closed glass containers. Since xylene is an inefficient solvent, it is necessary to stir for 24 hours at a temperature of 60°C. Resist solutions are filtered twice through 0.2 μm Millipore filters, and are stored at room temperature. The solutions show no signs of precipitation.

Thicknesses of single resist layers have been measured for different spin speeds. The resist thickness was measured with a Dektak stylus machine with a resolution of 5 nm. Thicknesses of spun-on 450K PMMA range between 92 nm for a spin speed of 2000 rpm to 45 nm at 8000 rpm. Thicknesses of the 185K PMMA range between 65 nm at 2000 rpm to 32.5 nm at 8000 rpm. Both molecular weights of PMMA spin uniformly to ±20% over a 1.5 in. oxidized Si wafer. A similar measurement of thickness was made to determine the loss of unexposed resist due to a standard 30-second development in 1:3 MIBK:IPA at 23°C (step 7 in Table II-1). The resist thickness loss was < 5 nm. An oxygen glow-discharge cleaning is used prior to metallization (step 10); the thickness loss due to this cleaning was also < 5 nm. A stronger developer, 1:1 MIBK:IPA, decreases the thickness of the upper layer to the extent that liftoff of aluminum is no longer possible.

II.E.3. Exposure Parameters and Lithography Results

The typical exposure field is 15 μm x 15 μm, for a pixel size of 15 nm x 15 nm. This is the field size used for exposure of the rings and lines described in chapter IV. Each pixel in the pattern is exposed with four single-line horizontal sweeps whose line centers are offset by 3.7 nm (1/4 pixel) between each sweep. For

tests of minimum achievable linewidths, we employ exposures either one pixel (four sweeps) wide, or 1/4 pixel (one sweep) wide. The beam energy commonly used is 30 keV, and the beam current used for a 15 μm x 15 μm field is 15 pA.

Fig. II-10 shows our result for linewidth vs. dose for the bilayer resist. Linewidths are measured with a JEOL 100CX in the SEM mode. Measured linewidths are consistent with electrical measurements on several samples. The smallest linewidth of metal lines is 30 nm. Aluminum lines as narrow as 35 nm have been used for studies of electron-electron interactions (see chapters III and IV). The single-line exposure and the 1-pixel-wide exposure produce comparable linewidths. Fig. II-10 shows that the 1-pixel sweep produced a narrower minimum linewidth in this particular test. A single-line sweep can apparently produce a 30-nm wide line as well, although this may require tighter control of processing parameters than for the 1-pixel-wide exposure.

Fig. II-11 shows a TEM micrograph of the PMMA/PMMA bilayer resist profile. Samples for TEM studies are prepared by the following process:

1) Spin polyimide on a substrate of KCl. Bake at 300°C for 1 h.
2) Spin the PMMA bilayer, as shown in Table II-1.
3) Expose a large test pattern with e-beam. Develop in MIBK:IPA 1:3 for 30 s at 23°C.
4) Using an rf plasma, sputter ~10 nm of Au-Pd onto the resist profile.
5) Place the KCl crystal in a beaker of water. The substrate dissolves, leaving (from the bottom up) polyimide, PMMA bilayer, and Au-Pd. The film floats on the water's surface.

6) Pick up the film with a loop of wire, and place the film in an embedding cast.

7) Pour in embedding epoxy, and dry overnight.

8) Slice thin sections for TEM with a diamond-knife microtome.

The layers of PMMA shown in Fig. II-11 may be somewhat thicker than the PMMA layers used with Si substrates; also, the electron beam used for this exposure is more diffuse than the beam used for high-resolution exposures, due to the larger field size and higher beam current employed. In any case, the undercut nature of the profile is clearly evident. Fig. II-12 shows a test pattern of Au on an oxidized Si substrate. The lines shown in Fig. II-12 are 45 nm wide, with a 150 nm pitch. This pattern indicates that the lateral extent of the undercut cannot be more than ~50 nm from the resist edge. Fig. II-13 shows several other test patterns of lifted-off metal.

II.E.5. Comparison With Other Work

Significant bilayer resist techniques for e-beam lithography were first presented by Hatzakis [1979] and Grobman et al. [1979]. One such process uses a bilayer consisting of a layer of PMMA and a layer of a copolymer, poly(methyl-methacrylate/methacrylic acid). The solvent used for each layer does not dissolve the other layer. For high sensitivity (low exposure dose) the copolymer is the top (imaging) layer. For high resolution PMMA is used as the imaging layer [Howard et al., 1981]. This latter bilayer system has produced metal lines as narrow as 35 nm with an SEM exposure system. Narrower linewidths can presumably be achieved with a higher resolution exposure system.

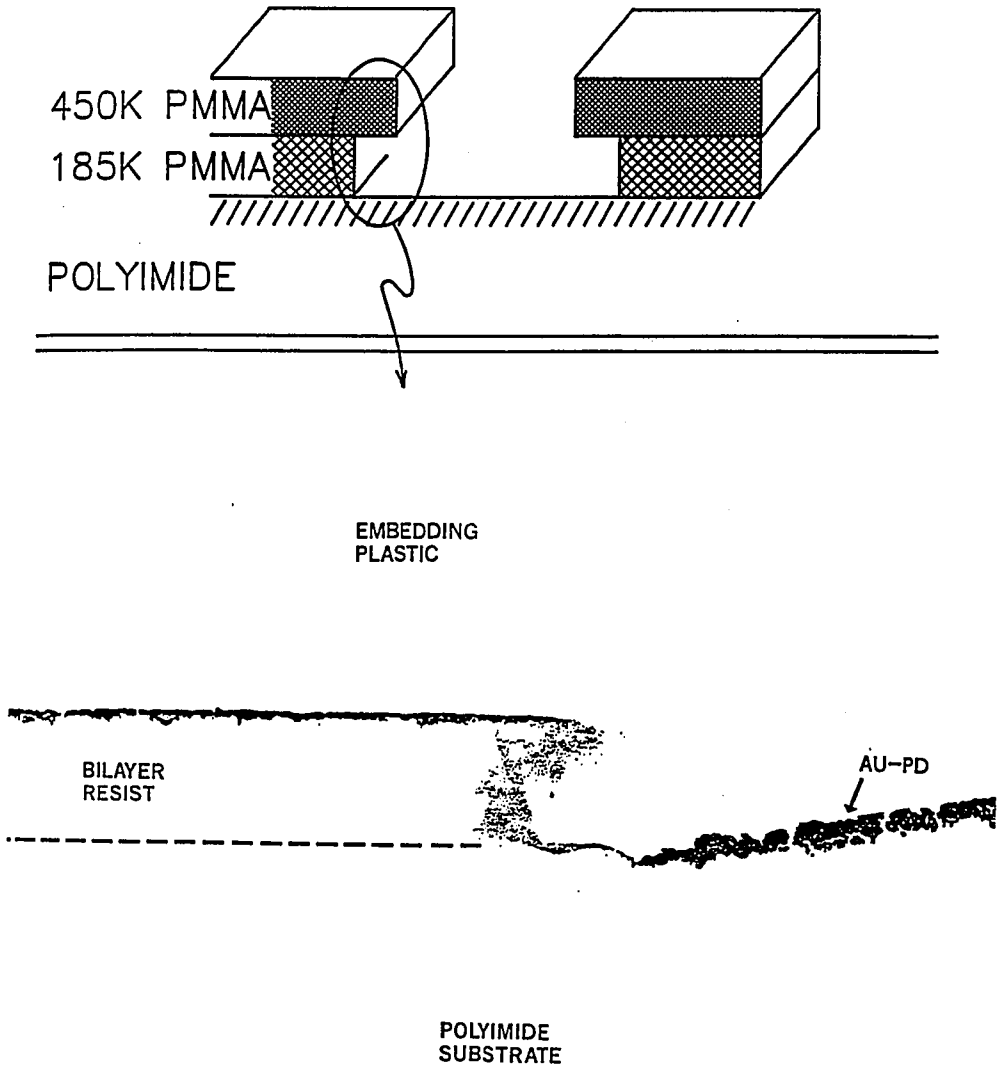

Fig. II-11: TEM micrograph of the PMMA/PMMA bilayer resist profile. Bilayer resist is spun onto a substrate of polyimide. After exposure and development the sample is coated with Au-Pd, then embedded in epoxy. Thin samples are prepared by slicing with microtome. The resist used for this sample may be thicker than the resist used for Si substrates. From [Rooks et al., 1987].

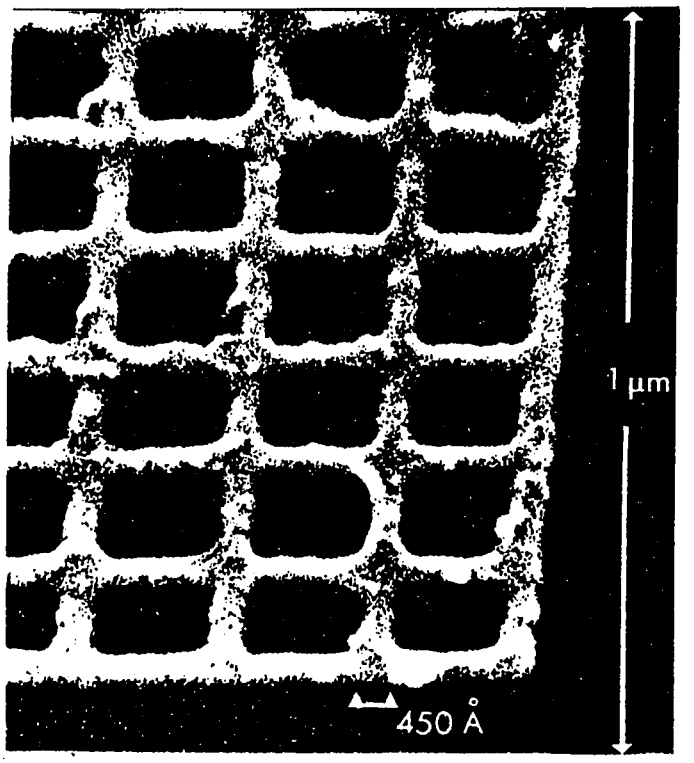

Fig. II-12: Test pattern of Au on an oxidized Si substrate. The lines are 45 nm wide, with a 150 nm pitch. This pattern indicates that the lateral extent of the undercut cannot be more than ~50 nm from the resist edge. From [Rooks et al., 1987].

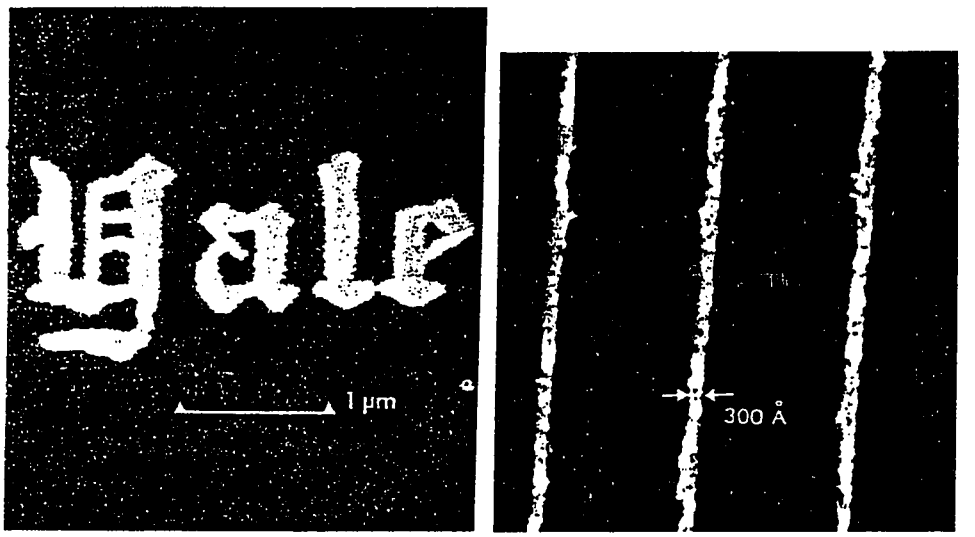

Fig. II-13: Examples of lifted-off Au patterns on oxidized Si substrates. From [Rooks et al., 1987].

With the PMMA/PMMA bilayer approach described above, Mackie and Beaumont [1985] have achieved narrower minimum linewidths (10 nm). Their beam size was ~8 nm, as determined in a transmission measurement; this appears to be smaller than our beam size. Their smaller beam size results from their use of higher beam energy, and from their ability to focus and stigmate in the transmission mode.

With a PMMA/copolymer bilayer, Howard and co-workers have reported a minimum linewidth of 35 nm in early work using an SEM exposure system. That linewidth, like ours, was most likely limited by the exposure tool. In later studies [Craighead et al., 1983; Mankiewich et al., 1986], STEM exposure of single-layer PMMA on a thick substrate allowed liftoff patterning of 10 nm Au-Pd lines. The PMMA/copolymer bilayer has an advantage relative to our PMMA/PMMA bilayer that one can use mutually exclusive developers, which allows better control of the amount of undercut, especially for large undercuts. However, for achieving the more vertical liftoff profiles needed for dense patterns, the PMMA/PMMA bilayer may be preferable since only one development time needs to be tightly controlled.

II.F. Junction Fabrication

II.F.1. The Step-Junction Technique

Junctions are fabricated with a process originally designed for photolithography by Dean W. Face [Face et al., 1986; Face, 1987; Face and Prober, 1987]. This process is shown in Fig. II-14. A step in Si or oxidized Si is made by reactive-ion etching [Face, 1987]. Metal evaporated at an angle serves as the base electrode. The base electrode is exposed to oxygen, to form a tunneling oxide. The sample is

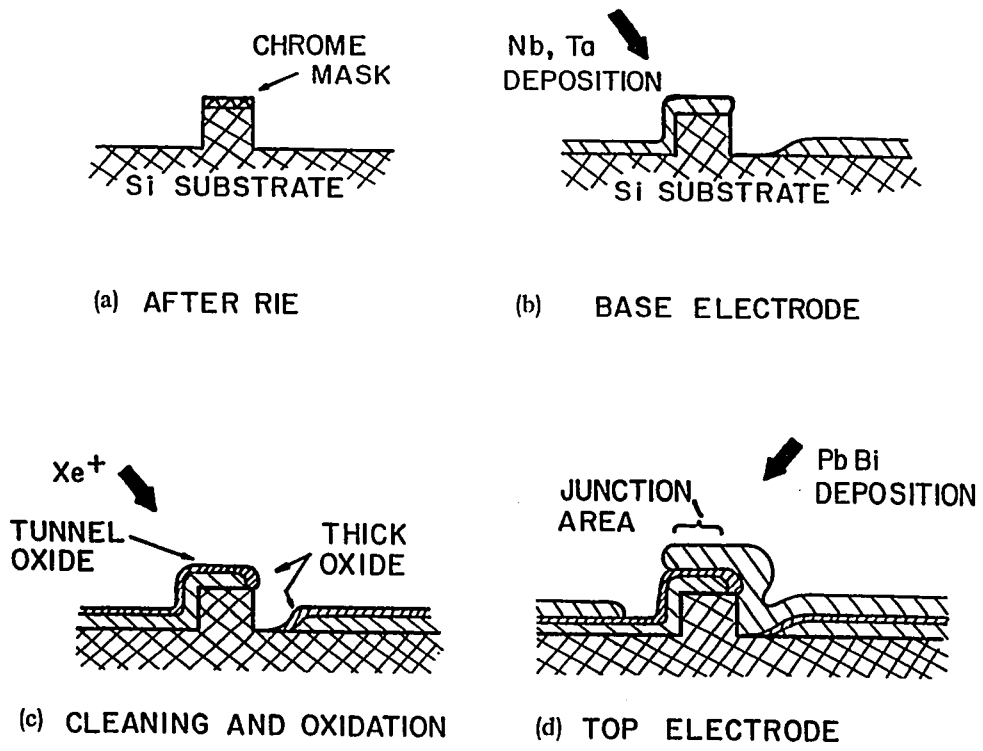

Fig. II-14: Step-defined junction fabrication process (cross section) shown here for a Ta/PbBi junction. Al/Al and Al/Pb electrode deposition can be done *in situ*, and so the ion-beam cleaning of step (c) is not necessary. From [Face et al., 1986].

then tilted in the other direction, and metal is evaporated to form the counterelectrode. Tunneling occurs only at the top of the step. The dimension of the junction into the page is determined by a liftoff mask, as shown in Fig. II-15.

For the purposes of the "normal-QUID" experiment (see chapters III and IV), two junctions are fabricated in parallel on the same step. Fig. II-16 shows a side view and a top view of a double-junction structure.

II.F.2. Electron-Beam Implementation of the Step-Junction Technique: Alignment Problems and the Al-on-PMMA Technique

We will first summarize briefly the process sequence, then discuss the specific details. The full fabrication process is given in Table II-2. Steps for the junctions are produced by first patterning lines of Cr on a Si wafer, then using the Cr as an etch mask for RIE [Face et al., 1986]. The Si (or SiO_2) is etched uniformly, except for regions covered by Cr. The Cr is later stripped (with Cr etchant) , and the wafer is coated with a single layer of PMMA resist. This resist is patterned to define the contacts of the junction (Fig. II-15,16). The liftoff mask must be accurately aligned to the step. Alignment is a simple matter in *photo*lithography, because one can see through the resist using red light. In the electron-beam process the step is hidden beneath a layer of PMMA which is effectively electron-opaque. Alignment of the junction pattern to the step is made possible by etching alignment marks along with the steps, as shown in Fig. II-17. These marks are designed to appear after the DUV exposure and development of the pad areas. The alignment marks are thus visible during e-beam alignment.

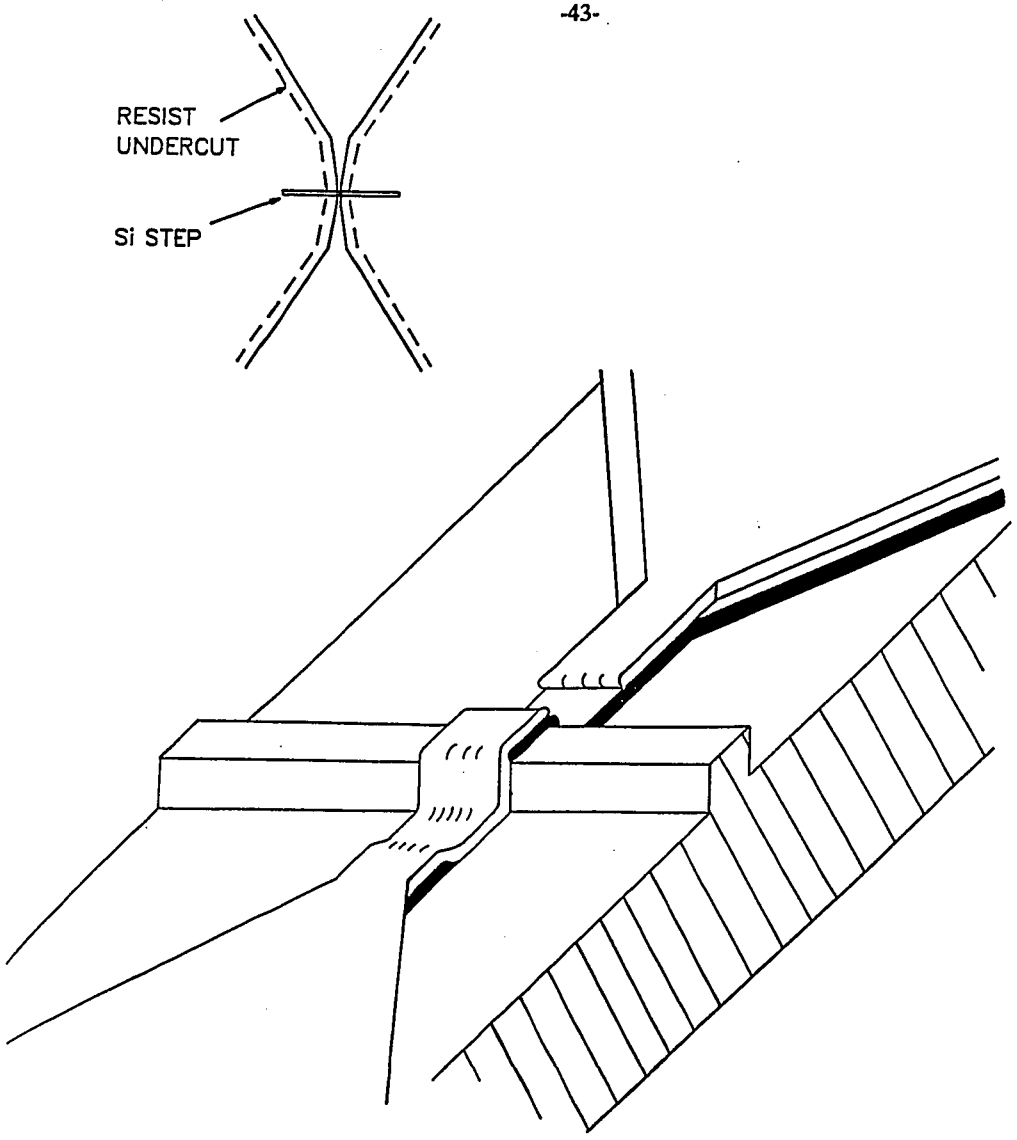

Fig II-15: Top: liftoff mask (top view) which defines the width of a junction. Bottom: junction after liftoff, showing the two metal layers. Current may flow through the bottom electrode (from the top of the figure), through the junction at the top of the step, then through the upper electrode (toward the bottom of the figure). From [Face and Prober, 1987].

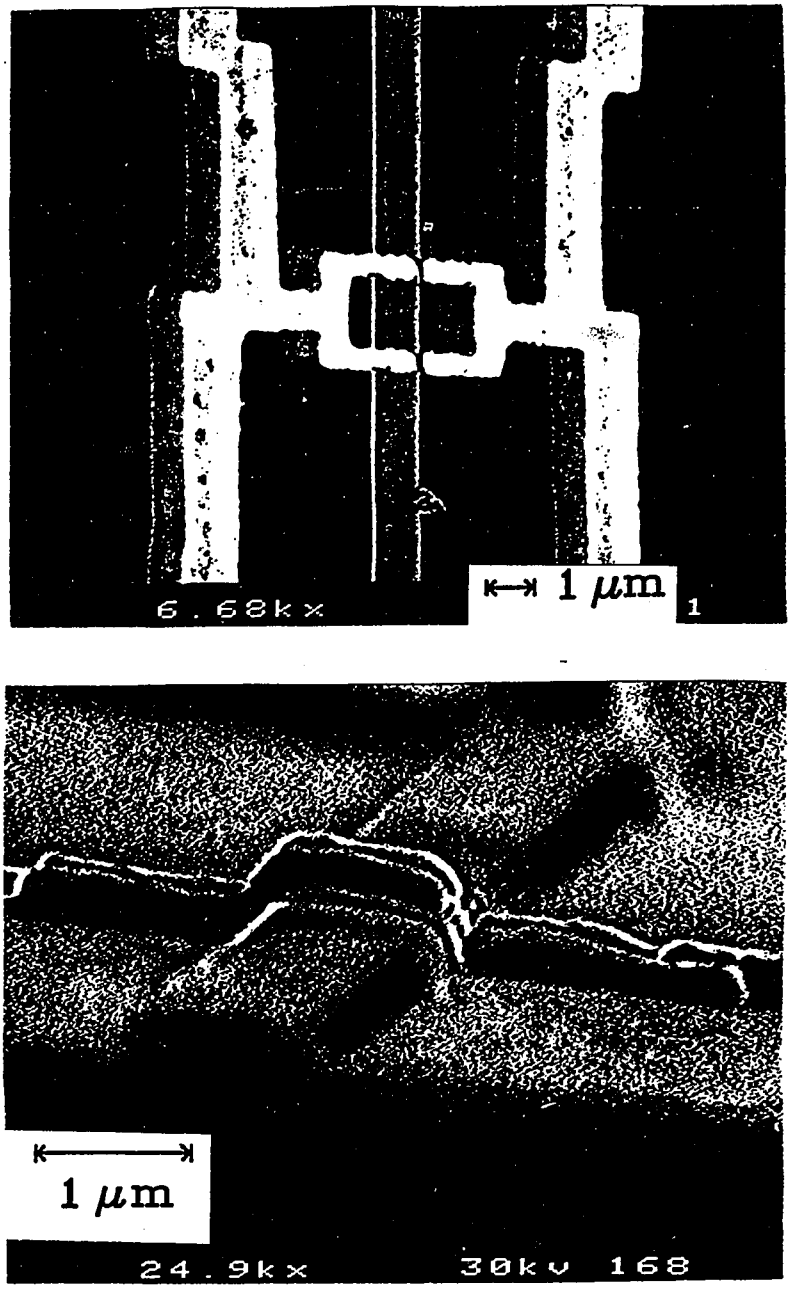

Fig. II-16: Top and side views of an $Al/Al_2O_3/Pb$ double-junction structure (for the normal-QUID experiment).

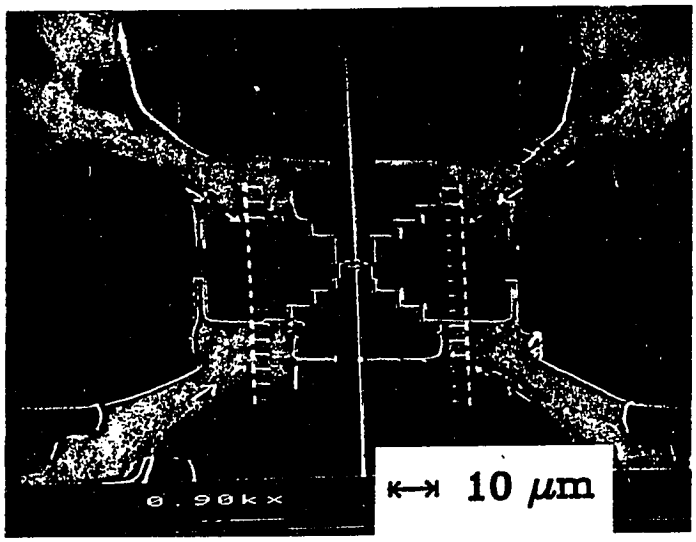

Fig. II-17: View of a double-junction device. The step runs vertically through the center. In the corners of the micrograph are large step patterns which allow alignment of the DUV pattern. DUV pads extend in from the corners, overlapping the e-beam pattern. During e-beam alignment some of the "T"s appear in the DUV-exposed pad areas, allowing alignment of the e-beam pattern to the step. The step cannot be seen during e-beam alignment.

The electron-beam process differs in another significant way from the photo process: steps must be made with e-beam (to make them narrow), and must be aligned to pads after they have been made. Fig. II-18 shows why this is a problem. Steps must be positioned across a wafer in such a way that the 2.5 in DUV pad mask can later be aligned. The steps must appear in the center of each pad structure, *over the entire wafer.* It is easy to imagine an e-beam system equipped with an automated laser-interferometer stage, which positions each step to within 0.1 μm from the center of the pads; this would eliminate the entire problem of aligning pads to steps. Using an SEM with a standard stage, it is not possible to position each step accurately over an entire wafer.

When using the e-beam system to draw a step pattern, there would normally be no *a priori* way of knowing the positions of the DUV pads (recall that the pads are exposed after the steps are made). One very simple solution is to pattern an image of the pads on top of the PMMA, then use this image to align the step pattern. A layer of ~100 nm of Al is evaporated onto the PMMA, then coated with photoresist. The photoresist is exposed with the pad mask, and the Al is etched with standard Al-etch [see ref. Al-etch]. Photoresist developer (MF-312) is used to complete the aluminum etching, since it does not attack PMMA. Steps are exposed in PMMA through the large open areas in the Al. Within a die the steps are offset from the center; however, the die-to-die step spacing is correct, and so proper alignment requires only a simple shift of the DUV pad mask (see Fig. II-19). The image of the pads is etched off of the PMMA (using MF-312) before development of the step pattern.

The Al-on-PMMA technique allows very accurate die-to-die alignment, even with

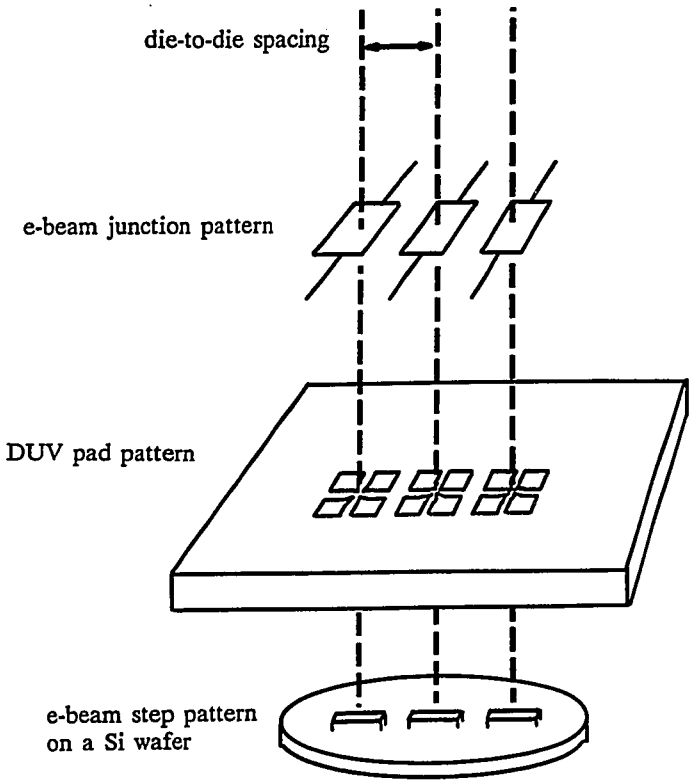

Fig II-18: E-beam/optical alignment for junction fabrication. Bottom: Steps are positioned across a wafer in such a way that the 2.5 in DUV pad mask can later be aligned. The steps must appear in the center of each pad structure, over the entire wafer. Steps are aligned to an Al pattern which sits on top of the PMMA. The step pattern contains alignment marks (not shown above) which allow alignment of the DUV mask. Smaller alignment marks in the step pattern allow alignment of the e-beam junction pattern to the central step. Middle: The DUV pad mask is aligned to the steps. Top: After DUV exposure and development, junction liftoff patterns can be aligned to the pad pattern.

a very modest e-beam stage. An alternative (and far more complex) method is to use a separate pattern of alignment marks (requiring a separate mask). The Al marks have the added benefit that they serve as focus and stigmation marks (Fig. II-20).

Once the steps have been etched to a height of ~400 nm, a thick layer (~600 nm) of PMMA is spun on the wafer and baked (see Appx. A). A mask aligner is used to align the pad mask to the steps (note that the step pattern includes features large enough to be seen in an optical microscope). The pads are exposed with DUV light, developed, and then placed in the e-beam system for exposure of the junction pattern. Table II-2 shows the complete process for e-beam step-junctions.

II.F.3. Materials Considerations

The step-junction method has had great success using tantalum base electrodes and Pb-Bi alloy counterelectrodes [Face, 1986]. The electron-beam implementation of this process has produced junction areas as small as 0.2 μm × 0.4 μm, and even smaller areas are feasible. For the current set of experiments on "normal-QUIDs", we have attempted $Al/Al_2O_3/Al$ and $Al/Al_2O_3/Pb$ junctions. The oxidation parameters and deposition techniques for these materials have not yet been fully developed. Preliminary results on these devices are discussed in section IV.D.

Al – on – PMMA Alignment Marks

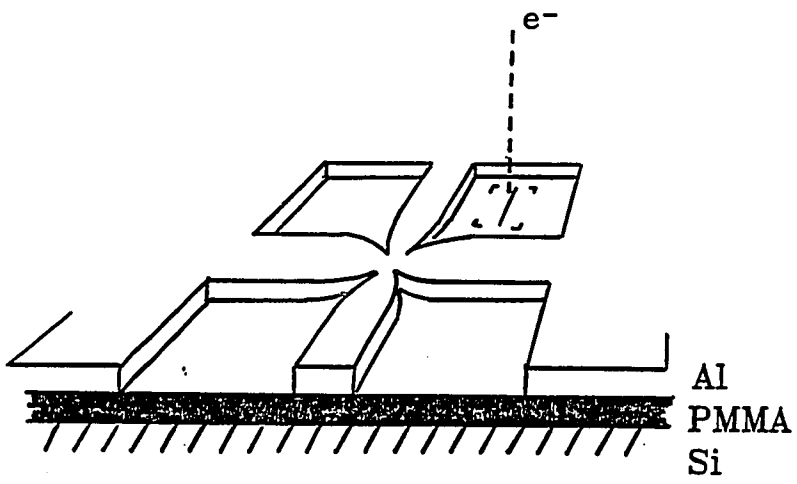

Fig. II-19: Al-on-PMMA alignment technique. Shown here is processing step #13 from Table II-2. Steps are exposed in PMMA through holes in the Al. Within a die the steps are offset from the center; however, the die-to-die step spacing is correct, and so proper alignment requires only a simple shift of the DUV pad mask. The image of the pads is etched off of the PMMA (using MF-312) before development of the step patern.

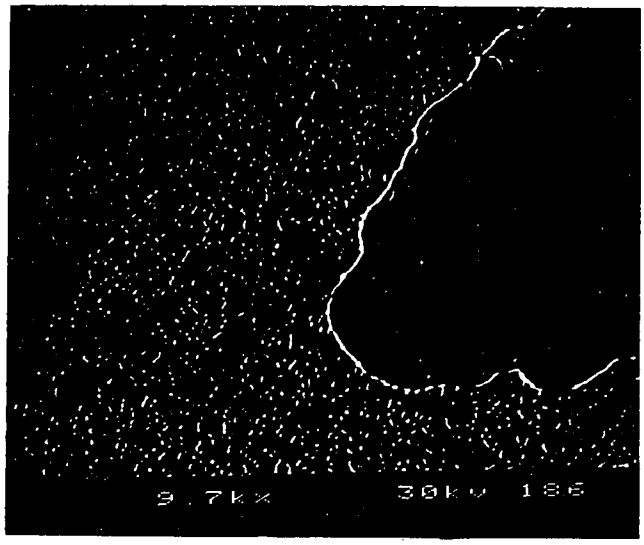

Fig. II-20: Al on PMMA pattern used for alignment, focus, and stigmation. Removal of photoresist with developer leaves a rough pattern on the Al.

Table II-2: Electron-Beam Step-Junction Process

Preparation for Step Pattern -- Fabrication of Alignment Marks

1. Clean a Si wafer [Face, 1987]
2. Optionally, oxidize the wafer.
3. Spin PMMA, 4% in chlorobezene, 950K MW, at 4000 rpm for 1 min.
4. Bake at 180°C for 30 min.
5. Evaporate > 100 nm Al at ~10^{-5} Torr.
6. Spin MP1450B photoresist at 3000 rpm for 1 min.
7. Bake for 10 min at 85°C
8. Expose the photoresist in UV light using the pad mask.
9. Develop photoresist in MF-312:water (1:1) for 1 min.
10. Etch Al in Al-etch [Al-etch] until Al is almost completely cleared.
11. Blanket-expose photoresist with UV light.
12. Strip photoresist and complete the Al etching by soaking in MF-312.

Step Pattern

13. Expose the step pattern (which contains alignment marks) repetitively over the entire wafer (using e-beam).
14. Strip the Al by soaking in MF-312.
15. Develop the PMMA in MIBK:IPA (1:3) for 30 s (23°C).
16. Evaporate 50 nm of Cr, and liftoff in acetone.
17. RIE step pattern into the wafer [Face, 1987].
18. Strip the Cr by soaking in Cr-etchant.

Contact Pads

19. Spin PMMA, 6% in chlorobenzene, 950K MW, at 4000 rpm for 1 min.
20. Bake at 180°C for 30 min.
21. Align the pad mask to the step patterns, using the large alignment marks exposed with the step pattern.
22. Expose the PMMA in DUV light using the pad mask.
23. Develop in MIBK:IPA (1:3) for 30 sec (23°C).

Junction Patterning With E-beam

24. Align the junction pattern, using the marks ("T"s) exposed with the steps.
25. Expose junction pattern with e-beam.
26. Develop in MIBK:IPA (1:3) for 30 s (23°C).
27. Evaporate base electrode at an angle.
28. Oxidize base electrode.
29. Change angle, and evaporate counterelectrode.
30. Liftoff in acetone.

III. Electron Transport Theory

A. Localization and Dimensionality of Narrow Wires

III.A.1. General Considerations

For narrow wires there are a number of corrections to the classical Drude resistance $\sigma_o = 1/\rho_o = ne^2\tau/m$ (τ is the elastic scattering time, n is the electron density per unit volume, m is the electron mass, σ_o is the Drude conductivity, and ρ_o is the Drude resistivity): (1) localization effects, (2) Maki-Thompson superconducting fluctuations, (3) Aslamazov-Larkin superconducting fluctuations, (4) normal-state fluctuation effects, and (5) classical magnetoresistance. Since this brief account of localization in wires is presented as a preface to quantum interference in rings, we will refer the reader to [Bergmann, 1984] for a discussion of Aslamazov-Larkin fluctuations, and to [Santhanam et al., 1987] for a thorough account of the other corrections.

Consider a wire (Fig. III-1a) through which electrons diffuse. There are many possible interference paths, and one would expect that the net effect on the resistance R of all these paths would average to zero. However, there is a special case in which the correction to R from each path has the same sign - regardless of the specific scattering path. An input wave from the left (Fig. III-1b) can split into two partial waves which travel on identical, but *time reversed* paths. The paths are identical, and so the partial waves suffer identical, but time reversed scattering sequences, and thus return to the origin in phase with each other. If the path length is less than ℓ_ϕ then the two waves will remain phase-coherent, and each will

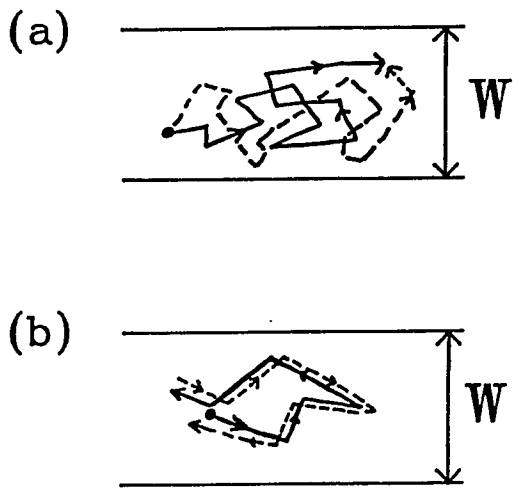

Fig. III-1: (a) Electrons diffusing through a wire, following random paths and interfering in a sample-specific way. (b) An electron wave splits into two partial waves which follow time-reversed paths. Initial wavevector is $\vec{k}$, final wavevector is $-\vec{k}+\vec{q}$. The largest contribution to the back-current occurs for values of q near zero.

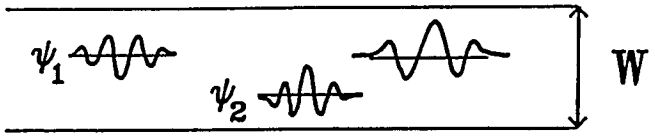

Fig III-2: Thouless picture of localization; wave-packets in the wire are strongly localized. Electron conduction in this regime occurs between weakly overlapping wave-functions, by thermal exitation, or by tunneling.

have a final momentum $-\vec{k}+\vec{q}$ (where $\vec{k}$ is the initial momentum, and $q<<k$) [Bergmann, 1984]. At the origin the waves interfere constructively, causing a "back-current" to flow to the left -- thereby increasing the resistance. The largest contribution to the back-current occurs for values of q near zero. If the path length is much greater than ℓ_ϕ (i.e., if one or both of the electron partial waves is likely lose its phase memory along the path) then the interference effects at the origin will average to zero.

The back-current arises from the electron's increased probability of returning to the origin - the electron is partially "stuck" (hence the term "localization"). At very low temperatures the electron can become strongly localized, and in this case the electron states can be considered as stationary wave packets in the wire. Electron conduction in this regime (Fig. III-2) occurs between weakly overlapping wave-functions, by thermal excitation or by tunneling. The first predictions of an increased R at low temperatures for wires of finite width were made by Thouless [1977], who used this picture of localized wave packets.

Localization has the effect of increasing the resistance at low temperatures (barring effects due to superconductivity and spin-orbit scattering). In addition, localization causes a change in the magnetic field dependence of the resistance. Application of a magnetic field perpendicular to the wire (or film) will destroy some of the time-reversal symmetry necessary for the phase coherence, thereby *decreasing* the resistance. In practice the magnetoresistance R(H) is a cleaner measure of localization than the temperature dependence of R, since the temperature dependence R(T) can be dominated by other effects, such as superconducting fluctuations and electron-electron interaction effects.

III.A.2. Spin-Orbit Scattering

In the frame of a conduction electron, an impurity nucleus appears as a moving charge. This moving charge creates a magnetic field at the electron. The correction to the electron's motion due to this field is called the spin-orbit (SO) interaction, in analogy to the case when the electron is bound to the nucleus [cf., Bethe and Salpeter, 1977]. The spin-orbit Hamiltonian is [Altshuler and Aronov, 1985]

$$H_{so} = -i\epsilon\, \vec{\sigma} \cdot (\vec{k} \times \vec{k}') \qquad \text{(III-1)}$$

where $\vec{k}$ is the wavevector before the interaction (collision), $\vec{k}'$ is the wavevector after the interaction, and ϵ is a constant. H_{so} does not violate the time-reversal symmetry of impurity scattering events. However, spin-orbit coupling will change the symmetry properties for the time-reversed paths discussed in the previous section. The spinor group for half-integral spins [Bethe, 1929] has a periodicity of 4π in $\vec{k}$-space; that is, a rotation by 2π in $\vec{k}$-space (Fig. III-3a) *reverses* the sign of the wavefunction. The time-reversed paths therefore will interfere destructively, and the application of a magnetic field will thus tend to *increase* the resistance (Fig. III-3b). In the case of strong spin-orbit scattering this tendency will dominate the localization contribution, leading to so-called "antilocalization" [Bergmann, 1984].

For a metal with spin-orbit scattering (and no magnetic scattering) there is a new length scale, ℓ_2 ($\neq \ell_\phi$) for deciding the effective dimension for part of the localization contribution to R:

(a)

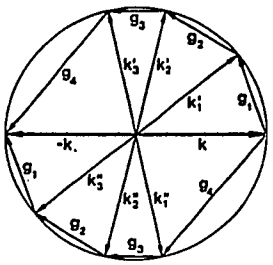

(b)

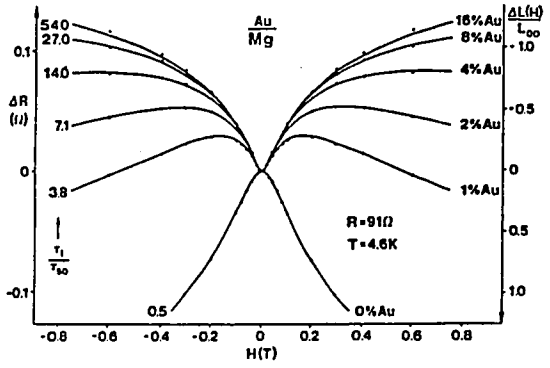

Fig. III-3: (a) $\vec{k}$-space picture of an electron wave which splits into two partial waves. The scattering sequences are related by time-reversal, and so the amplitudes in the final state $-\vec{k}$ are identical. For the case of no spin-orbit scattering this leads to constructive interference. (b) Effect of spin-orbit scattering. An overlayer of Au on a Mg film changes the behavior completely. Solid lines are fits to the theory of Hikami et al. [1980]. From [Bergmann, 1984].

$$\ell_2 = (D\tau_2)^{1/2}$$

where $\tau_2^{-1} = \tau_\phi^{-1} + (4/3)\tau_{SO}^{-1}$ (III-2)

and τ_{so}^{-1} is the spin-orbit scattering rate.

III.A.3. Superconducting Fluctuation Effects

For the experiments on aluminum we must consider superconducting effects. Aslamazov-Larkin fluctuations [Bergmann, 1984] can be ignored as long as $(T/T_c) > 1.3$ [Santhanam et al., 1987]. The correction due to Maki-Thompson (MT) fluctuations [Larkin, 1980; Patton, 1971] will be the dominant term causing a decrease in the resistance as T approaches T_c.

The MT fluctuations arise from the correlation between the two quasiparticles of near-zero total momentum which are produced when a thermal excitation breaks a superconducting pair. Time-reversal symmetry is required to maintain this correlation. Thus, application of a magnetic field will "destroy" the MT contribution. The resistance thus increases with application of a magnetic field. The result is that the magnetoresistance at low fields becomes positive instead of negative. Note that the MT correction is <u>not</u> effected by SO scattering since the SO hamiltonian does not violate time reversal symmetry. It follows that ℓ_ϕ is the appropriate length scale for deciding the dimensionality of the MT correction.

III.A.4 Magnetic Scattering. The 1D Localization Equation

Magnetic impurities which flip the electron's spin will destroy both the localization and MT contributions. For the Al used in these studies the magnetic

scattering is negligible since common magnetic impurities do not have localized moments in Al [Ashcroft and Mermin, 1976]. However, Ag has shown some evidence of magnetic scattering, and the localization expressions [Bergmann, 1984; Lee and Ramakrishnan, 1985] can be generalized by substituting

$$(\tau_\phi^{-1} + 2\tau_s^{-1}) \text{ for } \tau_\phi^{-1}$$

and

$$[\tau_\phi^{-1} + (4/3)\tau_{so}^{-1} + (2/3)\tau_s^{-1}] \text{ for } \tau_2^{-1}$$

in eq. III-2 (this will be done for eq. III-3 below). In terms of length scales we can substitute $\ell_\phi = (D\tau_\phi)^{1/2}$, $\ell_2 = (D\tau_2)^{1/2}$, and so on.

The formula for 1D localization including MT fluctuations, SO and magnetic scattering [Wind et al. 1986] is

$$\frac{\Delta R}{R} = \left[\frac{R_\square}{\pi(\hbar/e^2)W} \right] \left\{ \frac{3}{2} [\ell_2^{-2} + \ell_H^{-2}]^{-1/2} - (\beta+1/2)[\ell_1^{-2} + \ell_H^{-2}]^{-1/2} \right\} \qquad \text{(III-3)}$$

where W=line width,

$$\ell_2^{-2} = \ell_\phi^{-2} + (4/3)\ell_{so}^{-2} + (2/3)\ell_s^{-2},$$

$$\ell_1^{-2} = \ell_\phi^{-2} + 2\ell_s^{-2},$$

$$\ell_{so} = (D\tau_{so})^{1/2}, \quad \ell_s = (D\tau_s)^{1/2},$$

$$\ell_H = \frac{\sqrt{3}\hbar}{eBW},$$

and $\beta(T/T_c)$ is the MT superconducting fluctuation parameter. $\beta = 0$ for Ag. Linewidths used in the studies described here are in the "fully one-dimensional"

regime; that is, $W < \ell_2$, $W < \ell_1$, $W < \ell_T$ (thermal diffusion length*), and $W < \ell_\phi = (D\tau_\phi)^{1/2}$. The temperature dependence and dimensionality of various scattering mechanisms are summarized in Table III-1.

III.B. Electron-Electron Scattering in Sub-0.1 μm Wires

III.B.1 General Considerations

Several mechanisms contribute to the phase-breaking rate $\tau_\phi^{-1} = D/\ell_\phi^2$. Experiments on two-dimensional systems [Santhanam and Prober, 1984; Gordon et al., 1983; Gordon et al., 1984; Dynes, 1982; Lee and Ramakrishnan, 1985; Kramer et al., 1985] have shown that phase breaking is dominated by two-dimensional (2D) electron-electron (ee) scattering (typically for $T \lesssim 5K$), and by electron-phonon (ep) scattering at higher temperatures. Over the full temperature range, $\tau_\phi^{-1} = \tau_{ee}^{-1} + \tau_{ep}^{-1}$.

In previous studies of wider 1D wires [Santhanam et al., 1984; Gordon, 1984] the wires were in the 1D regime for localization effects: W was less than both ℓ_2 and ℓ_ϕ. However, the wires were too wide to be in the 1D limit with respect to the electron-electron scattering mechanism. The length scale which determines the dimensionality of electron-electron scattering is the thermal diffusion length $\ell_T = (\hbar D/k_B T)^{1/2} \sim 0.1$ μm for Al and Ag wires at low temperatures. Only wires with width and thickness less than ℓ_T are "one-dimensional" with respect to electron-electron scattering.

---

* This will be defined in the next section.

Table III-1

Temperature Dependence and Dimensionality
of the Resistance for Various Scattering Mechanisms

Scattering Mechanism	Dimensional[a] Length Scale of Scattering rate	Temperature Dependence 1D	2D	3D
clean-limit elec.-phonon	λ_{phonon} or ℓ (b)			T^3 (e)
electron-electron w/ $\Delta E \geq k_B T$	ℓ_T (c)	$T^{1/2}$ (c)	$T \ln(T_1/T)$ (d) or, T (c)	$T^{3/2}$ (c)
electron-electron w/ $\Delta E \ll k_B T$	ℓ_T (i)	$T^{2/3}$ (c)	T (c)	T^2 (c)
spin-orbit	ℓ_2 (g)	none	none	none
magnetic	ℓ_2 (g) ℓ_1 (h)	none (f)	none (f)	none (f)
classical clean-limit electron-electron	(j)	T^2 (j)	T^2 (j)	T^2 (j)

(a) If the thickness is less than this, then the sample is 2D. If both thickness and width are less than this, then the sample is 1D. For the phonon rate, the criteria are relevant if the phonons in the film are acoustically decoupled from the substrate phonons.
(b) Pippard-Ziman condition [Ziman, 1960; Pippard, 1955].
(c) Altshuler, Aronov, Khmelnitskii, and Larkin 1982c.
(d) Abrahams et al., 1981; Fukuyama and Abrahams, 1983.
(e) Lawrence and Meador, 1978; applies to "clean limit": $q_{ph}\ell << 1$.
(f) Applies to our samples at low temperatures. Samples with large amounts of magnetic impurities will show Kondo effects.
(g) Applies to the "triplet" term of eq. III-3 (the 3/2 term).
(h) Applies to the "singlet" term of eq. III-3 (the 1/2 term).
(i) Wind et al., 1986.
(j) Applies to "clean limit", $\hbar/\tau << k_B T$. See [Ashcroft and Mermin, 1976].

An additional motivation for the study of scattering mechanisms in 1D wires is the unresolved discrepancy between predictions of the 2D electron phase-breaking rate. The theory of Altshuler, Aronov, Khmelnitskii, and Larkin (AAK) [Altshuler et al., 1982b] predicts a 2D electron-electron phase-breaking rate which has a temperature dependence $\propto T$. The theory of [Abrahams, Anderson, Lee, Ramakrishnan, 1981] and [Fukuyama and Abrahams, 1983] predicts a dependence $\propto T \ln(T_1/T)$. Although quite different in form, the magnitudes predicted by these theories are too similar to be clearly distinguished with the experimental data of 2D metal films.

An electron-electron scattering event with a large energy transfer ($\Delta E \sim k_B T$) certainly destroys the electron phase memory and contributes to the phase-breaking rate. A change in energy causes a change in the phase of the electron's wavefunction, as can be seen from eq. I-1. Altshuler and co-workers [1982b,c] have predicted another contribution to τ_ϕ^{-1}, from multiple electron-electron collisions with *small* energy transfers ($\Delta E << k_B T$). Each small energy change will alter the phase randomly, and a series of small energy changes will cause the electron's phase to evolve as a "random walk" -- which after many steps leads to a net phase change comparable to π.

Electron-electron collisions are enhanced in the presence of impurities, due to the violation of momentum conservation [Altshuler and Aronov, 1981a]. This "quasielastic" rate is equivalent to the Nyquist rate $\tau_N^{-1}=(D/\ell_N^2)$, due to the scattering of electrons by electromagnetic fluctuations. The spectral power of these fluctuations is roughly constant with frequency [Eiler, 1984]; that is, $N(\omega)\hbar\omega =$

constant, where $N(\omega)$ is the number density of photons. Low frequency fluctuations are inefficient in scattering. Dephasing occurs due to many scattering events with small energy transfers.

The relevant dimensional length scale for the Nyquist scattering rate has not been clearly defined in the papers by AAK [1982b] and Altshuler and Aronov [1985]. However, recent experimental results suggest that only wires with width less than ℓ_T can be considered one-dimensional with respect to the Nyquist mechanism [Wind et al., 1986]. These results will be discussed further in the next chapter.

For sub-0.1 μm Al and Ag wires the Nyquist electron-electron rate is the dominant inelastic mechanism below ~10K. Experiments at Yale [Wind et al., 1986] have confirmed the theoretical predictions for the width dependence, temperature dependence, and magnitude of the 1D electron-electron "Nyquist rate" [AAK, 1982]:

$$\tau_{ee}^{-1} = \left[\frac{R_\square}{\sqrt{2}(\hbar/e^2)} \frac{k_B}{\hbar} \frac{\sqrt{D}}{w} \right]^{2/3} T^{2/3} \qquad \text{(III-4)}$$

III.B.2 The Thermal Diffusion Length, ℓ_T

When seeking a physical interpretation of the thermal diffusion length ℓ_T it is best to consider first its formal origin. The electron-electron interaction is determined by the phase volume of available states in the scattering process. Using Fermi's Golden Rule it can be shown that [AAK, 1982, their equ. 3.4.3]

$$\tau_{ee}^{-1} \sim \int_0^E d\omega \int_0^\omega dE' \int_0^\infty q^2 dq \; W_q \left[\mathrm{Re}\left(\frac{1}{i\omega + Dq^2} \right) \right]^2 \qquad \text{(III-5)}$$

where $\hbar\omega$ = the energy transfer in a collision,

E' = the energy of the second quasiparticle in the collision,

W_q = square of matrix element of the interaction, and

q = momentum transfer in the collision.

As one dimension of the metal (say, the width W) is reduced, the integral approximation over a quasi-continuum of q-states must be replaced by a sum over the discrete states $q = \pi n/W$, where n is an integer. We see from eq. III-5 that the essential q's are on the order of $(\omega/D)^{1/2}$; or, using the lowest n, we have $W \sim (D/\omega)^{1/2}$. In terms of an energy $\varepsilon \equiv \hbar\omega$, this reads

$$\varepsilon \sim \hbar D/W^2 \, . \qquad \text{(III-6)}$$

These states can be considered discrete as long as the energy spacing is greater than $k_B T$. The dimensional crossover is thus found when we set $\varepsilon = k_B T$:

$$k_B T \sim \hbar D/W^2$$

$$W \sim (\hbar D/k_B T)^{1/2} \equiv \ell_T \qquad \text{(III-7)}$$

Consider now a different derivation of eq. III-7**. We ask: if two electrons are initially in phase, but differ in energy by k_BT, how far can they diffuse before their relative phase differs by 2π? Fig. III-4 shows a diffusing electron. L is the net displacement, s is the path length. The phase increment along the path is $2\pi s/\lambda(E) = sk(E)$. When does $[sk(E) - sk(E+k_BT)] = s\Delta k = 2\pi$? If $s\Delta k=2\pi$ then $1/s \sim (\Delta k/\Delta E)\Delta E$. Using $v_Ft=s$ (t is the time interval) and $L=(Dt)^{1/2}$ we have $s = v_FL^2/D$.

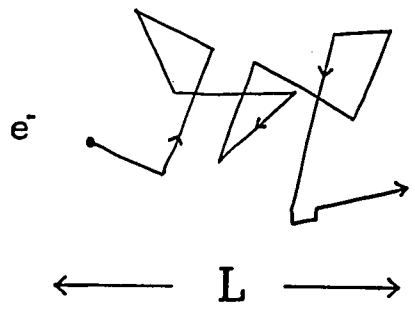

Fig. III-4: A diffusing electron. L is the net displacement, s is the path length. The electron undergoes a series of elastic scattering events.

** Following [Stone and Imry, 1986] and Stone, private communication

So,

$$\frac{\Delta k}{\Delta E}\,\Delta E \sim \frac{D}{v_F L^2}$$

or,

$$\hbar v_F \Delta E \sim \frac{D}{v_F L^2} \quad .$$

Setting $\Delta E = k_B T$ gives $L = (\hbar D/k_B T)^{1/2} = \ell_T$.

Instead of asking for an L beyond which the electrons go out of phase, we could have said, "given a sample of length L, what energy change E_c is necessary so that two electrons which follow the same path of length s across the sample acquire a significant phase difference?" The time to diffuse across the sample is L^2/D (as mentioned above), and the Uncertainty Relation gives

$$E_c \sim hD/L^2 \qquad \text{(III-8)}$$

which is the same as eq. III-6. This E_c is the same as the "Thouless parameter", V, which measures the sensitivity of the energy levels to boundary conditions (e.g., the phase difference across a system) [Stone and Imry, 1986].

We see that the ℓ_T's (or equivalently, the E_c's) from these two approaches are equivalent. An initially coherent electron wavepacket is made from a thermal energy distribution. These arguments imply that ℓ_T is the length over which the phase coherence of the wavepacket is lost due to thermal smearing. However, it is important to note that this thermal smearing is *not* equivalent to dephasing in an inelastic collision. If two electron waves (or, two partial waves) of the *same* energy

are initially phase coherent, then it is the phase-breaking length ℓ_ϕ which is the distance over which these waves lose coherence due to energy-changing collisions. Thus, for time-reversed paths, ℓ_ϕ is the relevant length scale, not ℓ_T.

III.C. Rings and the Aharonov-Bohm Effect

III.C.1. Introduction

Interference patterns of electrons (Fig. III-5a) traveling through vacuum were first predicted by Aharonov and Bohm in 1959 [Aharonov, Bohm, 1959], and were seen experimentally the following year by Chambers [Chambers, 1960]. The important difference between this and more recent experiments is that in disordered systems (such as a metal) the electrons are subject to many scattering events. It is not remarkable (in 1987) that electron waves interfere or that they interact with a vector potential; rather, it is surprising that this interference can be clearly observed in a disordered system.

The paths shown in Fig. III-1b are suggestive of the more complex geometry of a ring. When the time-reversed paths of Fig. III-1b are indeed constrained to a ring (Fig. III-5b), the partial waves continue to interfere constructively at the origin. Just as in the case of localization in a wire, the resistance is increased. In the case of a ring, however, the effect of a magnetic field is more dramatic. The magnetic field $\vec{B} = \vec{\nabla} \times \vec{A}$ will shift the phase of the electron's wavefunction by

$$\Delta\phi = \frac{e}{\hbar} \int \vec{A} \cdot d\vec{l} \qquad \text{(III-9)}$$

where the integral is taken along the electron's path.

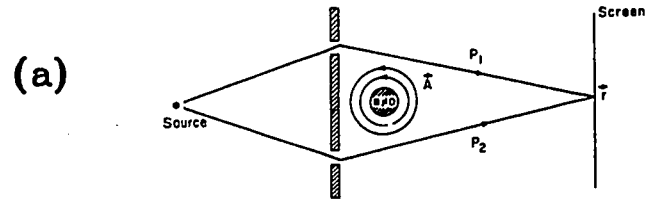

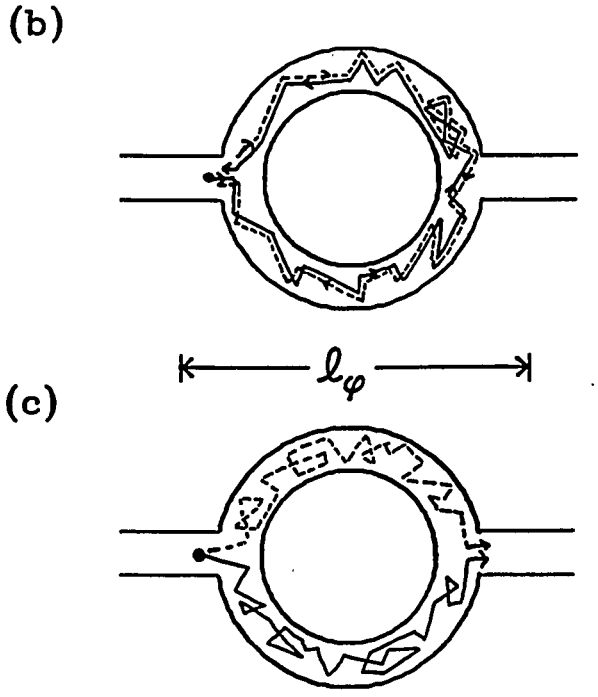

Fig. III-5: (a) The Aharonov-Bohm effect in vacuum. Electrons diffract in the same way as light, except that the phase is shifted by the vector potential $\vec{A}$. From [Shankar, 1980]. (b) The time-reversed paths of Fig. III-1b are constrained to a ring. A magnetic flux normal to the page shifts the phase of the electron's wavefunction. The magnetoresistance (MR), R(H), will oscillate with a flux period of h/2e. (c) Arbitrary-path (i.e., non-time-reversed) interference shown for the case where the MR will oscillate with a flux period of h/e.

An electron wave traveling clockwise fully around the ring has its phase shifted by

$$\Delta\phi = \frac{e}{\hbar} \oint \vec{A}\cdot d\vec{l} = 2\pi\Phi/\Phi_o \qquad \text{(III-10)}$$

where $\Phi_o = h/e$ is the single-electron flux quantum. The phase difference between two waves, one propagating fully clockwise and the other propagating fully counterclockwise, is then $4\pi\Phi/\Phi_o$. Because of this shift, the maximum back-current will occur when $\Delta\phi_{cw} - \Delta\phi_{ccw} = \Delta\phi = 2\pi n$, where n is an integer. The resistance of the ring should therefore oscillate with a period in the flux of

$$\Delta\Phi = \Phi_o/2 = h/2e = 20.7 \text{ gauss } \mu m^2.$$

A single wire will not show this oscillatory effect, because there are many different paths, each of which enclose different areas, and thus enclose different amounts of flux. A ring constrains the electrons to enclose a fairly well defined area, which determines a well-defined flux period. Of course, the magnetic field penetrates also the metal of the ring, thereby decreasing the localization effect (i.e., the time-reversed-path interference not encircling the ring) as it does in wires. Oscillations in the resistance thus appear on a background due to 1D localization. The ring must be designed with a sufficiently small ratio of linewidth to diameter, so that at least a few oscillations can be seen before localization is destroyed by the magnetic field.

Time-reversed paths are of course not the only route by which electrons can interfere. For a wire which is not much longer than ℓ_ϕ, the paths shown in Fig. III-1a can produce a net (albeit random) time-independent interference pattern. The net intensity from all possible paths will depend on the microscopic impurity distribution of the metal [Lee and Stone, 1985; Stone, 1985].

For the paths shown in Fig. III-5c, the ring geometry once again provides a "monochromator" for the different interference patterns. In this case the two paths around the ring are non-equivalent, so that the phase difference is random. Another set of paths will have a <u>different</u> phase difference and, as in the case of a short wire, the net intensity from all possible paths will depend on the microscopic impurity distribution. The distinction between a short wire and a small ring is that the ring encloses a well-defined flux. For this case each electron travels <u>half</u>-way around the ring, so that <u>twice</u> the flux is needed to change the phase by 2π. Therefore, the resistance should oscillate with a flux period of $\Phi_o = h/e$, although the oscillation phase will depend upon the specific impurity distribution in the ring.

There are <u>two</u> mechanisms which produce oscillations of period $\Delta\Phi = h/2e$: (1) those due to time-reversed paths, as predicted by Altshuler, Aronov, and Spivac ("AAS") [Altshuler, Aronov, Spivac, 1981], and (2) those due to the first harmonic of arbitrary, non-time-reversed paths which fully encircle the ring ("non-AAS").

The above arguments suggest that there should be higher-harmonic effects (with flux periods h/ne where n is an integer) due to electron paths which revolve further about the ring. If for a ring of radius r we have $n\pi r > \ell_\phi$, then harmonics of order h/ne are expected to be damped by a factor of $\exp(-n\pi r/\ell_\phi)$, if $\ell_\phi < \pi r$.

III.C.2. Theories of Oscillations in Rings

III.C.2.i. Diagrammatic Results

Corrections to the Drude formula for the conductance can be calculated via diagrammatic perturbation techniques. These "Kubo Formalism" methods have been described in detail elsewhere [AAK, 1982; Bergmann, 1984; Lee and Ramakrishnan, 1985; Fukuyama, 1983]. The first corrections using this technique [Langer and Neal, 1966] considered the contribution to the conductivity due to time-reversed paths (or, "maximally-crossed" diagrams). This eventually led to a description of localization in wires [Altshuler, Aronov, 1981b; Santhanam et al., 1984].

Localization theory led also to the first predictions of resistance oscillations in metal rings [Altshuler, Aronov, and Spivac, 1981 (AAS); Altshuler, Aronov, Spivac, Sharvin, and Sharvin, 1982]. This theory predicts that the low-temperature resistance will be a periodic function of the flux through the ring, with a period h/2e. For a ring where $2\pi r > \ell_\phi$, the AAS theory gives

$$\frac{\Delta R}{R} = -(\beta+1/2)(\ell_1^{-2}+\ell_H^{-2})^{-1/2}\,\frac{R_\square}{\pi W(\hbar/e^2)}\left[1+\cos\left(\frac{2\pi\Phi}{h/2e}\right)\exp\left(\frac{-2\pi r}{(\ell_1^{-2}+\ell_H^{-2})^{-1/2}}\right)\right]$$

$$+\ \frac{3}{2}(\ell_2^{-2}+\ell_H^{-2})^{-1/2}\,\frac{R_\square}{\pi W(\hbar/e^2)}\left[1+\cos\left(\frac{2\pi\Phi}{h/2e}\right)\exp\left(\frac{-2\pi r}{(\ell_2^{-2}+\ell_H^{-2})^{-1/2}}\right)\right] \qquad \text{(III-11)}$$

where Φ is the magnetic flux through the ring, and the other symbols are defined in eq. III-3.

The points of interest in this equation are (1) the periodicity of h/2e in the flux, (2) the exponential decrease with radius divided by (3) a field-dependent length scale determined by the phase-breaking length ℓ_ϕ, the magnetic scattering length ℓ_s, the spin-orbit length ℓ_{SO}, and the magnetic field***.

Eq. III-11 reduces to the 1D wire result (eq. III-3) when $2\pi r >> \ell_\phi$. The oscillatory part of eq. III-11 can be rewritten as [Chandrasekhar et al., 1985]

$$\frac{\Delta R}{R} = -(\beta+1/2)\frac{0.98}{N}\frac{(\ell_1^{-2}+\ell_H^{-2})^{-1/2}}{\ell}\frac{R_\square}{\pi W(\hbar/e^2)}\left[\cos\left(\frac{2\pi\Phi}{h/2e}\right)\exp\left(\frac{-2\pi r}{(\ell_1^{-2}+\ell_H^{-2})^{-1/2}}\right)\right] \qquad \text{(III-12)}$$

where ℓ is the elastic mean free path, $\ell_{SO} << \ell_\phi$, and N is (approximately) the number of atoms in the wire cross-section. The number of transverse states across the wire (below E_F) is on the order of $k_F^2 A$, where k_F is the Fermi wavevector and A is the cross-sectional area. We see that $k_F^2 A \sim N$.

*** One may find in the literature [Chandrasekhar et al., 1985] "effective ℓ_ϕ's", where ℓ_ϕ is a field-dependent quantity. This thesis takes ℓ_ϕ to be field independent, and uses instead ℓ_H as the field-dependent quantity. In this way we retain continuity between localization and the Landauer-type theories where, as we will see later, ℓ_ϕ is not field-dependent.

Eq. III-11 shows that oscillations predicted by the AAS theory appear on a background due to 1D localization effects (as discussed in section III.A). The overall dependence on magnetic field, magnetic scattering, and spin-orbit scattering will be the same as in wires. Spin-orbit scattering and MT superconducting fluctuations will tend to invert the initial phase of the AAS oscillation, just as they change the sign of the magnetoresistance in wires.

III.C.2.ii. Landauer Formalism

The Landauer formalism models a ring as a set of scattering centers connected by ideal channels, as shown in Fig. III-6b. Each scattering center is a potential barrier with transmission coefficient T and reflection coefficient R. For a barrier in a single channel (Fig. III-6a), the conductance is given by [Landauer, 1957, 1970]

$$G = \frac{e^2}{\pi\hbar} \frac{T}{R} . \qquad \text{(III-13)}$$

This is the single-channel Landauer formula. Subtleties involved in defining the chemical potential across the barrier will be discussed later. A 1D wire of finite length may be modeled as a series of N such barriers. In general the resistance of two such resistors in series is greater than the sum of their individual resistances.

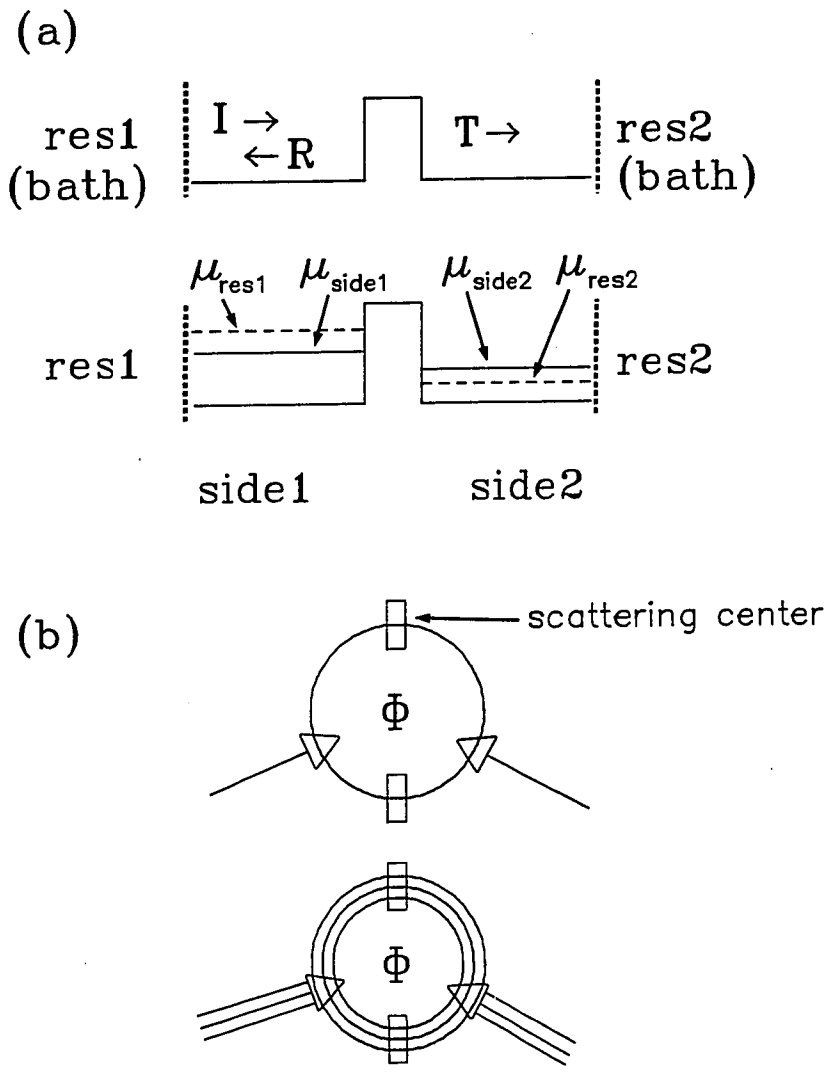

Fig III-6: (a) The Landauer geometry: μ_{res1} and μ_{res2} are the chemical potentials of the baths; μ_{side1} and μ_{side2} are those of the ideal conductors. (b) 1D ring model (above); ideal wires link two scattering centers. Multichannel ring (below) with three channels. A flux Φ is applied through the ring. From [Imry, 1986].

To simulate a wire of finite width we consider the "multichannel" case (Fig. III-6]. Several formulas have been proposed for the multichannel Landauer equation [Büttiker et al., 1985; Fisher and Lee, 1981; Langreth and Abrahams, 1981]; for example [Stone and Imry, 1986]

$$g=2\ \mathrm{Tr}(t^{\dagger}t) \qquad \text{(III-14)}$$

is the conductance in units of (e^2/h). t is the transmission matrix, where $|t_{ij}|^2$ is the transmission coefficient for transfer from the j^{th} channel to the i^{th} channel.

The case of two ideal parallel barriers in a ring with leads was first solved by Gefen, Imry, and Azbel [1984], who found oscillations in the transmission coefficient as a function of Φ. The dominant period was found to be h/e. Predictions for a more realistic ring were later presented by Büttiker [Büttiker et al., 1985]. The most recent result [Stone and Imry, 1986] (where T=0 and $\ell_\phi > 2\pi r$) for the normalized conductance ($g=G(h/e^2)$) as a function of energy and field can be expressed schematically as follows:

$$g(E,B)=g_b(E)+g_o(E,B)+\sum_{n=1}^{\infty} g_n(E,B)\cos[2\pi n(\Phi_h/\Phi_o)+\gamma_n(E,B)] \qquad \text{(III-15)}$$

where Φ_h is the flux through the hole, $\Phi_o=h/e$, and g_b is the background Ohmic conductance. The g_n's and γ_n's reflect the *microscopic* impurity distribution. When averaging over many samples, $\langle g_o\rangle=0$, and $\langle g_1\rangle=0$, but $\langle g_2\rangle\neq 0$.

To generalize eq. III-15 to finite temperatures, one considers the effect of averaging over a distribution of energies with a spread $\Delta E=k_BT$ [Stone and Imry, 1986]. The energy scale E_c defined in section III.B.2 (eq. III-7 and III-9) is the characteristic energy scale such that electrons with energies differing by E_c will have significant differences in the interference along the length of a system. Averaging over an effective number $N=(k_BT/E_c)$ interference patterns will reduce the relative oscillation amplitude by $(E_c/k_BT)^{1/2}\sim L/\ell_T$, where L is the length of the system, and $\ell_T=(\hbar D/k_BT)^{1/2}$. Generalization to the case where $\ell_\phi << n\pi r$ will require a factor of $\exp(-n\pi r/\ell_\phi)$. For the case where $\ell_\phi \lesssim n\pi r$, the corrections do not appear to have a simple analytical form [Stone, 1987].

The component of eq. III-15 with period $\Phi_o=h/e$ is found from numerical simulations to be

$$\Delta G \sim 0.4(e^2/h)\cos[(2\pi\Phi/\Phi_o)+\gamma_1]. \qquad \text{(III-16)}$$

The magnetic flux penetrating the metal (annulus) of the ring will have an effect on the magnetoresistance; however, unlike the localization effect these non-AAS oscillations will not be <u>damped</u> by the field. The magnetic field *does* alter the phase of the electrons, but the non-AAS oscillations *already* have an arbitrary phase γ. A magnetic field in the annulus simply causes a beating between the oscillations with frequency $\Delta B=\Phi_o/$(hole area) and the aperiodic oscillations whose frequency *scale* is $\Delta B\sim\Phi_o/$(annulus area) (see Fig. III-7). In the AAS case the magnetic field in the annulus destroys the special phase relationship necessary for time-reversed scattering.

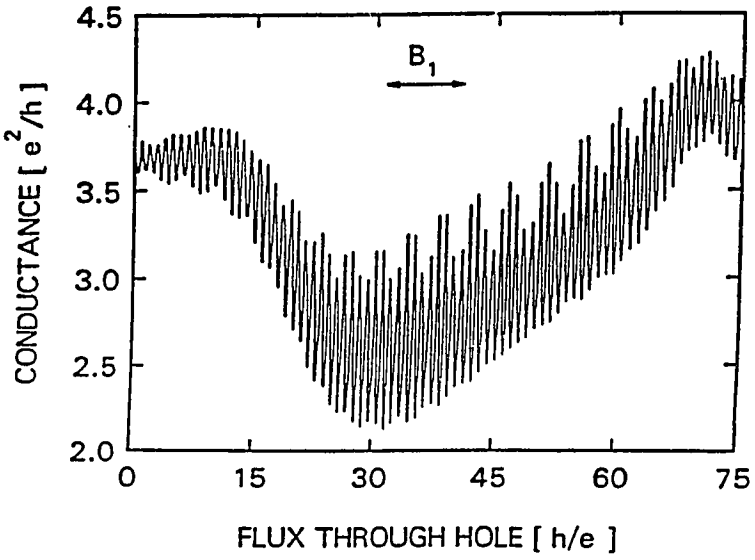

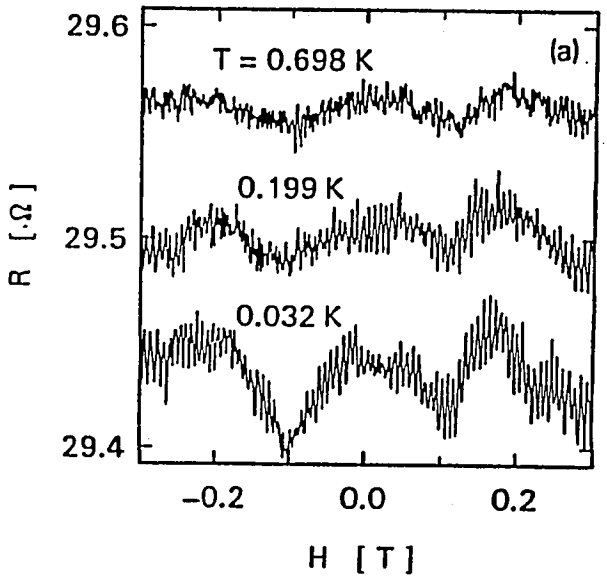

Fig. III-7: Top: Numerical simulation of magnetoconductance of a 100×100 site ring. h/e oscillations are seen. B_1 is the predicted scale of aperiodic background. From [Stone and Imry, 1986]. Bottom: magnetoresistance of a Au ring, showing a similar aperiodic background. From [Webb et al., 1985].

For an array of rings which extends over a distance larger than ℓ_ϕ, the non-AAS oscillations would be smaller than for a single ring. In contrast, the AAS effect has the same magnitude in an array of rings, since $\gamma_1=0$ for all time-reversed paths. The amplitude of resistance oscillations with period h/e decreases as $N^{-1/2}$, where N is the number of rings. A cylinder is roughly equivalent to an array of rings. A long cylinder ($N>>1$) is therefore expected not to show the non-AAS oscillations. The resistance of a long cylinder is expected to show only the AAS (localization) oscillations with period h/2e.

III.C.3. The Problem of Contacts

There are a number of ways that resistance can be defined. The early theoretical work on rings [Büttiker et al., 1983] considered simple 1D rings without contacts. The resistance could presumably be determined by measuring electromagnetic absorption. For the barrier in Fig. III-6 one can define the conductance as [Büttiker et al., 1986]

$$G_c = \frac{I}{\mu_{res1} - \mu_{res2}} = \frac{e^2}{\pi\hbar} T \qquad \text{(III-17)}$$

in contrast to

$$G = \frac{I}{\mu_{side1} - \mu_{side2}} = \frac{e^2}{\pi\hbar} \frac{T}{R}$$

where the μ's are chemical potentials defined in Fig. III-6. G_c is the conductance more likely to be measured; however, the contact between reservoir and ideal wire will introduce a contact resistance [Sharvin, 1965] $R_{orifice}=4\rho\ell/3A$, where ρ is the

resistivity, ℓ is the mean free path, and A is the cross-sectional area of the orifice.

In reality resistance measurements are made with a four-terminal configuration. Büttiker [1986] has recently derived a four-terminal multichannel Landauer formula which not only accounts for separate voltage probes, but also seems to explain the asymmetries seen in magnetoresistance data [Webb et al., 1985; Washburn et al., 1985]. Recent experiments [Skocpol et al., 1987; Webb et al., 1987] on systems with probe spacings less than ℓ_ϕ demonstrate the large influence of the voltage probes on any measurement in this size regime.

To summarize the theoretical considerations of rings: we have seen that the resistance should oscillate with periods h/e and h/2e (with higher harmonics heavily damped). The special case where electron partial waves follow time-reversed paths allows h/2e oscillations to be seen even in cylinders and large ensembles of rings.

III.D. Normal-State Two-Junction Interference Device ("normal-QUID")

III.D.1. The Normal-QUID Idea

Experiments which detect Aharonov-Bohm oscillations in single rings have measured amplitudes of $\Delta R/R$ which are on the order of 10^{-4} [Chandrasekhar et al., 1985] and 10^{-3} [Webb et al., 1985]. Such small amplitudes result from the ring's finite temperature, finite linewidth, and from a circumference which may be larger than ℓ_ϕ. These limitations are seen clearly in the oscillatory part of the AAS prediction, eq. III-12. The common factor between eq. III-12 and eq. III-16 is h/e^2 = 26 kΩ. In the measurement of a common 100 Ω ring this gives an overall factor of

$\Delta G/G = 100/26000 = 4 \times 10^{-3}$.

If the resistance of the ring could be increased without degrading ℓ_ϕ, then the oscillations could be greatly enhanced. Fig. III-8a shows a schematic of a so-called "normal QUID" (N-QUID). A high resistance can be provided by two tunnel junctions between the normal-metal leads. The dimensions of the high-resistance region must be smaller than the ℓ_ϕ for that region. (We do not at this time know what determines ℓ_ϕ for the high resistance region.) The tunneling process will cause a high resistance, while (hopefully) maintaining phase coherence. In appearance the device is much like a classic DC SQUID [cf. Wolf, 1985].

This N-QUID device is intended to mimic the single-barrier picture used with the Landauer formalism. Using clean metal and high-resistance junctions allows the exploration of the high-resistance regime of the quantum interference theory. Experiments at Yale with N-QUIDs have not yet yielded definitive data; however, their development has provided a useful technique for the fabrication of tunnel junctions with electron-beam lithography.

III.D.2 Tunneling Barriers

It may be argued that a tunneling barrier is not a simple enough system to provide an unambiguous test of the high-resistance regime of the ring theories. Clearly, a ring with "kinks" (Fig. III-8b) might be more suitable; however, such a device would be very difficult to fabricate. The first objection regarding tunnel barriers is that the tunneling oxide may not be uniform. Consider the barrier depicted in Fig. III-9. A wave $\psi_1 = \alpha_1 e^{ik_1 x}$ is attenuated by the barrier, and produces

(a)

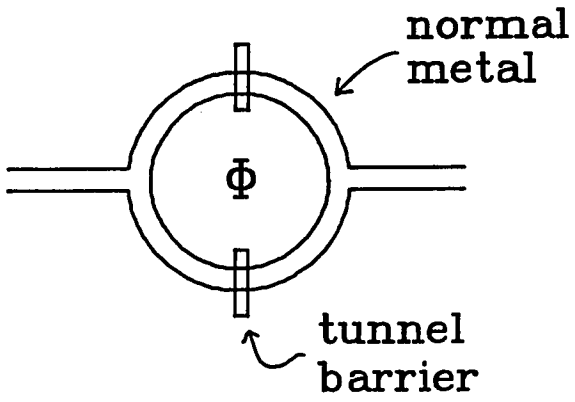

(b)

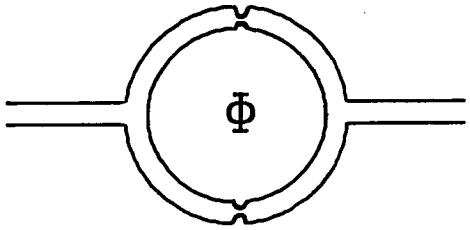

Fig. III-8: (a) The normal-QUID structure. The size of the ring must be less than the ℓ_ϕ for the normal metal, and the tunnel barrier must be smaller than its own effective phase-breaking length. (b) A ring with kinks is another possible system for investigation of the high-resistance regime.

$\psi_3=\alpha_3 e^{ik_3 x}$ on the right-hand side. For such a simple barrier an exact solution to the Schrödinger equation can be found by requiring that ψ and $d\psi/dx$ be continuous. In the case where the potential drop across the junction is much less than k_BT, we can say that $k_1=k_3=k$, and the result is [Baym, 1969; Wolf, 1985]

$$\psi_3 = \frac{2ik\kappa}{(k^2-\kappa^2)\sinh(\kappa d)+(2ik\kappa)\cosh(\kappa d)}\, e^{ik(x+d)} \qquad \text{(III-18)}$$

where d is the barrier thickness, $\kappa=\{(2m/\hbar^2)[V-E]\}^{1/2}$, and (V-E) is the barrier height. After some algebra one finds that the phase shift across the barrier is

$$\Delta\phi = \tan^{-1}\left[\frac{2(k^2-\kappa^2)\tanh(\kappa d)+(4k\kappa)\tan(2kd)}{4k\kappa-2(k^2-\kappa^2)\tanh(\kappa d)\tan(2kd)}\right] \qquad \text{(III-19)}$$

Consider the effect of the barrier on the thermal diffusion length. When we assume some reasonable values; say, for aluminum $E_F=11.7$ eV, $V=12.7$ eV, $d=20$ Å, and $T=1$ K [Ruggiero et al., 1986], then we find that the phase shift across the barrier is <u>smeared</u> 3×10^{-4} radians by the thermal spread k_BT. If the barrier were not there, then the phase would be broadened 1×10^{-4} radians -- assuming roughly ballistic transport over 20 Å. We see that in either case the junction region has little effect on thermal smearing, since the thermal diffusion length is determined by the distance over which the electron's phase is broadened by $\sim 2\pi$ (see section III.B.2).

A nonuniform barrier thickness will indeed cause a randomization in the phase, but since this happens only <u>spatially</u>, the interference effects predicted by both AAS

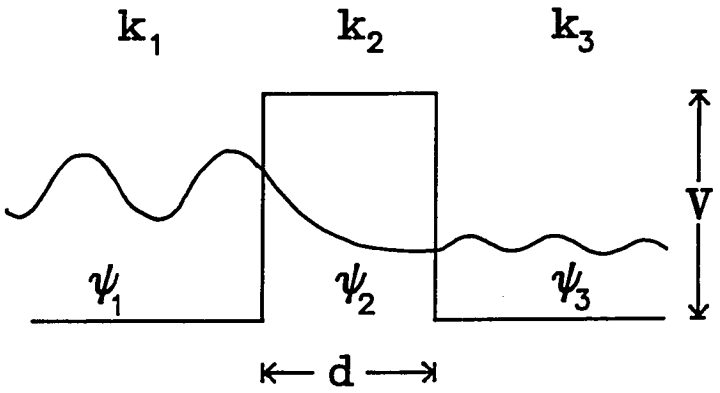

Fig. III-9: Model of a tunneling barrier at zero bias. A wave $\psi_1=\alpha_1 e^{ik_1 x}$ is attenuated by the barrier, and produces $\psi_3=\alpha_3 e^{ik_3 x}$ on the right-hand side.

and non-AAS theories will likely not be effected qualitatively (see sections I.B and III.B.2). As long as inelastic processes are avoided, even pinholes in the oxide barrier could likely be tolerated.

A stronger objection to the use of tunnel junctions for this experiment concerns non-ideal tunneling transmission. Impurities in the barrier could cause significant inelastic scattering. However, we know that *superconducting* junctions can show quasiparticle coherence effects. This demonstrates that energy changes in transmission must be much less than Δ (the superconducting energy gap) [Face et al., 1986]. In our fabrication of normal-metal tunnel junctions we draw heavily upon Josephson-junction technology. Another serious case of non-ideal transmission is indirect tunneling via traps in the oxide. These traps, if present, can change the tunneling properties in a time-dependent way. However, tunneling via traps usually occurs only at voltage biases of ~50 to 100 mV. Our experiments use a voltage drop less than k_BT~0.1 mV. These effects comprise at most a few percent of the total tunneling current at low bias voltages [Halbritter, 1985].

IV. Experimental Results

IV.A. Measurement Techniques

In these experiments we have employed both DC and AC measurements. For either type of measurement the samples are mounted on a cryostat designed by Dalrymple [Dalrymple, 1983, 1984], and cooled by a standard pumped-liquid-He^4 system. The system provides temperatures down to ~1.2 K. Proper sample mounting is critical, and has been described in chapter II.

Magnetoresistance (MR) measurements are made with a four-terminal AC bridge (Fig. IV-1). For a standard 179 Ω sample, this bridge has a resolution of roughly one part in 10^6 [Chandrasekhar, 1987]. The balance resistor is at room temperature, and is calculated to generate (for the 179 Ω sample) a Johnson noise of 1.7 $nV/\sqrt{Hz}$. The amplifier noise referred to the input of the lockin's transformer is less than this. Most AC measurements use a frequency of 500 Hz and a bandwidth of < 1 Hz, with a time constant ≥ 0.3 s. The current is kept low enough to avoid self-heating -- typically 1-10 μA. The procedure for detecting self-heating is described in [Santhanam, 1985, p.73]. AC measurement of junctions will be discussed in section IV.D.2.

The sample block is connected via a weak thermal link to the He bath. A resistive heater on the sample block allows dynamic control of the temperature. An analog "PID" (proportional, integral, and differential feedback) control circuit built by Chandrasekhar stabilizes the temperature to within 1 mK.

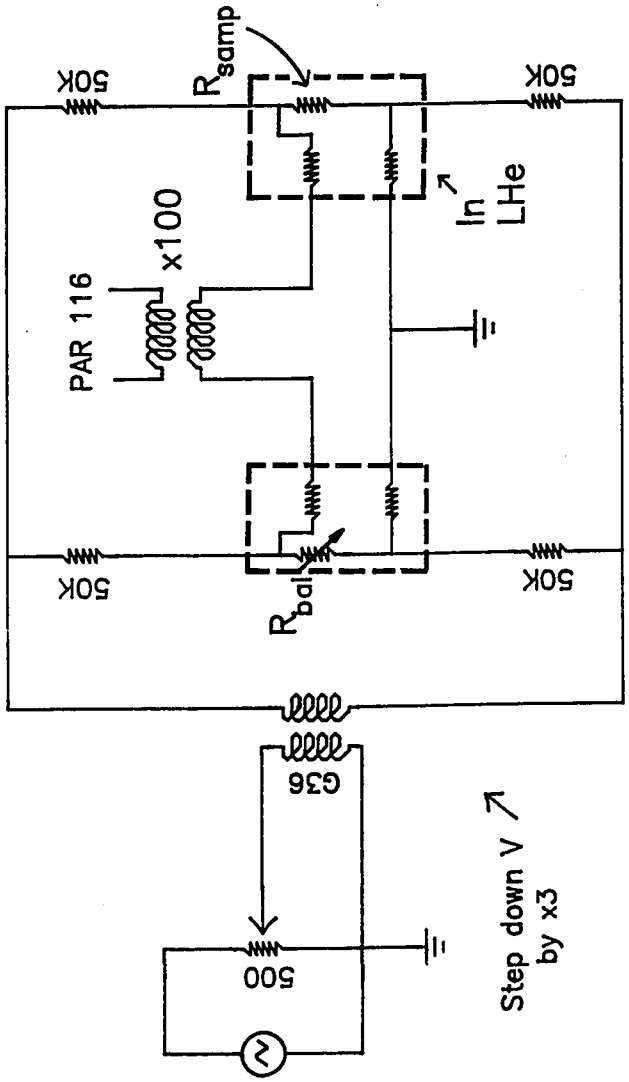

Fig. IV-1: Four-terminal AC bridge used for magnetoresistance measurements. The balance resistor is at room temperature. Resolution is approximately one part in 10^6. Most AC measurements use a frequency of 500 Hz and a bandwidth < 1 Hz. Dotted lines enclose lead resistances associated with the sample and the balance resistor.

The magnetic field is driven by a computer-controlled superconducting magnet (calibrated by Dalrymple). A Hewlett-Packard Series-200 computer first sets the magnetic field, then reads voltages indicating the sample resistance and magnet current from a pair of HP3478A multimeters (Fig. IV-2). For measurements of R(T) the computer monitors the meters passively, while the temperature is ramped slowly by hand.

DC measurements employ this same cryostat. A constant-current source drives a current through the sample, while a pair of buffer amplifiers are used to measure I and V. These electronics are detailed in the thesis of D. W. Face [Yale, 1987]. By adding an AC component to the DC bias, one can measure also dV/dI and d^2V/dI^2. When necessary, data are logged by a computer which passively monitors the voltmeters.

IV.B. One Dimensional Electron-Electron Scattering With Small Energy Transfers

IV.B.1 Experiments at Yale

The wires used in this study [Wind et al., 1986; Wind, 1987] were in the shape of meander lines (Fig. IV-3), ~50 μm long, with widths from 35 nm to 110 nm (±5 nm). These widths were determined from examination in a JEOL 100CX STEM in its SEM mode, at the Yale Medical School. For all of the samples the widths were verified with electrical measurements. Thicknesses were ~20 nm, as measured by a quartz-crystal thickness monitor. 2D films were codeposited with each set of wires, so that 2D properties could be compared to 1D properties.

The main goal of these experiments was to verify the temperature dependence

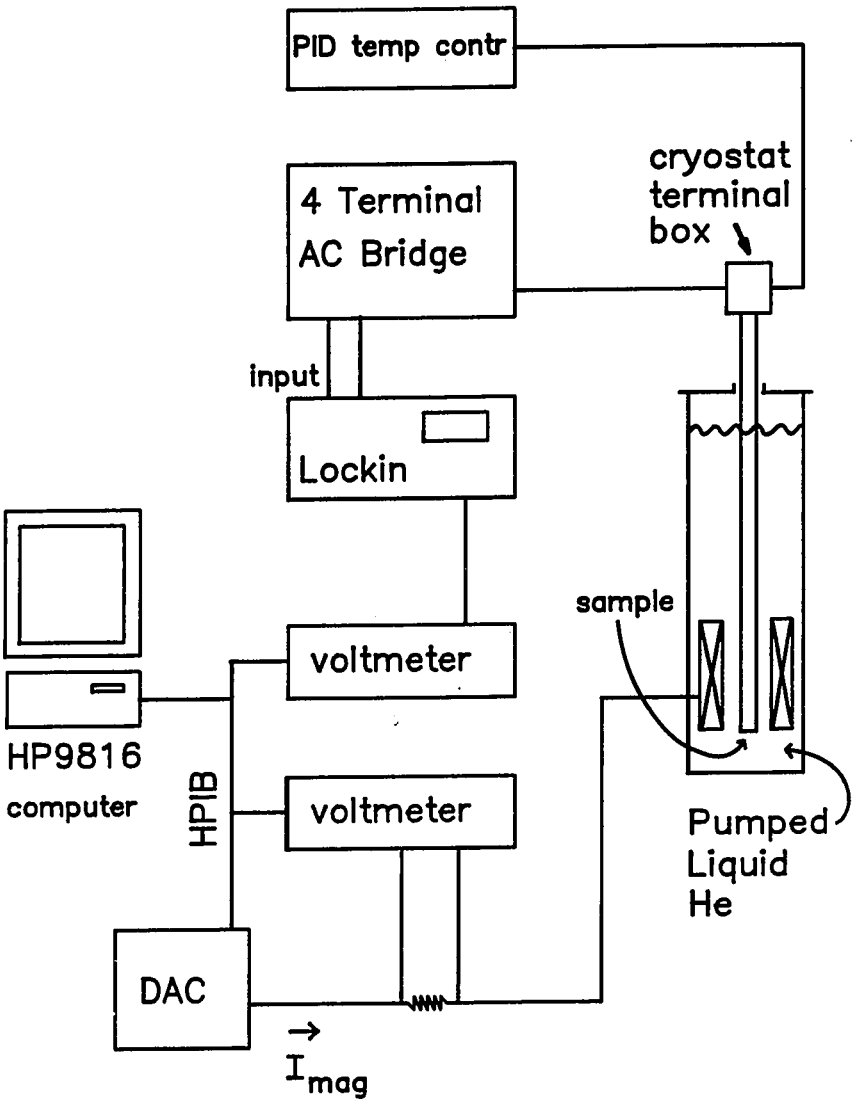

Fig. IV-2: Schematic diagram of the AC measurement apparatus. A Hewlett-Packard Series-200 computer first sets the magnetic field, then reads R and B data from a pair of HP3478A multi-meters. For measurements of R(T) the computer monitors the meters passively, while the temperature is ramped slowly by hand.

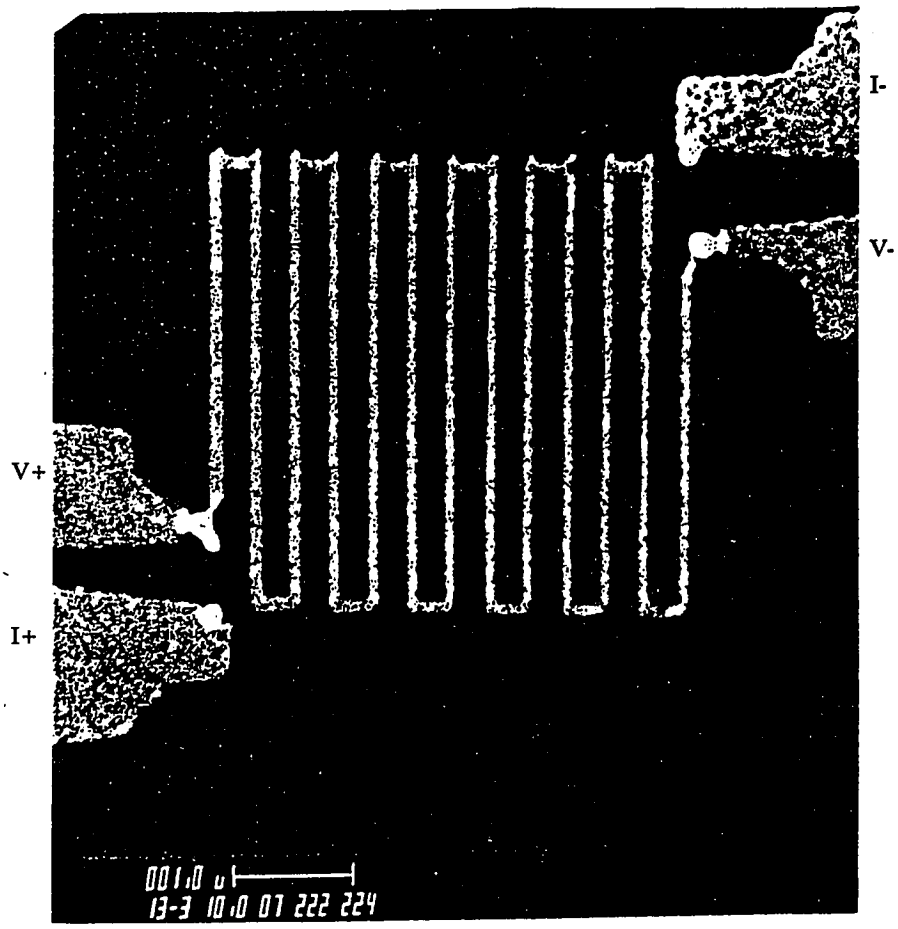

Fig IV-3: Meander line used in measurements of electron-electron scattering. After measurement this wire was accidentally destroyed by electrostatic discharge (i.e., causing the breaks between voltage and current probes). This wire has a linewidth ~110 nm. Wires as narrow as 35 nm have been fabricated and measured. Size-bar at the bottom shows 1 μm.

and width dependence predicted by Altshuler et al. [AAK, 1982], eq. III-5. To verify the width dependence groups of wires were evaporated at the same time, so that their material properties would be identical; the wires differ only in width. Table IV-1 shows all of the relevant sample parameters for the wires used in this study.

Table IV-1. Sample Parameters of 1D Wires

Sample	W (nm)	$R_\square$ (Ω)	D (cm^2/sec)	A_{ee}/A_{ee}^{theory}	$10^{-7}A_{ep}$ ($K^{-3}sec^{-1}$)	T_c (K)	ℓ_{so} (μm)	ℓ_s (μm)
Al1a	35	1.8	39	1.02	2.0	1.44	0.45	-
Al1b	46	1.8	39	1.03	2.1	1.44	0.45	-
Al2a	40	1.4	49	0.94	2.4	1.36	0.55	-
Al2b	60	1.4	49	1.04	2.1	1.36	0.55	-
Al2c	62	1.4	49	1.32	2.0	1.36	0.55	-
Al2f	film	1.3	53	film	1.6	1.36	0.55	-
Al3	110	1.1	63	1.11	2.0	1.32	0.56	-
Ag1	60	2.6	48	1.10	4.4	-	0.32	1.80
Ag2	100	1.5	85	1.06	2.2	-	0.52	1.19

Fig. IV-4 shows the magnetoresistance (MR) of wire Al2a at three representative temperatures. These and other MR data were fit to eq. III-4, using ℓ_ϕ

and ℓ_{so} as fitting parameters. For Ag it was found that a more consistent fit could be made when the magnetic scattering length ℓ_s was included as a parameter. When ℓ_s was not included in the fit, the values of ℓ_ϕ were seen to saturate at low temperatures. Eq. III-4 is expected to be valid up to fields of $12H_w = 12\hbar c/(4eW^2) = 1.6\ W^{-2}$ gauss, with the width in μm. For a 40 nm wire, $12H_w = 12$ kgauss. However, fitting to fields less than ~500 gauss is preferable, since $\beta(T/T_c)$ is depressed at higher fields. Larkin's β is valid for magnetic fields less than $k_B T_c \ln(T/T_c)/(4eD)$ [Lopez dos Santos and Abrahams, 1985].

For aluminum we could use the data from dH_{c2}/dT to determine the diffusion constant, as was done in the work by Santhanam [1985]:

$$D = \frac{-4k_B c}{\pi e (dH_{c2}/dT)} \qquad \text{(cgs)} \qquad \text{(IV-1)}$$

where H_{c2} is the perpendicular critical field [Tinkam, 1975; Santhanam, 1985 appendix F]. For our Al wires the diffusion constants were estimated by using values of $\rho_o \ell$ as a function of ρ_o from [Santhanam, 1985]. For Ag the diffusion constant $D = v_F \ell/3$ can be estimated by using measured values of $\rho_o \ell$ [Gershenzon et al., 1982].

Fig. IV-5 shows values of ℓ_ϕ inferred from the MR data. The solid lines are fits to $\tau_\phi^{-1} = A_{ee}T^{2/3} + A_{ep}T^3$, which includes the $T^{2/3}$ dependence of eq. III-4, as well as the T^3 dependence of 3D electron-phonon scattering. The dimensional length scale for electron-phonon scattering is generally taken to be the phonon wavelength, $\lambda_{ph} = (\pi\hbar v_s)/(2k_B T)$, where v_s is the transverse sound velocity [Bergmann, 1982]. For Al, the phonon wavelength can be written as $\lambda_{ph} = (365/T)$ Å, with T in K.

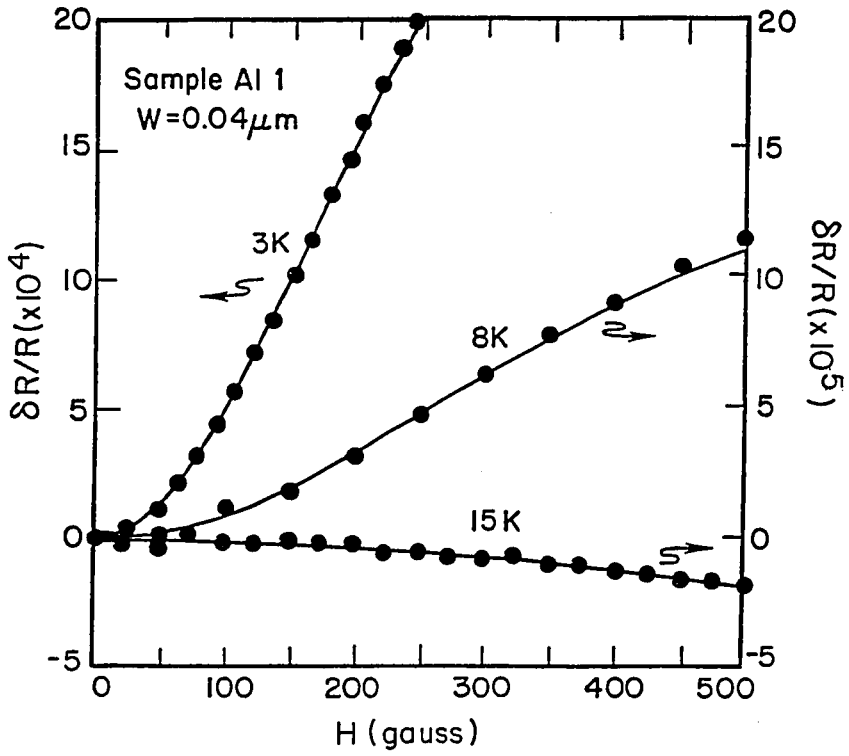

Fig. IV-4: Magnetoresistance of wire Al2a at three representative temperatures. Solid lines are fits to eq. III-4, using ℓ_ϕ and ℓ_{so} as parameters. From [Wind et al., 1986].

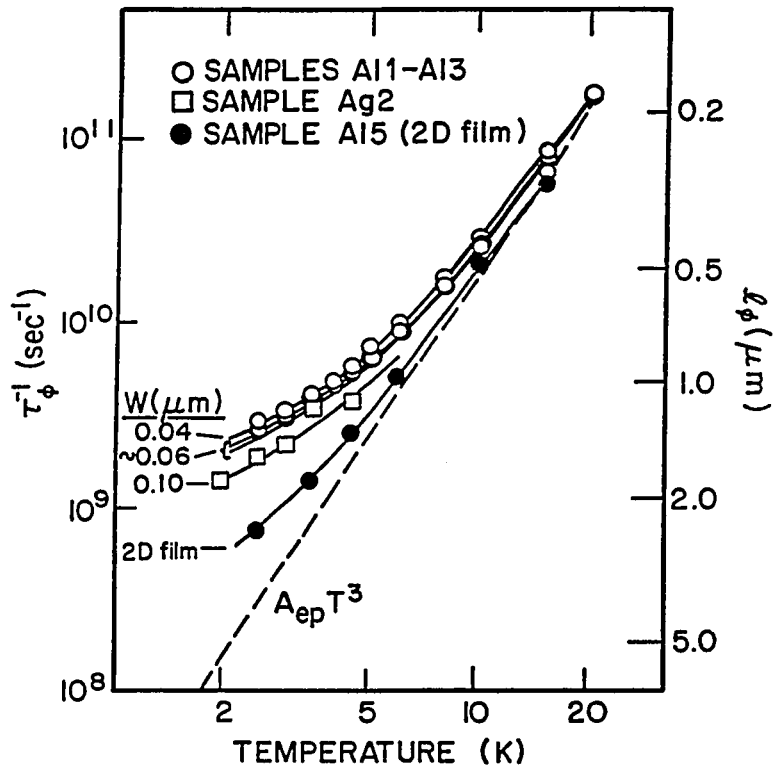

Fig. IV-5: Values of ℓ_ϕ and τ_ϕ vs. temperature, inferred from the MR data. The solid lines are fits to $\tau_\phi^{-1}=A_{ee}T^{2/3}+A_{ep}T^3$, which includes the $T^{2/3}$ dependence of eq. III-4, as well as the T^3 dependence of 3D electron-phonon scattering. Note that the scattering rates in wires are signigicantly higher than those of 2D films. From [Wind et al., 1986].

The elastic scattering length is sometimes considered to be the dimensional scale for electron-phonon scattering [Santhanam, 1985], but in any case, our samples appear to be effectively 3D for this scattering mechanism.

Another important test of the AAK theory is a study of the width dependence at a fixed temperature. Quantitative agreement with AAK is excellent, and the reader is referred to [Wind et al., 1986] and [Wind, 1987] for complete details. The wider wires ($W > \ell_T$) of previous studies by Santhanam, Wind, and Prober [1984] were 1D with respect to ℓ_ϕ, but showed electron-electron scattering rates identical to those of coevaporated 2D films. Comparison of the data from these wider wires ($W > \ell_T$) with those from recent studies of narrow wires ($W < \ell_T$) [Wind et al., 1986] confirms that ℓ_T is the length scale determining the dimensionality for electron-electron scattering. Our experiments on narrow wires of Al [Wind et al., 1986] also show that when $W < \ell_T$ the phase-breaking rate is dominated by electron-electron scattering with small energy transfers (the "Nyquist rate"), as predicted by AAK.

IV.B.2. Comparison With Other Work

In the study by [Lin and Giordano, 1986] it was claimed that the 1D Nyquist rate was observed in a 46 nm-wide AuPd wire. This wire was wider than the dimensional length scales for both the triplet and singlet terms of eq. III-4: $\ell_2 = 10$nm and $\ell_1 \sim 30$nm. Also, the wire was wider than $\ell_T \sim 18$ nm at 5 K. Their use of the 1D localization theory for the fitting process was therefore inappropriate.

In a study by Choi et al. [1986, 1987], narrow wires of GaAs demonstrated the 1D Nyquist rate. They found that data from narrow wires fit the form

$\tau_\phi^{-1}=A_{cl}T^2+A_{ee}T^{2/3}$. The T^2 dependence is from the clean-limit ($\hbar/\tau << k_BT$) electron-electron interaction [Ashcroft and Mermin, 1976, p.348]. For their 0.3 μm-wide wire, $A_{ee}/A_{ee}^{theory}=0.72$; for their 0.2 μm-wide wire they found $A_{ee}/A_{ee}^{theory}=0.81$. A comprehensive review of many other relevant experiments can be found in [Wind, 1987].

IV.C. Aharonov-Bohm Effect Experiments

IV.C.1. Experiments at Yale on Single Rings of Al and Ag

The rings we have studied are of area ~1 and ~4 μm^2, with film thickness ~250 Å. Linewidths were between 400 and 2300 Å. Fig. IV-6 shows micrographs of two typical rings. Sample parameters for the earlier studies are given in table IV-2. Fig. IV-7 shows the magnetoresistance (MR) of a 2.3 μm diameter circular ring of Al at 1.7 K. The oscillations have a flux period of h/2e, as predicted by [Altshuler et al., 1982a]. The length $\ell_\phi=1.7$ μm is determined from fitting the MR to equation III-11, using ℓ_ϕ and ℓ_{so} as parameters. The inset of Fig. IV-7 shows the high-field MR data for a similar ring. For this ring, data are available (at 4.5 K) which allow extraction of ℓ_ϕ by fitting either the low-field oscillations or the high-field data. These values of ℓ_ϕ (~1.2 μm at 4.5 K) agree to within 20%. However, we were not able to fit the low-field data much beyond a few oscillations. Just as in the case of wires, the high-field MR at low temperatures cannot be fitted well. For short samples ($\ell_\phi \sim \pi r$) this problem becomes worse. However, values of ℓ_ϕ derived from fitting low-field oscillations are in good agreement with the results from Al films and wires [Santhanam et al., 1984a,b; Gordon et al., 1984].

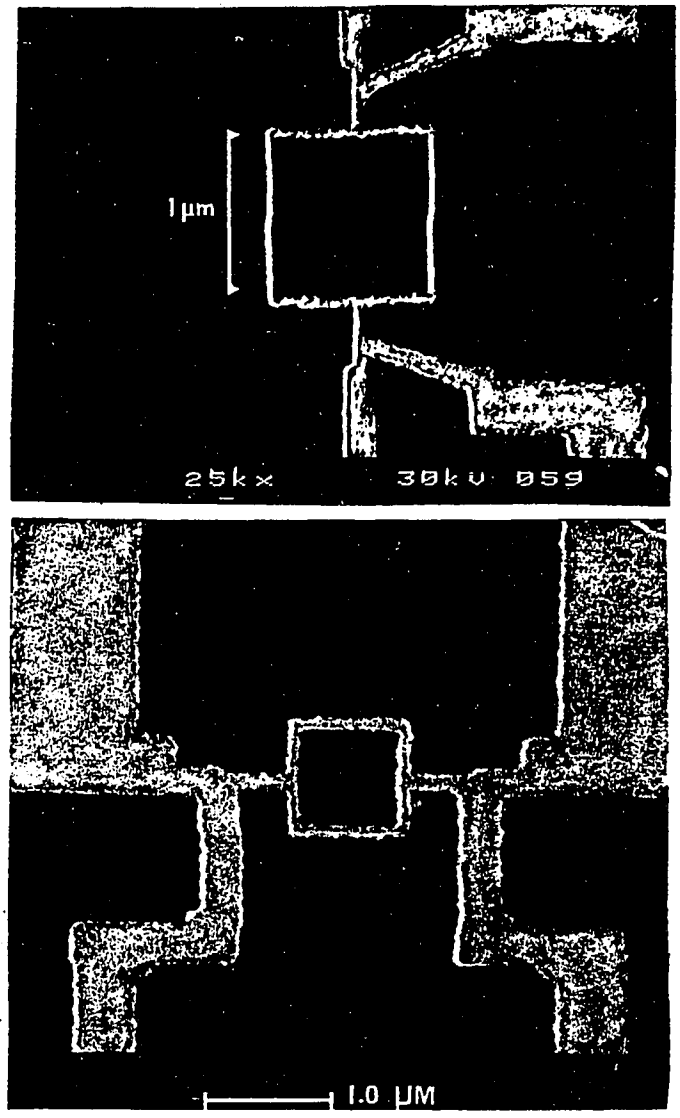

Fig. IV-6: Rings used for Aharonov-Bohm experiments. Ag and Al rings are fabricated on oxidized silicon substrates. Four-terminal lead structure is shown. In upper figure, the electron beam raster scan for exposure is in the vertical direction.

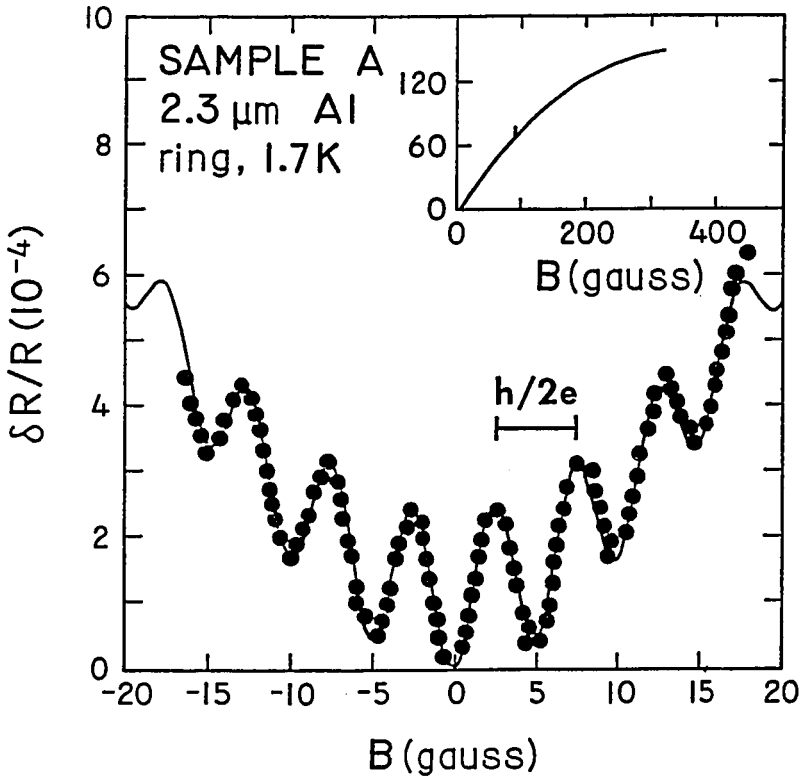

Fig. IV-7: Magnetoresistance (MR) of a 2.3 μm diameter circular ring of Al at 1.7 K. The oscillations have a flux period of h/2e, as predicted by Altshuler et al. [1982a]. Inset: high-field MR. From [Chandrasekhar et al., 1985].

Table IV-2. Sample parameters of rings.

Sample	Film	$R_\square$ (Ω)	Diameter (μm)	W (μm)	ℓ_ϕ (μm)	h/e effect
A	Al	1.1	2.3	0.19	1.7	(a)
B	Al	1.6	2.3	0.23	2.0	(a)
C	Al	3.0	1.1	0.19	1.0	uncertain
D	Ag	2.5	1.0	0.14	0.9	yes
E	Ag	1.6	1.0	0.14	0.7	yes

(a) h/e interference was not searched for in this sample

Magnetoresistance oscillations in Al rings are seen at temperatures up to 6 K. At a temperature of 1.7 K, $\beta \sim 5$, so that the MT contribution to eq. III-11 is dominant. At a temperature of 6 K, $\beta \sim 0.5$, so that at this temperature the localization contribution is significant. h/2e oscillations have been seen in more than 20 Al rings, and more than 5 Ag rings. One Ag ring studied did not show h/2e oscillations.

Fig. IV-8 shows the data from a 1 μm Ag ring, where the resistance oscillates with period h/2e at low fields, and with period h/e at higher fields. The h/2e oscillations in Ag rings are observable to 8 K, and the h/e oscillations are observable to 10 K. While the h/2e oscillations die out around 100 gauss, the h/e oscillations persist to the highest field measured, > 1 kgauss. The high-field data are seen to follow a "beating pattern", consistent with the simulations discussed in section

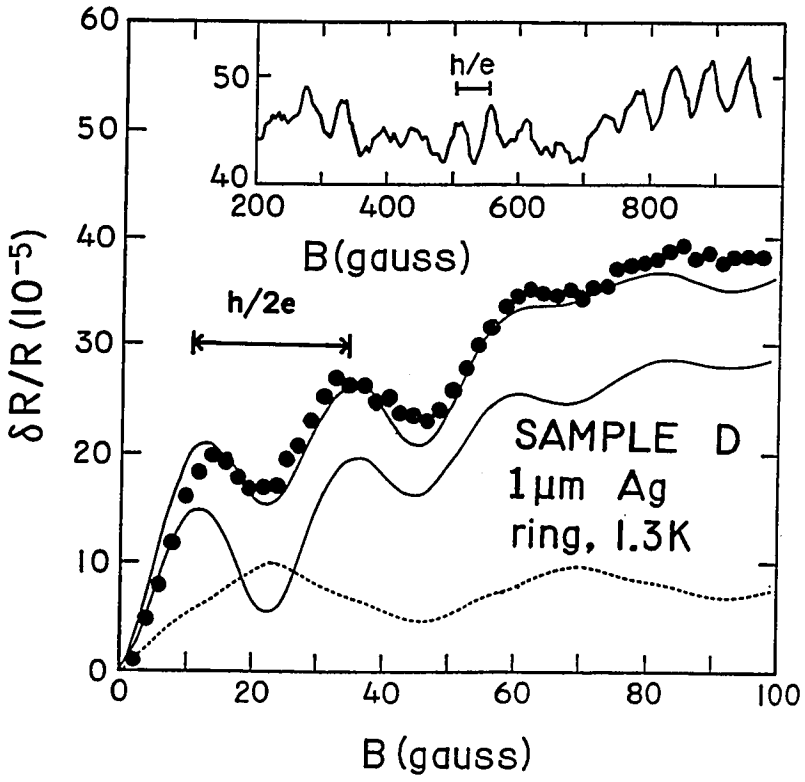

Fig. IV-8: Data from a 1 μm Ag ring, where the resistance oscillates with period h/2e at low fields, and with period h/e at higher fields. The lower solid line in the low-field data is a fit to the AAS theory (eq. III-11). The dotted line is an h/e contribution which, when combined with the AAS fit, gives the upper solid line. From [Chandrasekhar et al., 1985].

III.C.2.ii [Stone and Imry, 1986] and the experiments of Webb et al. [1985].

The low field data from the Ag rings cannot be fit with the AAS theory alone (eq. III-11). However, if one adds to the fit an h/e contribution, the low-field data appear to fit rather well, as shown in Fig. IV-8. Here it is also necessary to assume that the h/e contribution is damped, consistent with beating seen in the high-field data. Such a contrived fit obviously does not prove the existence of h/e oscillations at low fields; rather, it shows that AAS oscillations (h/2e) *are* clearly evident, and allows us to fit a value to the flux period. A fit is necessary to find the flux period, because for the low-field data there are too few oscillations to make a meaningful Fourier transform. The fitted h/2e period shown in Fig. IV-8 is 24 gauss, corresponding to r=0.53 μm. A Fourier transform of the high-field data shows a peak at ΔB=52 gauss, for an effective radius of 0.50 μm.

We may compare these results with the non-AAS theory [Stone and Imry, 1986, and refs. therein]. For simplicity we compare this theory to the Ag data, for which there are no superconducting fluctuation effects.

The g's of eq. III-15 [Stone and Imry, 1986] require several corrections before they can be compared to experiment:

(1) The temperature of 1.7 K can be included as a multiplicative damping factor of $(k_BT/E_c)^{-1/2}\sim 0.28$, where $E_c=hD/L^2$, L~1.5 μm, D~60 cm^2/s;

(2) The aspect ratio of Stone and Imry is defined as (flux through hole)+(flux in annulus); the theory uses a value of 4. Our Ag rings have an aspect ratio of ~1.8. The correction for this would require a different simulation, but is expected to be of order unity [Stone, 1987];

(3) Eq. III-15 applies to $2\pi r < \ell_\phi$. For our case, $2\pi r \sim \ell_\phi$. The correction factor does not appear to have a simple analytical form, and would once again require a separate simulation. The correction would have different effects on the two amplitudes, since for the Ag rings $\pi r \sim \ell_\phi$ and $2\pi r > \ell_\phi$.

Considering the three corrections which need to be applied to compare the non-AAS theory with our data, we can only say that the numerical simulations of Stone and Imry [1986] predict that the amplitude of the h/e oscillations should be much larger than the h/2e oscillations. For the Ag rings this is clearly not the case. In our experiments [Chandrasekhar et al., 1985] the h/e amplitude is $\sim 0.04e^2/h$. For its first oscillation the Ag h/2e amplitude is $\sim 0.03e^2/h$. The low-field h/2e oscillations are damped by the magnetic field (Fig. IV-8), suggesting that AAS oscillations may dominate over the non-time-reversed path (non-AAS) mechanism.

The reason why simulations predict a small h/2e amplitude may be that these calculations employ a small number of channels and a small ensemble of scattering sites. In these simulations, h/2e oscillations arising from time-reversed paths appear to be more prominent for larger ensembles of scattering centers [Stone, 1987]. Localization (i.e., time-reversed path interference) appears to be the dominant h/2e mechanism for our rings at low fields.

IV.C.2 Comparison With Other Work

The first observation of the Aharonov-Bohm effect in metal film devices was by Sharvin and Sharvin [Sharvin and Sharvin, 1981; Altshuler et al., 1982a], who studied

Mg and Li films evaporated onto a 1 μm diameter fiber. Only the AAS h/2e oscillations were seen. These measurements were repeated by Gijs et al. [1984] for Mg cylinders, and by Gordon [1984] and Gijs et al. [1984] for Al cylinders. Cylinders such as these are roughly equivalent to a parallel array of rings, each ring having a thickness ℓ_ϕ. Arrays of rings [Pannetier et al., 1984] were fabricated by evaporation of metal onto the end of a "channel plate", and by electron-beam lithography. Hexagonal and square patterns of Al, In, Mg, Cu, and Au fabricated with this process showed AAS h/2e oscillations in the magnetoresistance, just as in the case of cylinders. Experiments on arrays of quench-condensed Li rings [Bishop et al., 1985] also showed h/2e oscillations. Petrashov et al. [1986] have also reported h/2e oscillations in arrays of Al rings.

Early experiments on single rings of AuPd [Skocpol et al., 1984; Umbach et al., 1984], AuGe and Si inversion layers [Skocpol et al., 1984], and GaAs rings [Blonder, 1984] revealed no periodic oscillations. The lack of periodic oscillations was most likely due to poor aspect ratios (hole area + annulus area) or non-optimal material properties (e.g., magnetic scattering). Measurement of aperiodic oscillations (so-called "reproducible noise") in AuPd rings [Umbach et al, 1984] was one of the earliest observations of "universal conductance fluctuations", an effect which attracted theoretical attention after the experiment [Stone, 1985; Lee and Stone, 1985; Altshuler and Spivak, 1985]. The fact that the Aharonov-Bohm effect was not observed in single rings was surprising, since a single ring is the simplest theoretical case. However, single rings are far more delicate and produce less signal, so the fabrication and measurement are more demanding.

The first published report of Aharonov-Bohm oscillations in single rings was by Webb and co-workers at IBM [1985], who found h/e oscillations in Au rings. The h/2e oscillations seen by Webb et al. were barely above the noise level, and probably correspond to the harmonic of h/e (eq. III-15) - *not* the AAS (localization) h/2e of eq. III-11. Soon after the first report, both h/e and h/2e oscillations were reported for Ag rings at Yale [Chandrasekhar et al., 1985], where h/2e oscillations were seen also in Al rings. The effects in Ag and Al seen at Yale were later reproduced at IBM [Umbach et al., 1986]. Recently, h/e oscillations have been seen in rings of Al at Yale [Chandrasekhar, 1987]. Datta et al. [1986] observed h/e oscillations in a ring formed by the layers of a GaAs/AlGaAs heterostructure.

Data from IBM [Webb et al., 1985] for 1 μm Au rings show h/e oscillations which persist to the highest measured fields, 160 kgauss. Later studies at IBM [Umbach et al., 1986] on small arrays consisting of N Ag rings have verified that stochastic averaging of the h/e oscillations leads to a $\sqrt{N}$ dependence of the amplitude of the h/e oscillation.

IV.D. The Normal-QUID Experiment: Preliminary Results

IV.D.1. DC Measurements

Fig. II-16 shows several views of an N-QUID device. The fabrication of this device with electron-beam lithography has been detailed in chapter II. Fig III-8 shows a conceptual diagram of the normal-state quantum interference device (N-QUID). By employing superconducting materials we can use low-temperature data to characterize the tunneling barrier, then raise the temperature above T_c to obtain data in the normal-metal regime. As mentioned in section III.D.2., we require that

such tunneling barriers show sharp nonlinearities (when $T < T_c$) in their superconducting current vs. voltage (IV) data, to show that their large resistance is due to tunneling, not simply to impurity scattering. Also, a sharp IV indicates that simple, elastic tunneling is the dominant tunneling process. Inelastic (phase destroying) tunneling events are less probable if the low-voltage tunneling is elastic. The current through a superconducting junction should rise sharply at a voltage corresponding to the sum of the superconducting gaps for the two electrodes [see, e.g., Tinkham, 1975] (Fig. IV-9).

The first devices fabricated used a base electrode of Al and a counterelectrode of Pb. The barrier of aluminum oxide (Al_2O_3) is produced by thermal oxidation. For such small linewidths and junction dimensions we have found that Pb films are often discontinuous, since Pb tends to form clusters and voids. This problem could likely be solved by evaporating onto a substrate cooled by liquid nitrogen. To avoid this problem with Pb, a counterelectrode of Al was used. Unlike Pb, Al tends to react with the barrier oxide, thereby reducing the barrier thickness. In studies elsewhere, large-area $Al/Al_2O_3/Al$ tunnel junctions have shown sharp IV characteristics [Blackford and March, 1968].

To observe sharp superconducting IV characteristics (Fig. IV-9) the device must be well below the transition temperature, T_c. For the Al used in our previous work, $T_c \sim 1.3$ K (see Table IV-1); unfortunately, the pumped-He^4 system can reach only ~1.2 K. By making the Al "dirtier" (by evaporating at a low rate, ~3 Å/s), one can increase the T_c of Al to around 1.5 K.

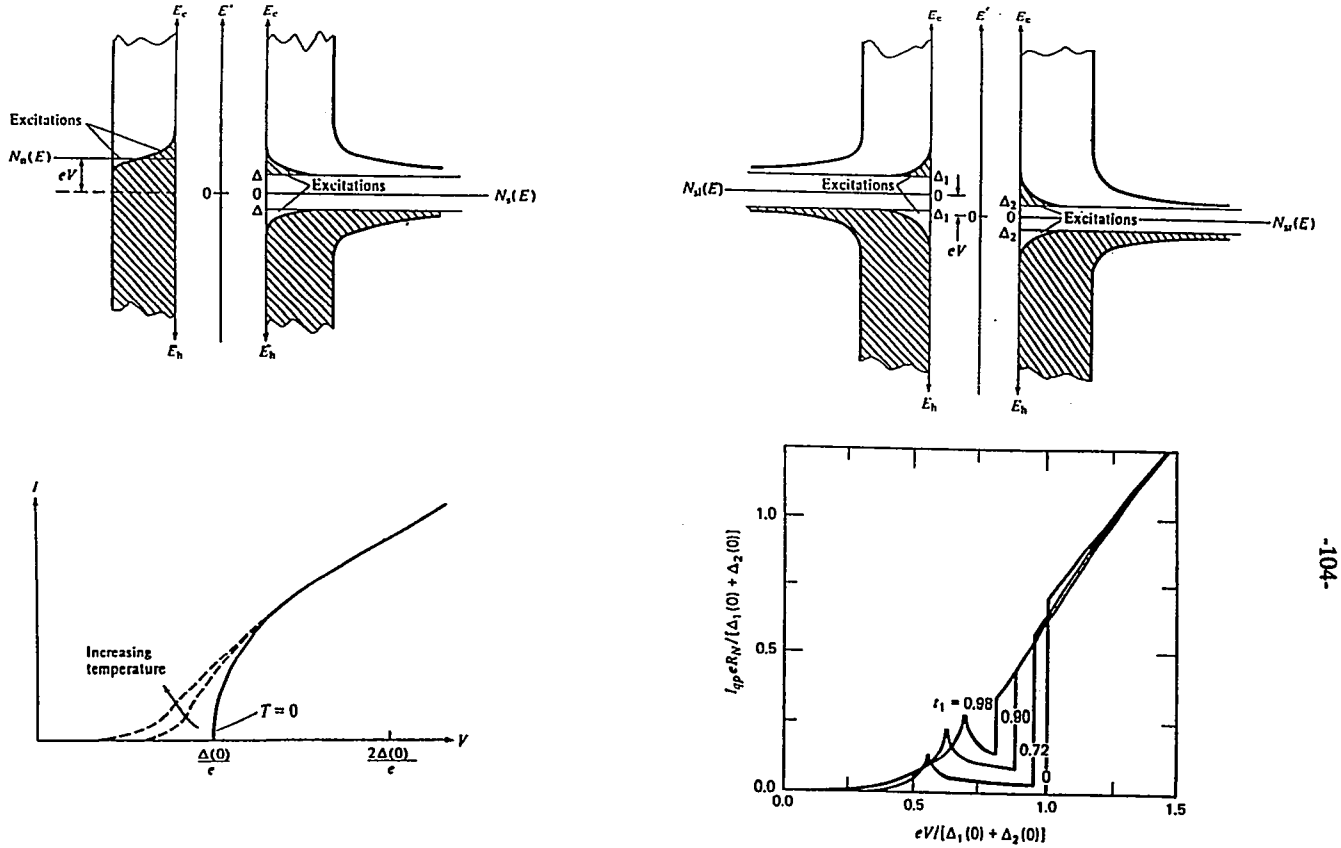

Fig. IV-9: a) Tunneling density of states for an SIN tunnel junction. b) I-V curve of an SIN tunnel junction for increasing temperature. c) Density of states diagram for an SIS tunnel junction showing the thermally excited quasiparticles. d) SIS tunnel junction I-V curve at several values of T/T_c. (a,b,c are from Van Duzer and Turner [1981]; d) is from Harris [1974]; as compiled by Face [1987]).

$Al/Al_2O_3/Al$ devices were made with high normal-state resistances (thick oxides), R~1 kΩ. We can estimate an expected value for the critical current I_c, using [Ambegaokar and Baratoff, 1963]

$$I_c R_N \sim \frac{\pi}{4} \frac{2\Delta(0)}{e} (1-T/T_c)^{-1/2} \qquad \text{(IV-2)}$$

where I_c is the critical current, R_N is the junction's normal-state resistance, and $\Delta(0)$ is the superconducting gap of Al at T=0 K. Using eq. IV-2, we find I_c~0.25 μA for the 1 kΩ junction at 1.2 K. This value is nominally above the measurement noise level; however, no critical current was observed in the two samples measured. All of the (five) high-resistance samples were destroyed by electrical transients before detailed IV curves could be obtained.

In an attempt to observe a critical current, lower resistance (R~20 Ω) $Al/Al_2O_3/Al$ junctions were fabricated. The three low resistance devices that survived measurement were entirely ohmic: IV data showed no critical current and no gap structure.

IV.D.2. AC Measurements

In order to observe interference due to electron paths which go all the way around the ring, the electrons must be capable of tunneling in either direction. Fig. IV-10 shows the Fermi levels in a voltage-biased N-QUID device. As long as there are neither inelastic scattering events nor radiative transitions, an electron tunneling to the right side of the ring will remain in a state above the Fermi level. From this

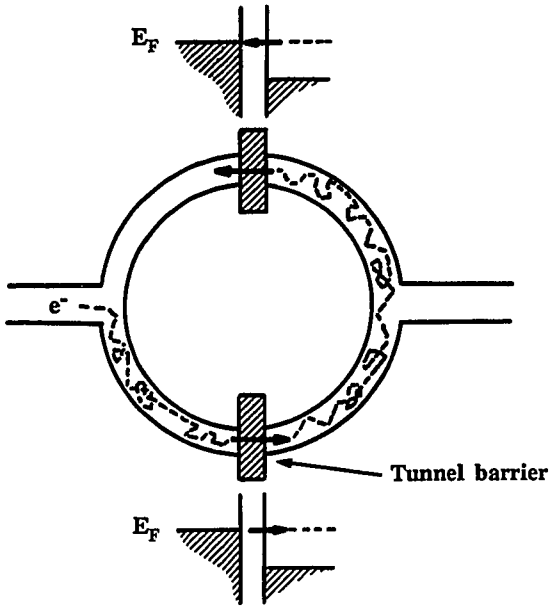

Fig IV-10: Schematic of a voltage-biased N-QUID device. An electron tunnels through a barrier, into a state above the Fermi energy. The electron undergoes neither inelastic collisions nor radiative transitions, and so remains at this energy. The electron is able to tunnel through the upper barrier. Not shown here are alternate (e.g., time-reversed) paths where the electron travels in the opposite direction (see Fig. III-5b). Such full paths around the ring allow the resistance to oscillate with a flux period of h/2e.

(a)

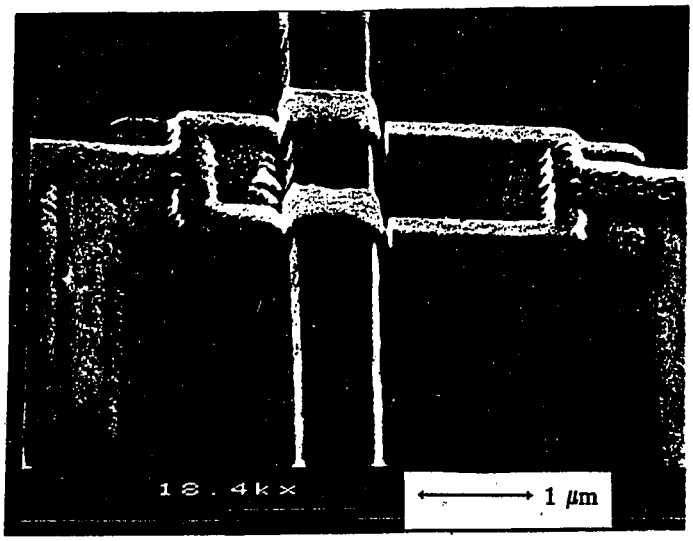

(b)

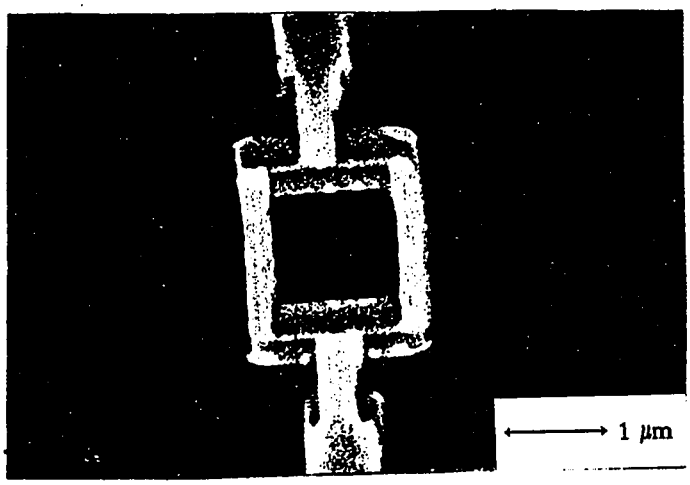

Fig. IV-11: (a) $Al/Al_2O_3/Al$ N-QUID device. (b) $Al/Al_2O_3/Al$ device fabricated without a step.

state the electron may tunnel to the left (against the voltage drop), as shown in Fig. IV-10. The voltage drop across the junction must be $\lesssim k_B T/e$, so that the electron will have a low probability of undergoing an inelastic transition to the Fermi level on the right-hand side.

AC measurements were made of devices similar to those shown in Fig. IV-11. High resistance (~1 kΩ) N-QUIDs were made with $Al/Al_2O_3/Al$ junctions, and the entire fabrication process was repeated *without substrate steps* (i.e., with metal rings instead of junctions), as shown in Fig. IV-11b. For this set of measurements the Al was fairly clean, $R_\square$~0.08 Ω. The total thickness is ~2000 Å, or roughly 8 times thicker than the rings described in section IV-B. The resistivity of this metal is then about three times less than for the rings of section IV-B.

Fig. IV-12a shows the MR of a ring with 2 kΩ junctions (similar to the device shown in Fig. IV-11). The trace reveals only noise. Fig. IV-12b shows the MR of a ring with similar material properties, but without junctions; h/2e oscillations are present. An approximate fit was made to eq. III-11. The ring has overlapping layers. Thus, the geometrical "radius" is not a well-defined quantity. For this reason the radius was used as a fitting parameter along with ℓ_ϕ. For the ring of Fig. IV-12, the effective radius is 1.38 μm; the average width is 0.56 μm; T_c is 1.25 K; T is 1.5 K; the resistance of the ring is 0.31 Ω; ℓ_ϕ has a fitted value of 3.45 μm.

(a)

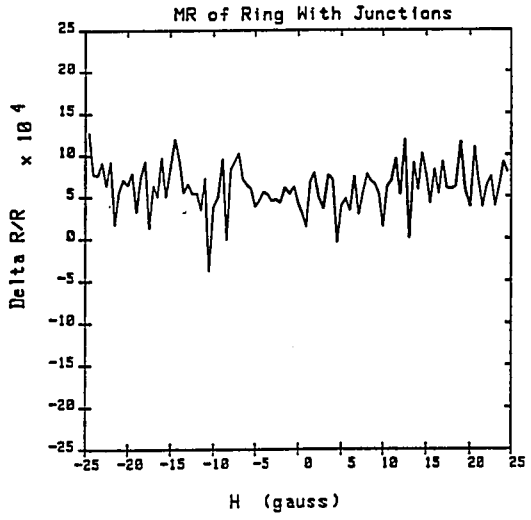

(b)

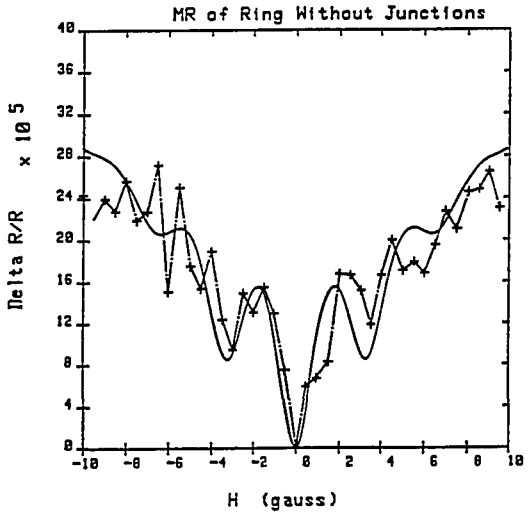

Fig IV-12: (a) MR of a normal-QUID with 2 kΩ junctions. The trace reveals only noise. (b) MR of a ring with similar material properties, but without junctions; h/2e oscillations are present. The radius has been fit to 1.38 μm, and the fitted value of ℓ_ϕ is 3.45 μm. Average width = 0.56 μm; T = 1.5 K; T_c=1.25 K; R=0.31 Ω.

IV.D.3. Future Directions For The Normal-QUID Experiment

From these experiments we can conclude that future progress will require a proper DC characterization of tunnel barrier properties. A counterelectrode which is less reactive than Al (e.g. Ag, Pb, or Pb-Bi alloy) will be necessary. Because the films used in this process are thin (<100 nm), the Pb-Bi may need to be evaporated onto a cooled substrate. Once the quality of the devices has been established, measurements can be made above T_c to observe N-QUID properties. A different base electrode, as well as a different counterelectrode, may be required. Since Al has shown only very weak (if any) h/e oscillations, it may be desirable to use a base electrode such as Mg.

Preliminary studies have shown the value of co-evaporating structures which are identical to N-QUIDs, but lack junctions. Such comparisons can tell us whether or not the junctions are suppressing the interference.

V. Summary and Conclusions

V.A. Scientific Issues

Devices with dimensions smaller than the phase-breaking length ℓ_ϕ have demonstrated corrections to the Drude conductivity which are determined by quantum interference effects. These effects have been observed in micron-size normal-metal rings of Al and Ag. Resistance oscillations with a flux period of h/2e, as predicted by Altshuler, Aronov, and Spivak (AAS), as well as oscillations with period h/e, have been observed in 1-2 μm diameter rings. These electron interference effects in metal rings are the solid-state analog of the Aharonov-Bohm effect for electrons in vacuum.

Low-field (H < 100 gauss) magnetoresistance data from Al and Ag rings were fit to the AAS theory [Altshuler et al., 1982a], using the phase-breaking length, ℓ_ϕ, and the spin-orbit scattering length, ℓ_{so}, as fitting parameters. Values of ℓ_ϕ derived from fitting low-field oscillations in Al samples are in good agreement with the results from Al films and wires [Wind et al., 1986; Santhanam et al., 1984a; Gordon et al., 1984].

Magnetoresistance oscillations with flux period h/2e and h/e are seen in Ag rings. While the h/2e oscillations die out after a few hundred gauss, the h/e oscillations persist to the highest field measured, > 1 kgauss. The high-field data are seen to follow a "beating pattern", consistent with the simulations discussed in section III.C.2.ii [Stone and Imry, 1986] and the experiments of Webb et al. [1985].

Narrow wires of Al and Ag, of width 35 to 110 nm, have been used to probe the electron phase-breaking rate. We find that this rate at low temperatures is dominated by one-dimensional electron-electron scattering with small energy transfers, as predicted by Altshuler et al. [AAK, 1982b]. Comparison of the data from wider wires (where the width W is larger than the thermal diffusion length ℓ_T) [Santhanam et al., 1984] with that from recent studies of narrow wires ($W < \ell_T$) [Wind et al., 1986] confirms that ℓ_T is the length scale determining the dimensionality of phase-breaking due to electron-electron scattering.

Experiments have begun on the "normal-QUID" device. This device consists of a ring with a tunnel-junction on each arm. The normal-QUID should show greatly enhanced Aharonov-Bohm oscillations, and is intended to test the high-resistance regime of the theory for quantum interference. Tunnel junctions for this device are made with an *in situ* junction fabrication technique adapted for e-beam lithography from an optical patterning method [Face and Prober, 1987]. So far, this experiment has not yielded unambiguous results, and further scientific progress will require further material characterization and device measurement.

The work on N-QUID devices has led to the technical development of alignment techniques which allow multilevel devices to be fabricated with any combination of e-beam and optical levels. Future device studies will benefit from fabrication experience and lithographic resolution gained in this work. Small tunnel junctions made with e-beam lithography can be used to observe the Aharonov-Bohm effect, and the Aharonov-Bohm effect can be used to study phase-breaking mechanisms in tunneling structures.

Several questions remain open for future investigation. The effect of magnetic impurities on the h/e and h/2e magnetoresistance oscillations is of interest. Aluminum shows very small h/e oscillations; this behavior could be unique to Al, or may be caused by a more general material property (e.g., superconductivity, grain size, impurities, etc.) The entire NQUID experiment remains unfinished, and so the high-resistance regime of normal-metal quantum interference remains unexplored, along with questions concerning phase-breaking mechanisms in tunnel junctions. Thus, exciting and interesting questions will also apply for the future.

V.B. Microfabrication Issues

Electron-beam lithography has been employed to fabricate devices for electron-transport studies. A modified scanning-electron microscope (SEM) has been converted for use as an electron-beam writer, and is now in general use for the production of devices with sub-0.1 μm linewidths. Scan control signals for the electron microscope are generated externally by a custom interface which provides a link between the computer and the SEM. Patterns are stored in the computer as a grid of 1024×1024 pixels. The e-beam interface generates raster-scan signals for the SEM electron beam, while sending the computer-generated pixel information to the electrostatic beam-blanker.

A hybrid deep-ultraviolet/electron-beam process has been developed for the fabrication of complete devices. Large features (> 10 μm linewidth) are exposed in PMMA using deep-ultraviolet (DUV) light ($\lambda \leq 220$ nm), then developed so that the pattern can be used for focusing and aligning the e-beam system. Various light sources - a Zn bulb, a Hg bulb, and two different collimated Hg-Xe lamps have been

characterized for DUV exposure.

Feature sizes as small as 30 nm have been produced with a process which uses a novel PMMA/PMMA bilayer electron-beam resist. This bilayer consists of two layers of PMMA of different molecular weights, with the higher molecular weight (lower sensitivity) polymer as the top layer. Both layers are exposed with a single exposure, and then developed with one development step. The typical problem encountered with multilayer resist systems is that the two resist layers may intermix, thereby reducing the effectiveness of either layer. To avoid this we have used xylene as the casting solvent for the top layer, since xylene is only a very weak solvent for PMMA. Most of the xylene evaporates from the top layer before any significant part of the bottom layer is dissolved. The two layers of PMMA are developed at one time with the same weak developer, so that any small interdiffused layer simply forms a thin region of intermediate sensitivity. The PMMA bilayer resist has made possible the fabrication of metal structures whose sizes are on the order of the electron phase-breaking length, ℓ_ϕ.

Appendix A: Standard Processes

I. Photolithography

1. Clean Si wafer (see, e.g., [Face, 1987]).
2. Oxidize wafer for 1 h at ~1000°C in a steam furnace. This produces ~500 nm of oxide.
3. Spin MP1450B (Shipley Co.) photoresist at 3000 rpm for 1 min. (Thickness ~0.5 μm).
4. Bake in air at 85°C for 10 min.
5. Expose with UV light through a contact or projection mask.
6. Develop pattern in MF-312:water 1:1 at room temperature (~23°C) for 1 min.
7. Etch underlying layer or liftoff a layer of metal.
8. Remove the photoresist in acetone. Alternatively, blanket expose and remove photoresist with MF-312.

II. Single-Layer E-beam Lithography

1. Clean a Si wafer (see, e.g., [Face, 1987]).
2. Oxidize wafer for 1 h at ~1000°C in a steam furnace. This produces ~500 nm of oxide.
3. Spin 950K MW PMMA, 4% in chlorobenzene, at 4000 rpm for 1 min.
4. Bake in air at 180°C for 30 min.
5. Expose with DUV light using a Cr-on-quartz mask (see section II.B).
6. Develop in MIBK:IPA (1:3) for 30 s at (23±1)°C.
7. Put the wafer in the e-beam system. Align and focus using the DUV pattern.

8. Expose with e-beam using the following parameters:

Mask:	intermediate pads (MIDDLE)
Voltage:	30 kV
Field:	38×38 μm (2.8 kx magnification)
Current:	38 pA
Working Distance:	5 mm
Final Aperture:	45 μm
Exposure Time Without Speed Control:	1 min. (1.8 μs clock period)

9. Increase the magnification, and expose with the following parameters:

Mask:	small device (e.g., a ring)
Voltage:	30 kV
Field:	15×15 μm (7 kx magnification)
Current:	15 pA
Working Distance:	5 mm
Final Aperture:	45 μm
Exposure Time Without Speed Control:	2.2 min. (4 μs clock period)

10. Remove the wafer from the e-beam system, and develop in MIBK:IPA (1:3) for 30 sec. at 23°C.

11. Evaporate 10 to 60 nm of metal, and liftoff by shooting acetone.

12. Store in liquid nitrogen to avoid contamination.

III. RIE of Si Steps: see [Face, 1987].

Appendix B: Electron-Beam Interface

This appendix provides the details of the electron-beam lithography interface, which has been described briefly in section II.D.3. The purpose of this appendix is to provide information necessary for the maintenance and improvement of the interface. The design of the raster-scan interface was motivated by the lack of a powerful computer; those facing the problem of SEM conversion may now find simpler solutions than the ones developed here.

One very simple and effective way to convert a SEM into an e-beam writer is through the use of three computer-controlled digital-to-analog (D/A) channels. One channel is used for the "X" coordinate, one for the "Y", and the third is used for turning the beam on and off ("blanking"). A pattern is formed, typically, by filling in rectangular shapes with either a spiral or a raster pattern. All of the patterning information is provided by a computer, which also "blanks" the beam between rectangles. This "vector scan" system was not used at Yale, because high-speed D/A cards were not available for the HP-87 computer then in use.

A. Block Diagram

Fig. A-0 shows a block diagram of the e-beam interface, which has been described in section II.D.3. The pin numbers appearing on the following diagrams (e.g. "H2", "F33") refer to locations on an Augat wire-wrap board. Almost all of the chips used are standard CMOS 4000-series.

1. Computer Controlled Enable

This circuit disables the raster interface from the IEEE-488 (or, "HPIB", or "GPIB") bus when the interface is not in use, and enables it when lithography is about to begin. To enable the raster interface, one sends the (Pascal) bus command LISTEN(7, 30), which sets the ATN line (pulls it to ground) and sets DIO1-DIO8 to 00111110 (ASCII ">"). To disable the raster interface, one sends the bus command UNLISTEN(7), which sets the ATN line and sets DIO1-DIO8 to 00111111. On the HPIB bus "1" is an active low, and "0" is a passive, floating TTL high voltage of ~3.5 V. The two eight-input NANDs recognize the bus commands and set the enable latch accordingly. Note that the actual enable signal is not set until the ATN line goes high, indicating the end of the bus instruction.

2. Byte Slicing

This section slices bytes into bits and sends them to the beam blank analog output. Mask data is taken in one byte (8 bits) at a time, and clocked out of a shift register.

Input:

DIO1-DIO8 - data lines from HPIB bus.

M/NM - mask/not mask; flips the bits of the mask to give the negative image of the e-beam pattern.

LD - load; asserted when a byte of data is made available on the bus.

X5 - fifth X counter bit; used to distinguish between pattern and speed-control data.

X2 - second X counter bit; used to clock the bits out of the shift register.

Output:

BBO - beam blanking output (logic level).

3. Clock Enable and Beam Blank

This section starts and stops the clock on various conditions, and sets override conditions on the beam-blank signal. The clock is stopped at the end of every horizontal scan line. The center flip-flop produces and end-of-line pause to allow the SEM scan coils to settle. This time is adjustable through the 50 KΩ pot, but in practice is always less than the pause created by the driver program.

Input:

CKST - clock start; equal to not-DAV, this sets a latch when data is valid.

X12 - twelfth X counter bit; indicates the end of a horizontal sweep.

Y12 - twelfth Y counter bit; indicates the end of a pattern.

RST - reset;

not-ATN - indicates when command data is on the HPIB bus.

MASK/LINES - formerly used to create single-line sweeps, this line to the front panel is no longer used. Single-line sweeps can be done from software.

Output:

CKEN - clock enable; this signal allows the counters to count.

BBK - beam blank override.

4. Handshake

This section communicates with the computer. The interface requests data by setting NRFD high (0). The computer responds by setting data on DIO1-DIO8, then indicates valid data by setting DAV low (1). The raster interface acknowledges receipt of data by setting NDAC (not data accepted) high (0).

Input:

X5 - fifth X counter bit; requests data.

DAV - HPIB line asserted (set low) by the computer when data on the bus is valid.

ENABLE - enables the raster interface to perform handshaking.

Output:

NRFD - not ready for data when this line is low.

NDAC - not data accepted; low when data has not been accepted.

CKST - clock start; asserted when DAV goes low at the beginning of a line.

An excellent introduction to HPIB (IEEE-488) can be found in HP-IB Interface Owners Manual, Series 80, p. 64-66 (HP part number 82937-90017), and IO Programming Guide, Series 80, p. 85-130 (HP part number 00085-90142 Rev. D 10/81).

5. Reset

This section generates a reset signal when the computer asserts (pulls low) the ATN line, when the "Reset" button is pushed, and when the power is turned on.

Input:

ATN - HPIB line which indicates a command on the bus.

Output:

RST - reset signal from front panel. If a pattern is being sent, then the driver program will timeout.

6. Load Decoding

This section determines when data should be loaded from the HPIB bus. Note that the distinction between pattern data and speed-control data is made by the X5 line in diagram 2.

Input:

X1, X2, X3, X4 - clock counter lines.

Output:

LD - indicates that data should be on the bus, ready to be used.

7. Turbo

The variable-speed raster section is called the "turbo drive". This section enables the interface to switch clocks. The FAST clock can be selected during long blank sections of the pattern. The "gears" provide for a smooth transition from one clock to another (see section II.D.3). The XNOR in the upper left corner waits until the external and the FAST clocks are either both low or both high before allowing the switch. The second XNOR in the center waits for the fast clock and the

external clock to match before switching back to the external clock. The BRAKE signal is generated with a 4013 monostable. This signal is intended to provide a settling time when switching from fast to slow clocks. In practice it is far simpler to control the settling time through software - by specifying the smallest unexposed area that can be marked as "fast".

Input:

LD - the load signal.

X5 - fifth X counter bit. Separates pattern data from speed-control data.

DIO1 - the data line that carries speed information

AUTORST - reset line that chooses the external clock upon power-on.

BRAKE ON - turns on the brake signal when switching from fast (internal) to slow (external).

Output:

CLK - final clocking line that toggles the X counter.

BRAKE - the settling time pause.

FAST - the fast clock signal (1 MHz).

8. Counters and DACS

This section provides the X and Y raster sweeps by feeding the lines of two twelve-bit counters into a pair of DACs.

Input:

CLK - clock.

RST - reset.

CKEN - clock enable.

Vxref and Vyref - reference voltage inputs for the DACs.

Output:

X1-X12 - X counter bits.

Y1-Y12 - Y counter bits.

Vxout and Vyout - raster sweep voltages (before analog processing).

9. Beam Blank Analog Output

This section converts the logic level blanking signal (BBO) into positive and negative blanking voltages. The 4512 multiplexer is used to select between pattern data and the override switch from the front panel.

Input:

BBO - logical beam blank signal.

BLANK - override signal from the front panel which forces the beam to blank.

UNBLANK - override signal from the front panel which forces the beam to unblank.

Output:

+ BLANK OUT - ~+9 V blanking signal to one plate of the beam blanker.

- BLANK OUT - ~-9 V blanking signal to the other plate of the beam blanker.

10. Raser Sweep Analog Output

This section provides a voltage reference for the DACs, and produces a bipolar (-Vref to Vref) analog output. The AD580 provides a reference voltage, and the

widths of the sweeps are controlled not by the gain of the output op-amps (LF356), but by the gain of the op-amps used for the voltage reference (OP-07).

Input:

Vxout and Vyout - zero to Vref sweep from the DACs.

XWIDTH and YWIDTH - pots on the front panel.

Output:

Vxref and Vyref - variable voltage reference for the DACs.

Xout and Yout - bipolar analog sweeps.

11. X and Y Filters

These filters are needed to remove high-frequency noise present in the X and Y raster sweep lines. The high-inductance scan coils of the SEM filter out some of the noise.

12. I/O to GPIB and Front Panel

These cables connect the board to the front panel, to the GPIB (HPIB) bus, to the blanking signal BNCs, and to the BNC from the external clock.

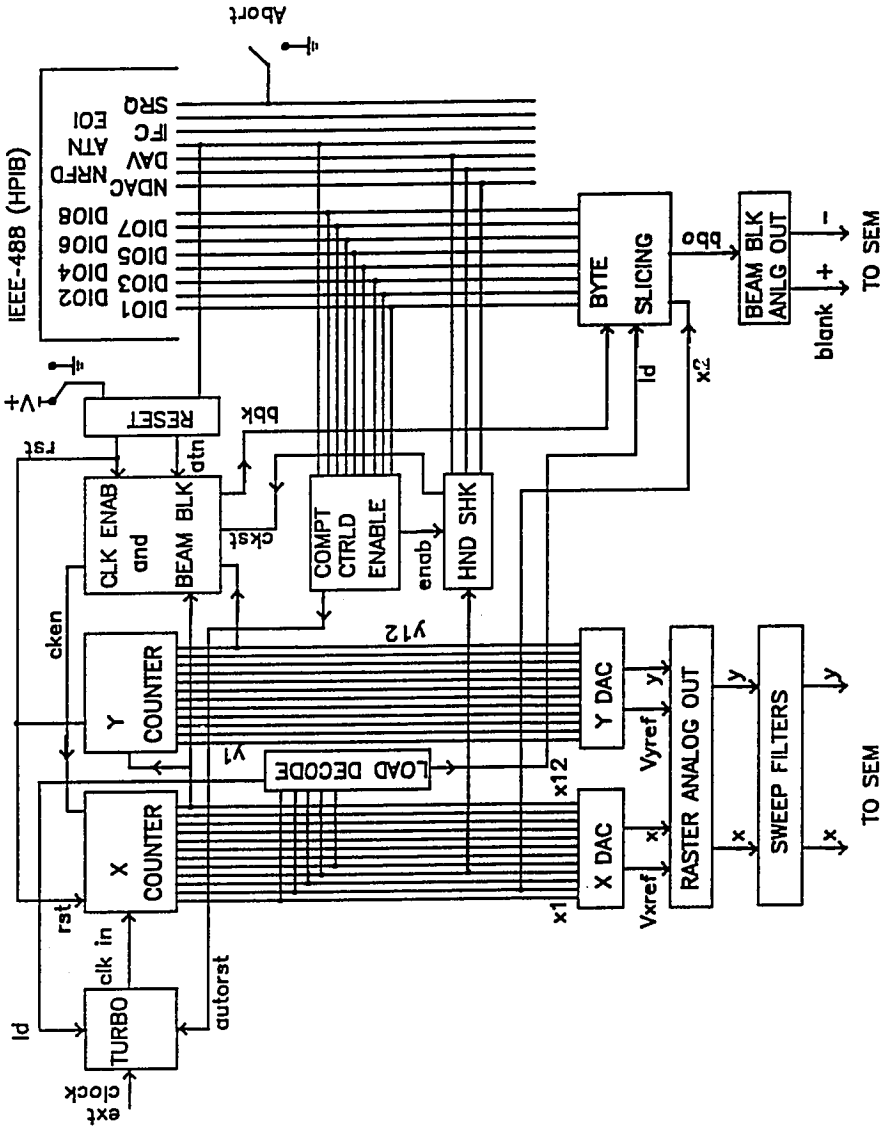

Fig. A-0: Block diagram of the e-beam interface.

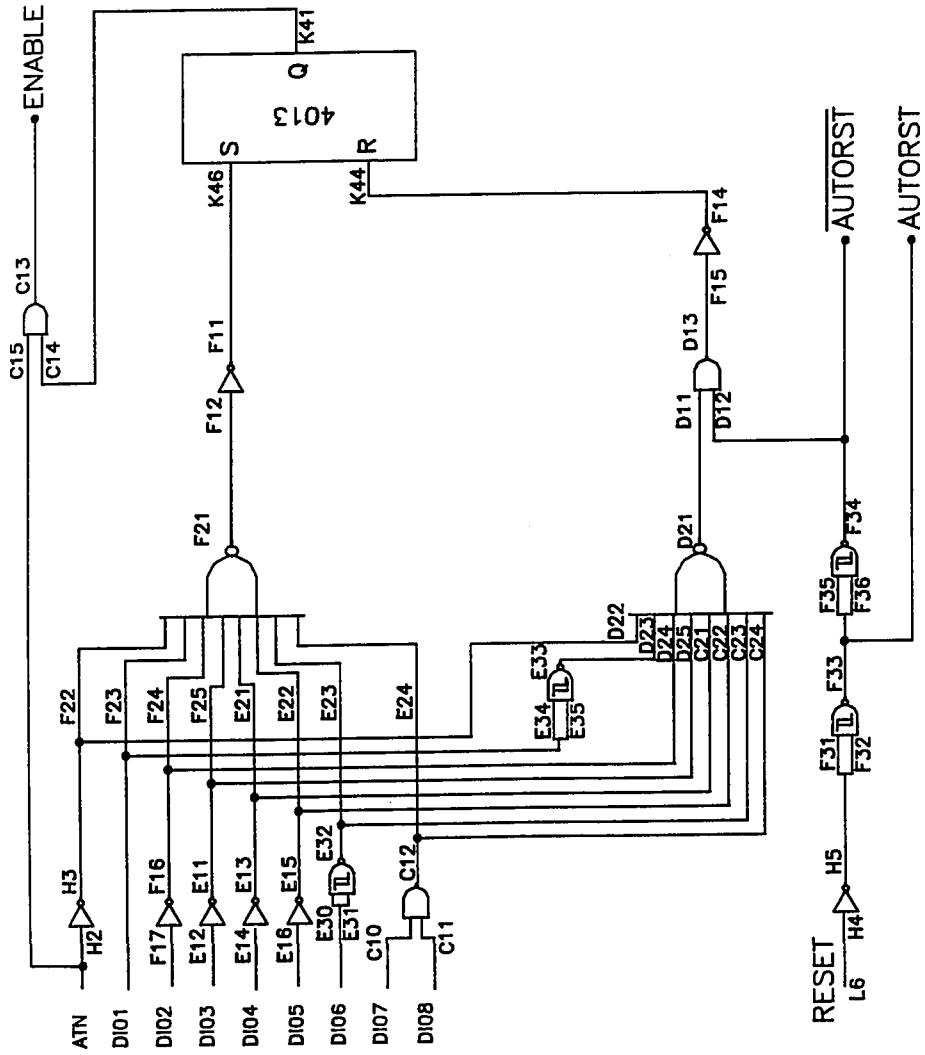

1. COMPUTER CONTROLLED ENABLE

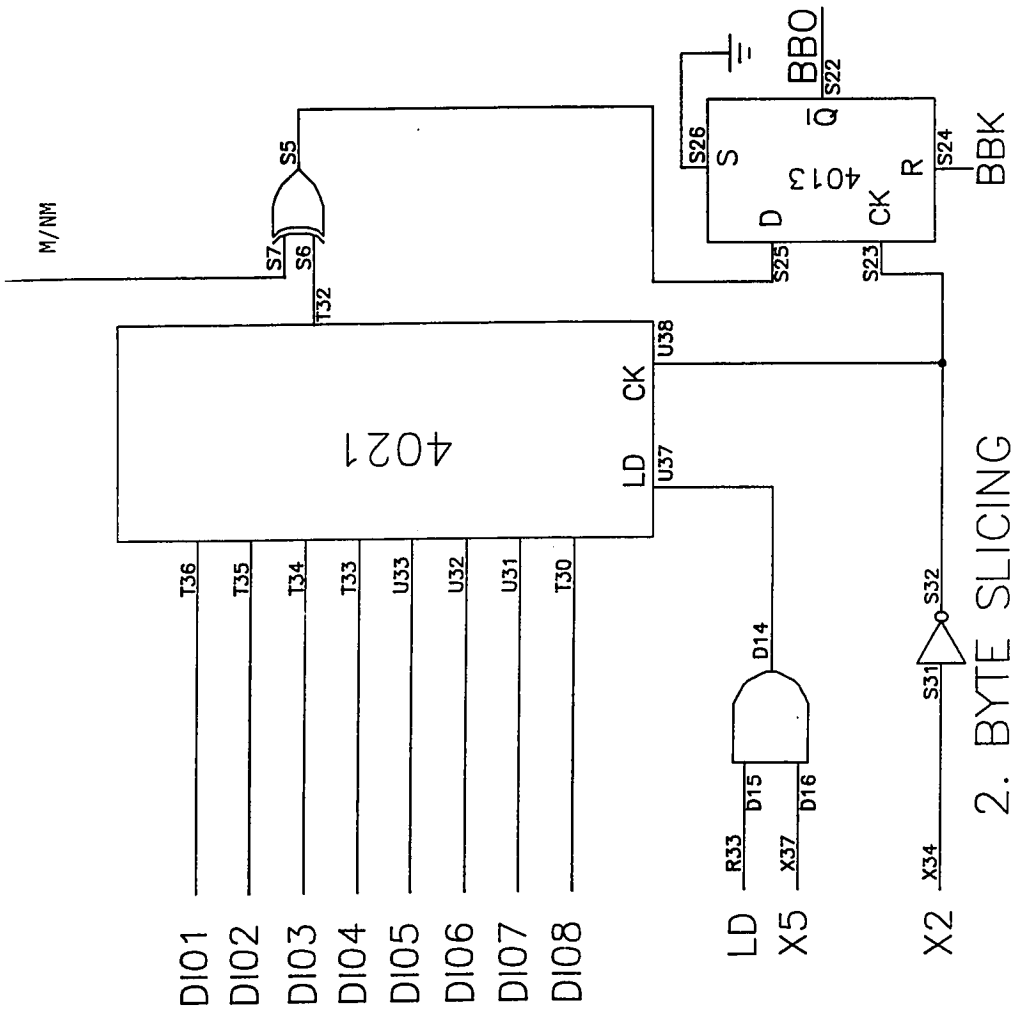
M/NM
S5
S7
S6
T32
4021
U38
CK
LD
U37
T36
T35
T34
T33
U33
U32
U31
T30
D101
D102
D103
D104
D105
D106
D107
D108
D14
D15
D16
R33
X37
LD
X5
S32
S31
X34
X2
2. BYTE SLICING
BBO
S22
S26
S
4013
D
CK
R
Q
S24
BBK
S25
S23

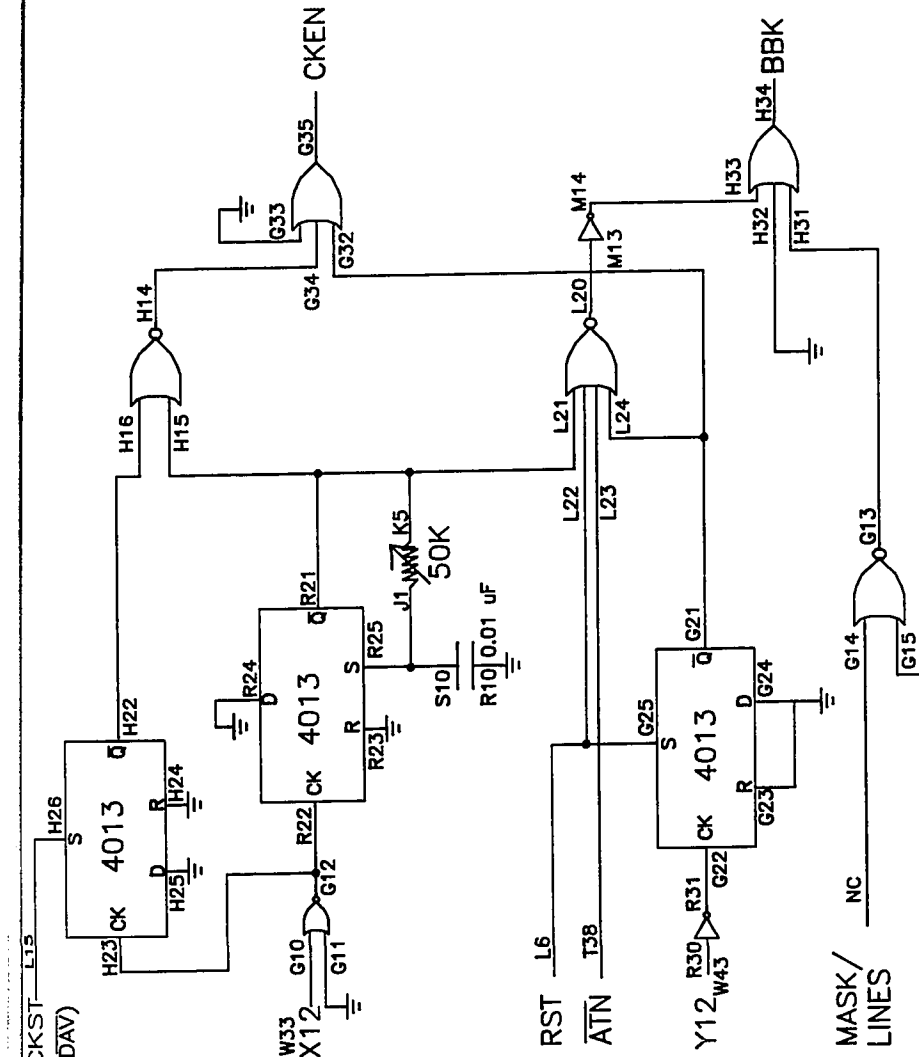

3. CLOCK ENABLE AND BEAM BLANK

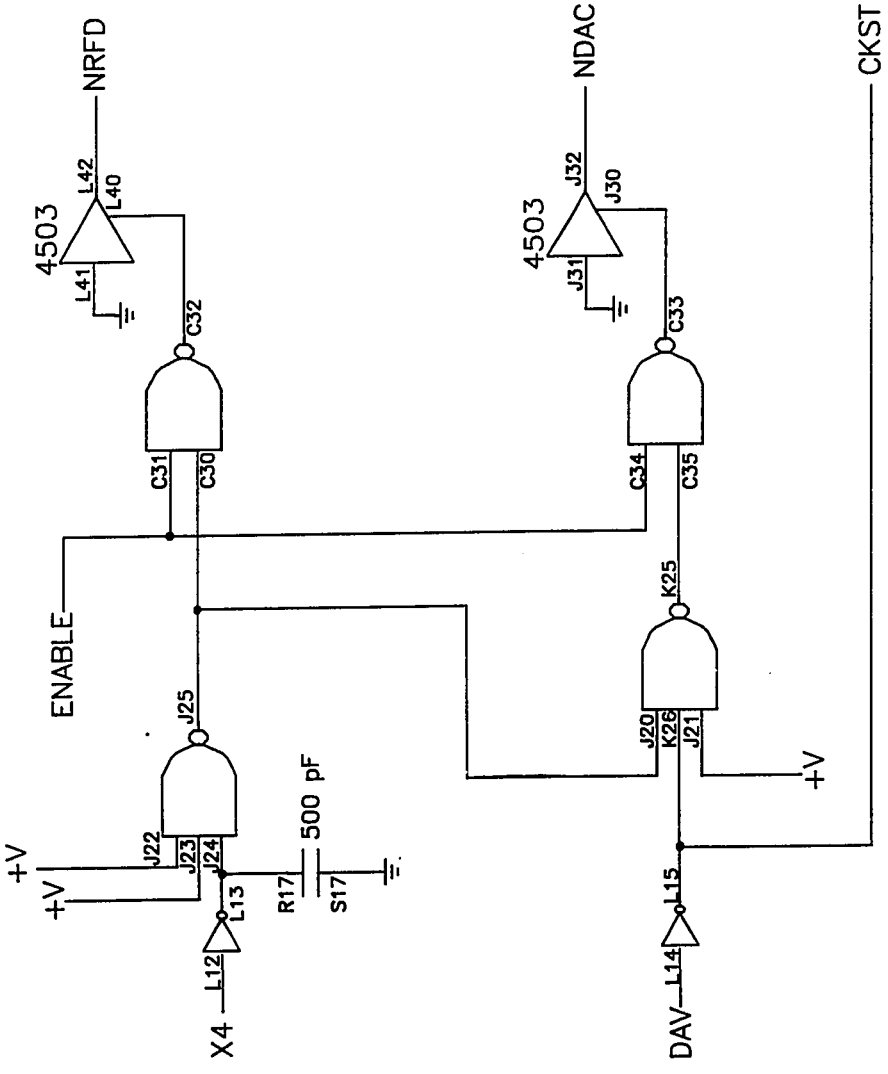
NRFD
4503
L42
L40
L41
C32
C31
C30
ENABLE
J25
+V
+V
J22
J23
J24
L13
R17
500 pF
S17
L12
X4
NDAC
4503
J32
J30
J31
C33
C34
C35
K25
J20
K26
J21
+V
L15
L14
DAV
CKST

4. HANDSHAKE

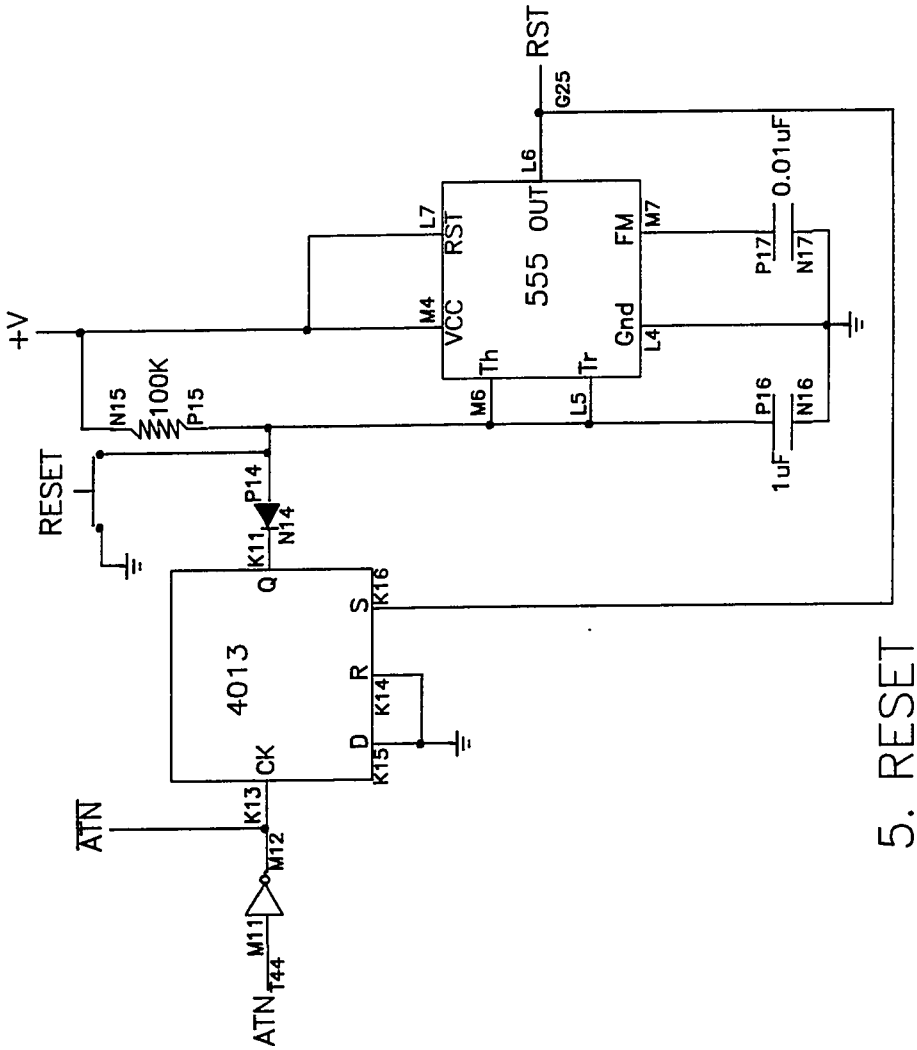
RST
G25
L6
555
OUT
L7
RST
M4
VCC
Th
M6
Tr
L5
Gnd
L4
FM
M7
P17
0.01uF
N17
+V
N15
100K
P15
P16
1uF
N16
RESET
P14
N14
K11
Q
S
K16
4013
R
K14
D
K15
CK
K13
ATN
M12
M11
T44
ATN

5. RESET

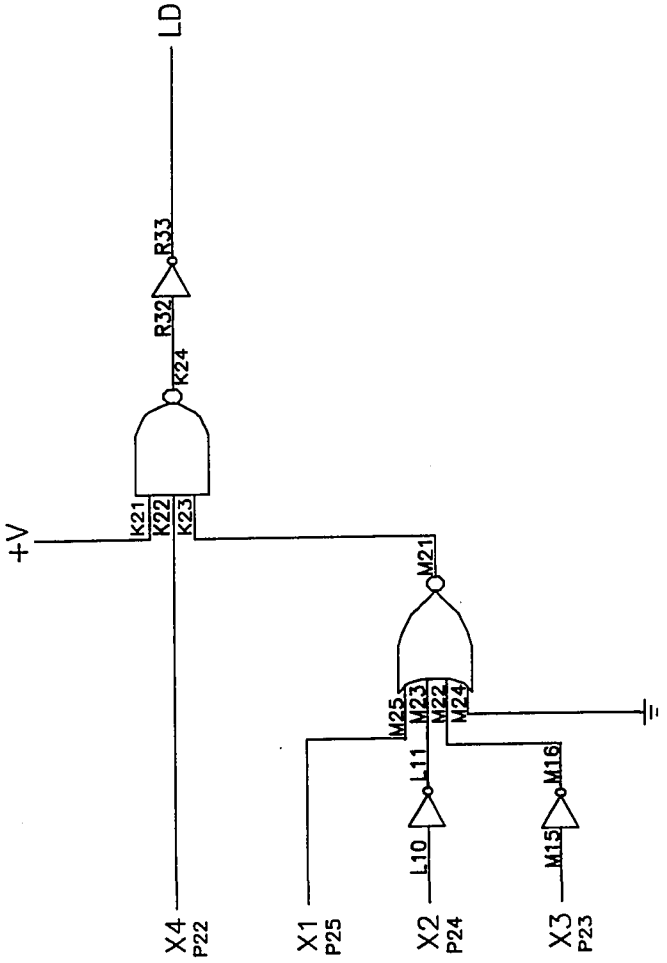

6. LOAD DECODING

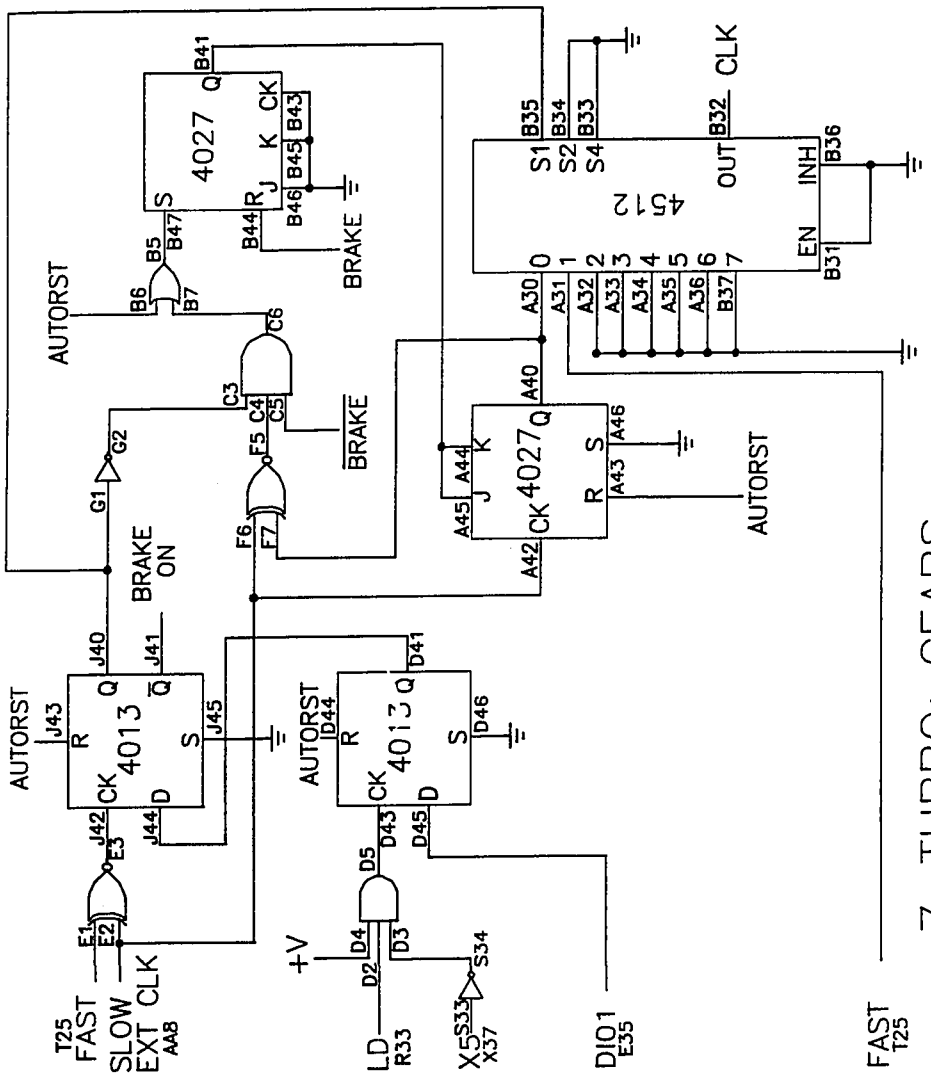
7. TURBO: GEARS
T25 FAST
SLOW
EXT CLK AA8
LD R33
X5 X37
DIO1 E35
FAST T25
+V
AUTORST
BRAKE ON
BRAKE
4013
4027
4512
CLK
OUT
INH
EN
S1
S2
S4

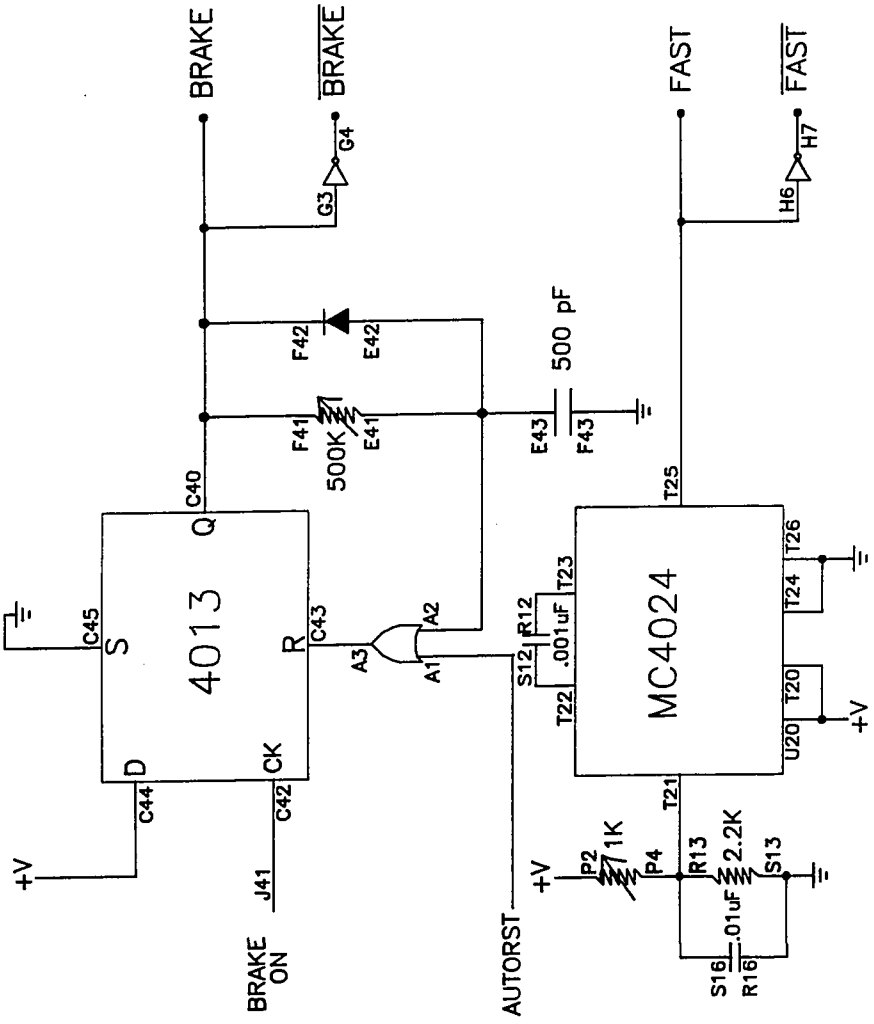

7B. TURBO FAST AND BRAKE

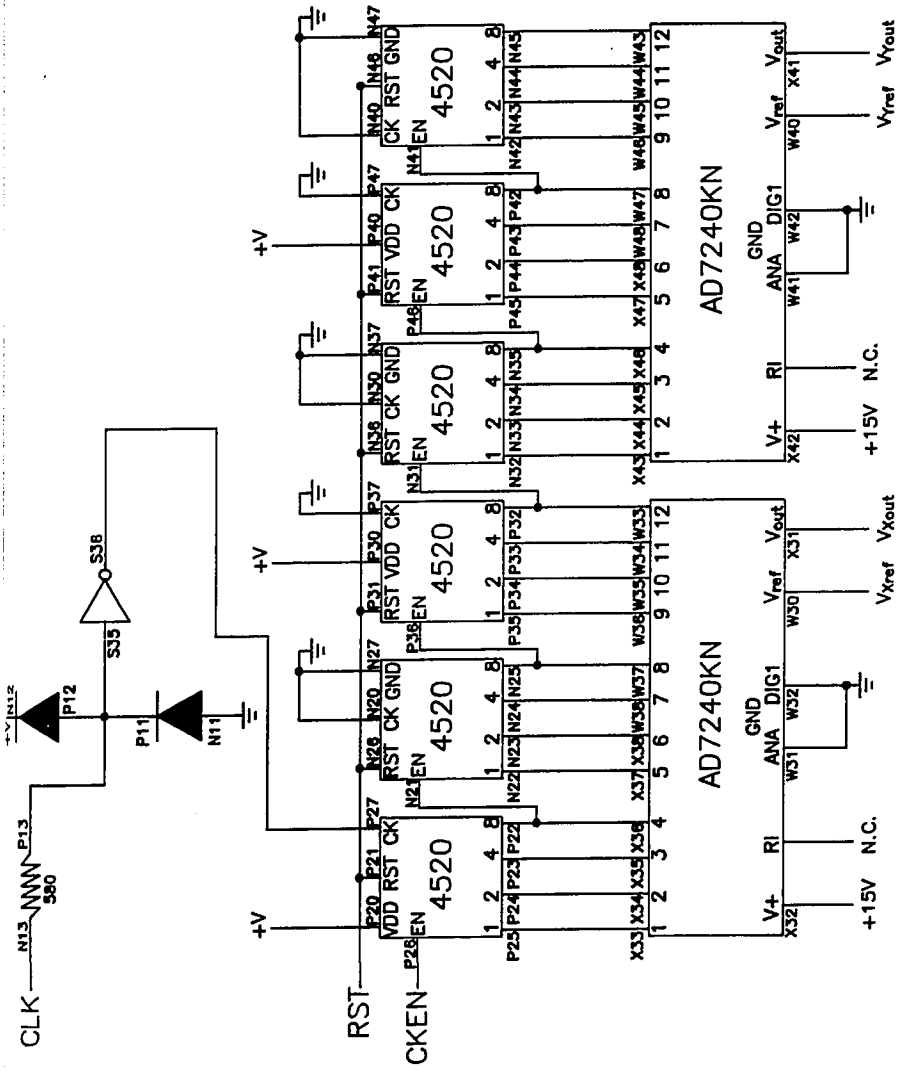

8. COUNTERS AND DACS

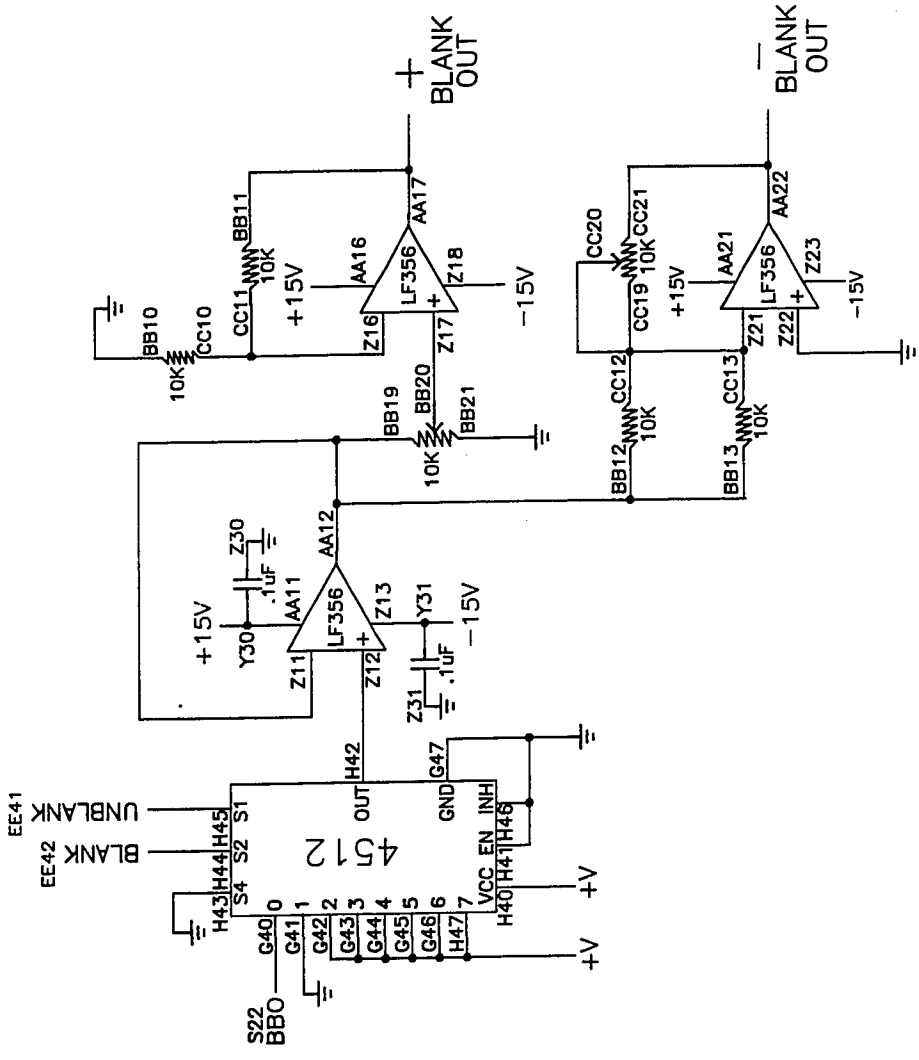

9. BEAM BLANK ANALOG OUTPUT

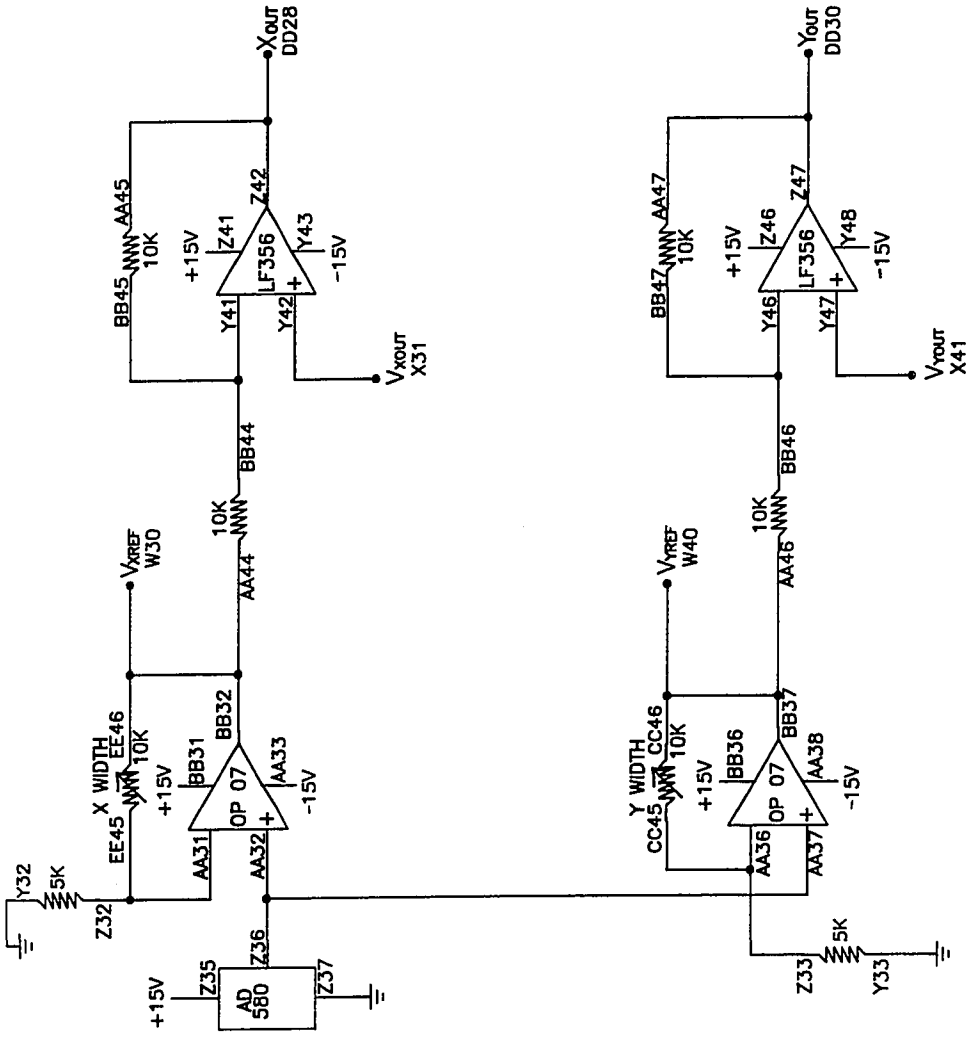

10. RASTER SWEEP ANALOG OUTPUT

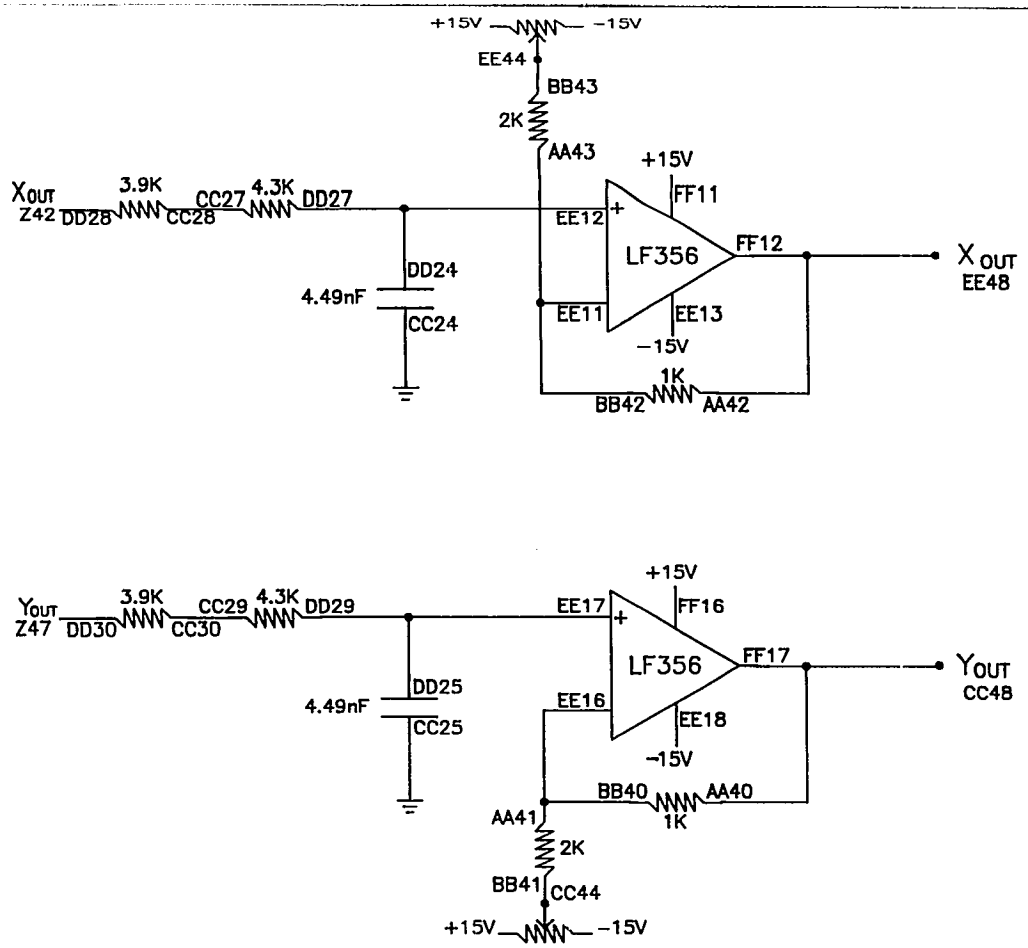

11. X AND Y FILTERS

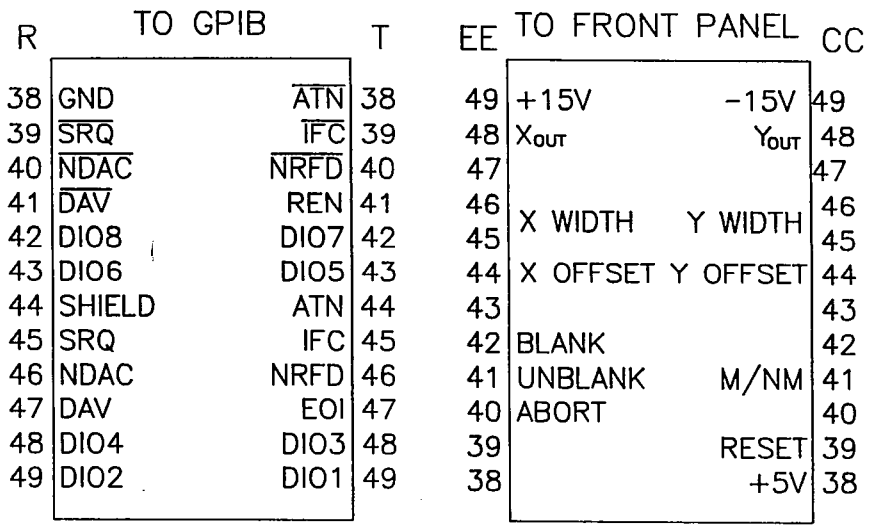

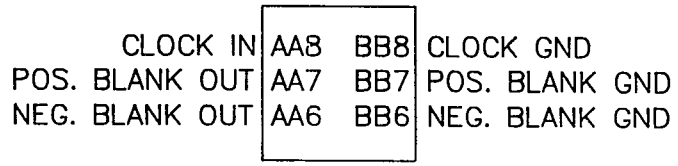

12. I/O TO GPIB AND FRONT PANEL

References

AAK: acronym for Altshuler, B. L., A. G. Aronov, and D. E. Khmelnitskii, J. Phys. C 15, 7367 (1982b).

Abrahams, E., P. W. Anderson, P. A. Lee, T. V. Ramakrishnan, Phys. Rev. B 24, 6783 (1981).

Aharonov, Y., and D. Bohm, Phys. Rev. 115, 485 (1959).

Aldrich Chemical Co., Milwaukee, WI, 450K MW PMMA, stock number (18,226-5).

Al-etch: phosphoric acid, nitric acid, acetic acid, water (16:1:1:2) from Allied Chemical Co.

Altshuler, B. L., A. G. Aronov, A. I. Larkin, and D. E. Khmelnitski, Zh. Eksp. Teor. Fiz. 81, 768 (1981) [Sov. Phys. JETP 54, 411 (1981)]; B. L. Alt'shuler, D. E. Khel'nitski, A. I. Larkin, and P. A. Lee, Phys. Rev. B 22, 5142 (1980).

Altshuler, B. L., A. G. Aronov, Solid State Commun. 38, 11 (1981 a).

Altshuler, B. L., A. G. Aronov, Pis'ma. Zh. Exsp. Teor. Fiz. 33, 515 (1981) [JETP Lett. 33, 499 (1981 b)].

Altshuler, B. L., A. G. Aronov, and B. Z. Spivak, JETP Lett. 33, 94 (1981).

Altshuler, B. L., A. G. Aronov, and B. Z. Spivak, D. Yu Sharvin, and Yu. V. Sharvin, Pis'ma Zh. Eksp. Teor. Fiz. 35, 476 (1982a) [JETP Lett. 35, 588 (1982a)].

Altshuler, B. L., A. G. Aronov, and D. E. Khmelnitskii, J. Phys. C 15, 7367 (1982b).

Altshuler, B. L., A. G. Aronov, D. E. Khmelnitskii, and A. I. Larkin, "Coherent Effects in Disordered Conductors", chapter in Quantum Theory of Solids, I. M. Lifshits, ed. (MIR Publishers, Moscow, 1982c).

Altshuler, B. L., and A. G. Aronov, "Electron-electron interaction effects in disordered conductors", chapter in Electron-Electron Interactions in Disordered Systems, A. L. Efros and M. Pollak, eds., Modern Problems in Condensed Matter Sciences 10, (North-Holland, Amsterdam, 1985).

Altshuler, B. L., and B. Z. Spivak, Pis'ma. Zh. Exsp. Teor. Fiz. 42, 363 (1985) [JETP Lett. 42, 447 (1985)].

Ambegaokar, V., and A. Baratoff, Phys. Rev. Lett. 10, 486 (1963).

Anderson, P. W., Phys. Rev. 109, 1492 (1958).

Ashcroft, N. W., and N. D. Mermin, Solid State Physics (Holt, Rinehart, and Winston, New York, 1976).

Balzers Optical Group, Marlborough, MA.

Baym, G., Lectures on Quantum Mechanics, (W. A. Benjamin, New York, 1969).

BDH Chemical Co., 185K MW PMMA, stock number 29774, distributed by Gallard-Schlesinger Mfg. Corp., Carle Place, NY.

Beaumont, S. P., P. G. Bower, T. Tamamura, C. D. W. Wilkinson, Appl. Phys. Lett. 38, 436 (1981).

Beaumont, S. P., S. Singh, and C. D. W. Wilkinson, Proc. 10th Conf. on Electron and Ion Beam Sci. and Technol., Montreal (1982).

Bergmann, G., Z. Phys. B 48, 5 (1982).

Bergmann, G., Phys. Rep. 107, 1 (1984).

Bethe, H. A., E. E. Salpeter, Quantum Mechanics of One- and Two- Electron Atoms, (Plenum, New York, 1977).

Bethe, H. A., Annalen der Physik, 3, 133-206 (1929); English translation: Splitting of Terms in Crystals, Consultants Bureau Inc., New York, 1929).

Bishop, D. J., J. C. Lincini, G. J. Dolan, Appl. Phys. Lett. 46, 1000 (1985).

Blackford, B. L., and R. H. March, Can. J. Phys. 46, 141 (1968).

Blonder, G., Bull. Am. Phys. Soc. 29, 535 (1984).

Broers, A. N., W. W. Molzen, J. J. Cuomo, and N. D. Wittels, Appl. Phys. Lett. 29, 596 (1976).

Broers, A. N., J. Electrochem. Soc. 128, 166 (1981).

Büttiker, M., Y. Imry, R. Landauer, S. Pinhas, Phys. Rev. B 31, 6207 (1985).

Büttiker, M., Phys. Rev. Lett. 57, 1761 (1986).

Chambers, R. G., Phys. Rev. Lett. 5, 3 (1960).

Chandrasekhar, V., M. J. Rooks, S. Wind, and D. E. Prober, Phys. Rev. Lett. 55,

1610 (1985).

Chandrasekhar, V., private communication, 1987.

Choi, K. K., D. C. Tsui, and K. Alavi, American Physical Society Meeting, KT6, March 1986 (unpublished).

Choi, K. K., D. C. Tsui, and K. Alavi, Appl. Phys. Lett. 50, 110 (1987). See also Choi, K. K., D. C. Tsui, and K. Alavi, Phys. Rev. B (to be published).

Craighead, H. G., R. E. Howard, L. D. Jackel, and P. M. Mankiewich, Appl. Phys. Lett. 42, 38 (1983).

Dalrymple, B. J., Ph.D. Thesis, Yale University, 1983 (University Microfilms, Ann Arbor, MI 48106).

Dalrymple, B. J., and D. E. Prober, Rev. Sci. Inst. 55, 958 (1984).

Datta, S., M. R. Melloch, S. Bandyopadhyay, R. Noren, M. Vaziri, M. Miller, R. Reifenberger, Phys. Rev. Lett. 55, 2344 (1985).

Dynes, R. C., Physica (Amsterdam) 109 & 110B, 1857 (1982).

Eiler, W., J. Low Temp. Phys. 56, 481 (1984).

Face, D. W., D. E. Prober, W. R. McGrath, P. L. Richards, Appl. Phys. Lett. 48, 16 (1986).

Face, D. W., Ph.D. Thesis, Yale University, 1987 (University Microfilms, Ann Arbor, MI 48106).

Face, D. W., and D. E. Prober, submitted to J. Appl. Phys., 1987.

Feng, S., P. A. Lee, A. D. Stone, Phys. Rev. Lett. 56, 1960 (1986).

Feuer, M. D., Ph.D. Thesis, Yale University, 1980 (University Microfilms, Ann Arbor, MI 48106).

Fisher, D. S., and P. A. Lee, Phys. Rev. B 23, 685 (1981).

Fukuyama, H., E. Abrahams, Phys. Rev. B 27, 5976 (1983).

Fukuyama, H., Chapter in Percolation, Localization, and Superconductivity, A. M. Goldman and S. Wolf, eds. (Plenum, New York, 1984).

Gates, George W. & Co., Franklin Square, NY, Model 420-U1, Hg bulb #UA-3.

Gefen, Y., Y. Imry, M. Y. Azbel, Phys. Rev. Lett. 52, 129 (1984).

Gershenzon, M. E., V. N. Gubankov, Yu. E. Zhuravlev, Pis'ma. Zh. Eksp. Teor. Foz. 35, 467 (1982) [JETP Lett. 35, 576 (1982)].

Ghandhi, S. K., VLSI Fabrication Principles, (John Whiley & Sons, New York,1983).

Gijs, M., C. Van Haesendonck, and Y Bruynseraede, Phys. Rev. Lett. 52, 2069 (1984).

Gordon, J. M., C. J. Lobb, and M. Tinkham, Phys. Rev. B 28, 4046 (1983).

Gordon, J. M., Phys. Rev. B 30, 6770 (1984).

Gordon, J. M., C. J. Lobb, and M. Tinkham, Phys. Rev. B 29, 5232 (1984).

Grabbe, P., Rev. Sci. Instrum., 51, 992 (1980).

Greeneich, J. S., "Electron-beam processes", in Electron-Beam Technology in Microelectronic Fabrication, George R. Brewer, ed., (Academic Press, New York, 1980).

Grobman, W. D., H. E. Luhn, T. P, Donohue, A. J. Speth, A. Wilson, M. Hatzakis, and T. H. P. Chang, IEEE Trans. Electron Dev. ED-26, 360 (1979).

Halbritter, J., Appl. Phys. 58, 1320 (1985).

Harris, R. E., Phys. Rev. B 10, 84 (1974).

Hatzakis, M., J. Vac. Sci. Technol. 16, 1984 (1979).

Hikami, S., A. I. Larkin, and Y. Nagaoka, Prog. Theor. Phys., 63, 707 (1980).

Howard, R. E., E. L. Hu, L. D. Jackel, IEEE Trans. Electron Dev. ED-28, 1378 (1981).

Howard, R. E., and D. E. Prober, "Nanometer-Scale Fabrication Techniques", from VLSI Electronics: Microstructure Science, vol. 5, (Academic Press, New York, 1982).

Howard, R. E., L. D. Jackel, P. M. Mankiewich, W. J. Skocpol, Science 231, 346 (1986).

HTG (Hybrid Technology Group) Co., San Jose, CA, Model 3HR with DUV system upgrade n211400; funding for this aligner was provided in part by ITT Co.

Imry, Y., "Physics of Mesoscopic Systems", chapter in Directions in Condensed Matter

Physics, G. Grinstein and G. Marzenko, eds. (World Publishers, Singapore, 1986).

Jackel, L. D., R. E. Howard, P. M. Mankiewich, H. G. Craighead, and R. W. Epworth, Appl. Phys. Lett. 45, 698 (1984).

Joy, D. C., Microelctron. Eng. 1, 103 (1983).

Kramer, B., G. Bergmann, and Y. Bruynseraede (Springer-Verlag, Berlin, 1985).

KTI Inc., Sunnyvale, CA.

Larkin, A. I., Pis'ma Zh. Eksp. Teor. Fiz. 31, 239 (1980) [JETP Lett. 31, 219 (1980).

Laibowitz, R. B., and C. P. Umbach, in Percolation, Localization, and Superconductivity, NATO ASI Series B: Physics vol. 109, (Plenum Press, New York, 1983), p.267.

Landauer, R., IBM J. Res. Dev. 1, 233 (1957).

Landauer, R., Philosoph Mag. 21, 863 (1970).

Langer, J. S., and T. Neal, Phys. Rev. Lett. 16, 984 (1966).

Langreth, D. C., E. Abrahams, Phys. Rev. B 24, 2978 (1981).

Lawrence, W. E., and A. B. Meador, Phys. Rev. B 18, 1154 (1978).

Lee, K. Y., J. Frost, W. Patrick, W. S. Mackie, S. P. Beaumont, and C. D. W. Wilkinson, "Fabrication of Ultra Small Devices on Thin Active GaAs Membrane", J. Vac. Sci. Technol. B, to appear Jan.-Feb. 1987.

Lee, P. A., and T. V. Ramakrishnan, Rev. Mod. Phys. 57, 287 (1985); see also [Bergmann, 1984].

Lee, P. A., and A. D. Stone, Phys. Rev. Lett. 55, 1622 (1985).

Lin, B. J., IBM J. Res. Develop. 20, 213 (1976), and J. Vac. Sci. Technol. 12, 1317 (1975).

Lin, B. J., "Multi-Layer Resist Systems", from Introduction to Microlithography, ASC Symposiun Series 219, (American Chemical Society, Washington, DC, 1983).

Lin, J. J., and N. Giordano, Phys. Rev. B 33, 1519 (1986).

Lopez dos Santos, J. M. B., and E. Abrahams, Phys. Rev. B 31, 172 (1985).

Mackie, S., private communication, 1985.

Mackie, S., and S. P. Beaumont, Solid State Technol., 28, No. 8, 117 (1985).

Mankiewich, P.M., R. E. Howard, L. D. Jackel, W. J. Skocpol, and D. M. Tennant, J. Vac. Sci. Technol. B4, 380 (1986).

Melngailis, J., H. I. Smith, and N. Efremow, IEEE Trans. Elec. Dev., 496, July 1975.

Molzen, W. W., A. N. Broers, J. J. Cuomo, J. M. E. Harper and R. B. Laibowitz, J. Vac. Sci. Technol. 16, 269 (1980).

Oriel Corp., Stratford, CT, lamp model #81281 with Ushio Hg-Xe lamp.

Pannetier, B., J. Chaussy, R. Rammal, and P. Gandit, Phys. Rev. Lett. 53, 718 (1984).

Patton, B. R., Phys. Rev. Lett. 27, 1273 (1971).

Prober, D. E., "Quantum Transport in Microstructures", Invited paper presented at International Conference on Microcircuit Engineering, Interlaken, Switzerland, 1986.

Petrashov, V., B. Nilsson, J. Bindslev Hansen, and T. Claeson, SQUID '85, H. D. Hahlbohm and H. Lübbig, eds. (Walter de Gruyter & Co., Berlin, 1985).

Pippard, A. B., Philos. Mag. 46, 1104 (1955).

Rooks, M. J., S. Wind, P. McEuen, and D. E. Prober, J. Vac. Sci. Technol. B 5, 318 (1987).

Ruggiero, S. T., E. K. Track, D. E. Prober, G. B. Arnold, and M. J. DeWeert, Phys. Rev. B 34, 217 (1986).

Santhanam, P., and D. E. Prober, Phys. Rev. B 29, 3733, 1984.

Santhanam, P., S. Wind, and D. E. Prober, Phys. Rev. Lett. 53, 1179 (1984).

Santhanam, P., Ph.D. Thesis, Yale University, 1985 (University Microfilms, Ann Arbor, MI 48106).

Santhanam, P., S. Wind, and D. E. Prober, Phys. Rev. B, to appear March 1 (1987).

Schmid, A., Z. Physik 271, 251 (1974).

Shankar, R., Principles of Quantum Mechanics, (Plenum, New York, 1980).

Sharvin, Y. V., Sh. Eksp. Teor. Fiz. 48, 984 (1965) [JETP 21, 655 (1965)].

Sharvin, D. Y., and Y. V. Sharvin, Pis'ma. Zh. Eksp. Teor. Fiz. 34, 285 (1981) [JETP Lett. 34, 272 (1981)].

Skocpol, W. J., L. D. Jackel, R. E. Howard, P. M. Mankiewich, R. E. Behringer, L. A. Fetter, and D. M. Tennant, in Proceedings of the International Conference on Localization, Interaction and Transport Phenomena in Impure Metals, Suppl. (PTB, Braunschweig, 1984), pp. 7-10.

Skocpol, W. J., P. M. Mankiwich, R. E. Howard, L. D. Jackel, D. M. Tennant, A. D. Stone, "Nonlocal Potential Measurements Inside Quantun Conductors", to be published.

Stone, A. D., Phys. Rev. Lett. 54, 2692 (1985).

Stone, A. D., Y. Imry, Phys. Rev. Lett. 56 189 (1986).

Stone, A. D., private communication, (1987).

Thompson, L. F., C. G. Wilson, and M. J. Bowden, eds., Introduction to Microlithography, ASC Symposiun Series 219, (American Chemical Society, Washington, DC, 1983).

Thouless, D. J., Phys. Rev. Lett. 39, 1167 (1977).

Tinkham, M., Introduction to Superconductivity, (McGraw-Hill, New York, 1975).

Umbach, C. P., S. Washburn, R. B. Laibowitz, and R. A. Webb, Phys. Rev. B 30, 4048 (1984).

Umbach, C. P., private communication, 1985.

Umbach, C. P., C. Van Haesendonck, R. B. Laibowitz, S. Washburn, and R. A. Webb, Phys. Rev. Lett. 56, 386 (1986).

UVP Inc., San Gabriel CA, Preliminary Data Release Z-800/08/78, Zn lamp model #Z-800.

Van Duzer, T., and C. W. Turner, Priciples of Superconductive Devices and Circuits, (Elsevier, New York, 1981).

Washburn, S., C. P. Umbach, R. B. Laibowitz, and R. A. Webb, Phys. Rev. 32, 4789 (1985).

Webb, R. A., S. Washburn, C. P. Umbach, and R. B. Laibowitz, Phys. Rev. Lett. 54,

2696 (1985).

Webb, R. A., et al., 1987, to be published.

Wind, S., M. J. Rooks, V. Chandrasekhar, and D. E. Prober, Phys. Rev. Lett. 57, 633 (1986).

Wind, S., Ph.D. Thesis, Yale University, 1987 (University Microfilms, Ann Arbor, MI 48106).

Wolcott, N. M., and J. Hilsenrath, A Contribution to Computer Typesetting Techniques: Tables of Coordinates for Hershey's Repertory of Occidental Type Fonts and Graphic Sumbols, National Bureau of Standards Special Publication 424, (U.S. Gov't Printing Office, Washington DC, 1976 -- out of print).

Wolf, E. L., Principles of Electron Tunneling Spectroscopy, (Oxford Un. Press, London, 1985).

Ziman, J., M., Electrons and Phonons (Clarendon Press, Oxford, 1960).